Doctoral Thesis

Microscopic Studies of π-d Molecular Conductor λ-$(BETS)_2FeCl_4$ by ESR

Taehoon Lee

Condensed Matter Physics, Graduate School of Science, Hokkaido University

March 2019

Contents

Chapter 1

Introduction

1.1 Molecular based conductors

For a long time, the organic materials are thought as the electrical insulators. However, TTF(TCNQ) was found to have a high electrical conductivity at room temperature in 1973 [1, 2], where TTF and TCNQ are tetrathiafulvalene and 7,7,8,8,-tetracyanoquinodimethane, respectively.

TCNQ was first synthesized by Acker *et al*. [3]. It is a symmetrical-planar molecule as shown in Fig. 1.1(a). Meanwhile, TTF was synthesized by several groups [3–8], which is also a symmetrical-planar molecule and consists of S, C and H atoms as shown in Fig. 1.1(a). TTF molecule is a donor molecule, and has a tendency to give electrons. Meanwhile, TCNQ molecule is an acceptor molecule, and has a tendency to accept electrons [1, 2, 9, 10].

In TTF(TCNQ), the electron from the highest occupied molecular orbital (HOMO) of the TTF molecule is transferred into the lowest unoccupied molecular orbital (LUMO) of the TCNQ molecule, leading to a stable charge-transfer salt as shown in the Fig. 1.1(b). TTF and TCNQ molecules stack face-to-face with the interstack spacings of 3.47 and 3.17 Å, respectively [11]. For both molecule, the π-orbitals overlap along the stacking direction. Hence, the TTF(TCNQ) salt is a quasi 1-dimensional conductor, where the electrical conductivity can reach the value of a conventional metal. However, a metal-to-insulator (MI) transition is observed at 50 K, which is identified as the Peierls transition due to its low-dimensionality [12]. For avoiding the Peierls instability, scientists were motivated to apply pressure and to develop

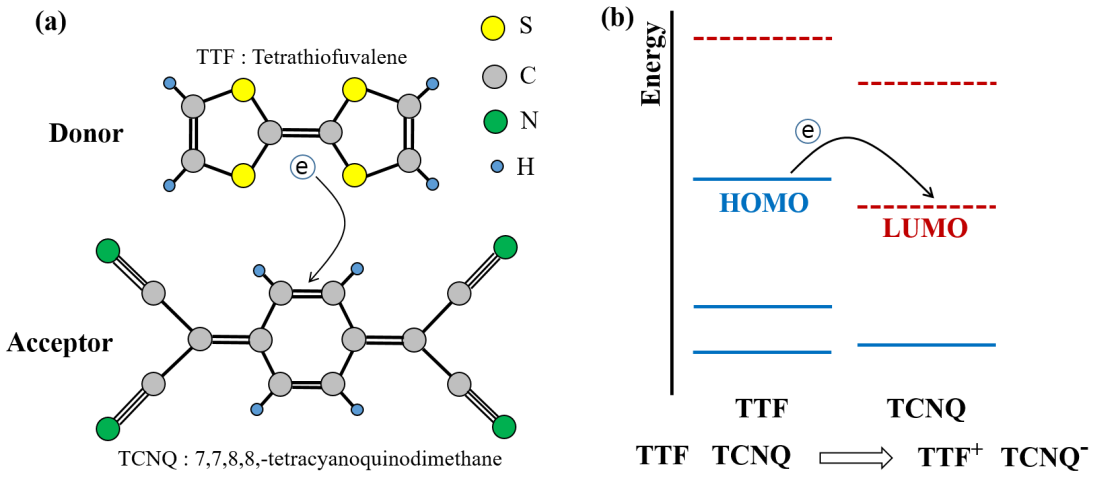

Figure 1.1: Schematic picture of (a) the molecular structure of TTF and TCNQ, (b) simplified energy levels of TTF(TCNQ) [9, 10].

new donors or acceptors with stronger intermolecular couplings.

In 1980's, TMTSF (tetramethyltetraselenafulvalene) was synthesized by Bechgaard *et al.*, where the molecule is shown in Fig. 1.2(a) [13]. $(TMTSF)_2X$ complexes are called as Bechgaard salts, where X is the counter anion. Here, the anion X has a closed-shell configuration by accepting an electron, hence, it does not contribute to the conducting property. The anion takes one electron from the HOMO of TMTSF molecule, and the charge is +0.5 per TMTSF molecule for the case of 2:1 salt. As a result, the band structure is 3/4-filled (or 1/4-filled for holes). TMTSF molecules are stacked face-to-face with the overlapped π-orbitals as shown in Fig. 1.2(b). Hence, $(TMTSF)_2PF_6$ is also a quasi 1-dimensional conductor. Unfortunately, $(TMTSF)_2PF_6$ has a MI transition around 12 K at ambient pressure, which is similar to the TTF(TCNQ) salt. However, $(TMTSF)_2PF_6$ becomes a superconductor at 0.9 K when the pressure of about 12 kbar is applied, as shown in Fig. 1.2(c) [14]. After these findings, the research on organic conductors exploded. Because it attracted peoples interests that the organic materials are able to become a metal and even a superconductor.

The intermolecular interactions are determined not only by the distance between adjacent molecules but also by their spatial arrangements. The strong tendency for having a MI transition (i.e. Peierls transition) in TMTSF compounds is inherent in the quasi 1-dimensionality of the electron systems. In order to achieve ambient-pressure superconductivity in these organic complexes with potentially high transition temperature, it is necessary to increase

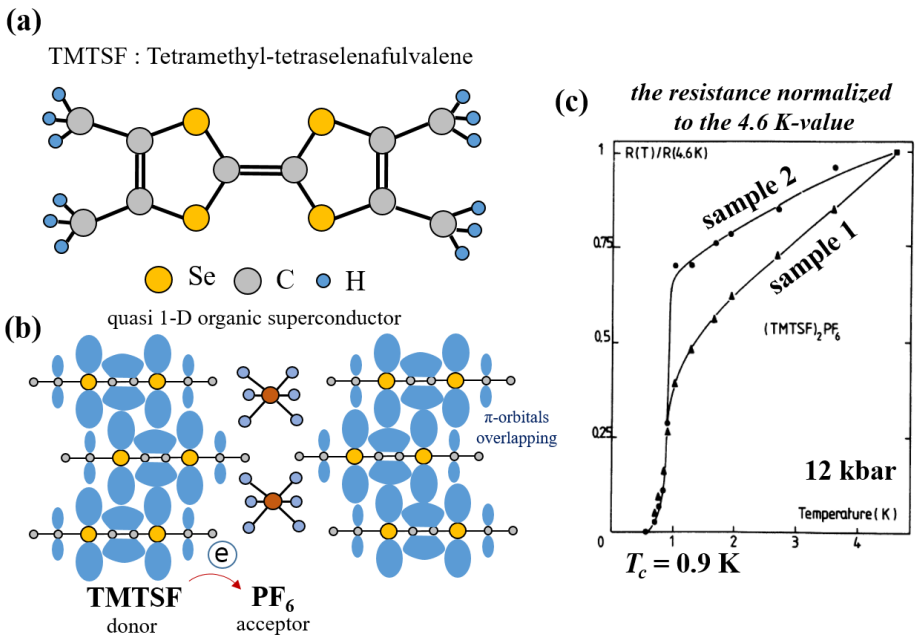

Figure 1.2: (a) The cartoon of the TMTSF molecule, (b) side view of the TMTSF stacks and (c) temperature dependence of the resistance [14].

their dimensionality of the electron system. And, the enhancement of a quasi 2-dimensional interstack interaction was achieved by the bisethylenedithio-tetrathiafulvalene (BEDT-TTF, or simply ET) molecule. The molecular structure of ET is depicted in Fig. 1.3(a), where ET is a planar molecule based on S, C and H atoms. Several types of ET molecule arrangements are shown in Fig. 1.3(b) [15]. Due to the arrangements of ET molecules and the π-orbital overlaps, the resulting salts are mostly quasi 2-dimensional organic conductors with high conductivity within the ET layers, and are insulating perpendicular to the layers since the counter anion is a closed-shell and does not participate in conducting properties. Indeed, the BEDT-TTF charge-transfer salts have been formed with a variety of anions such as I_3 and $Cu(NCS)_2$. Among them, κ-type arrangements have provided many superconductors. κ-$(ET)_2I_3$ was reported by Kato *et al.* as the 2-dimensional superconductor, where the transition temperature was found at 3.6 K [16,17]. Soon after that, higher transition temperature ($T_c = 10.4$ K) was observed in κ-$(ET)_2Cu(NCS)_2$ salt by Saito *et al* in 1987. Successively, the critical temperature of ambient pressure organic superconductor with κ-$(ET)_2Cu[N(CN)_2]Br$ was further raized to 11.8 K [18]. In contrast, κ-$(ET)_2Cu[N(CN)_2]Cl$ displays non-metallic behavior at ambient pressure, but superconductivity was found at 12.8 K by applying the

pressure of about 30 MPa [19, 20].

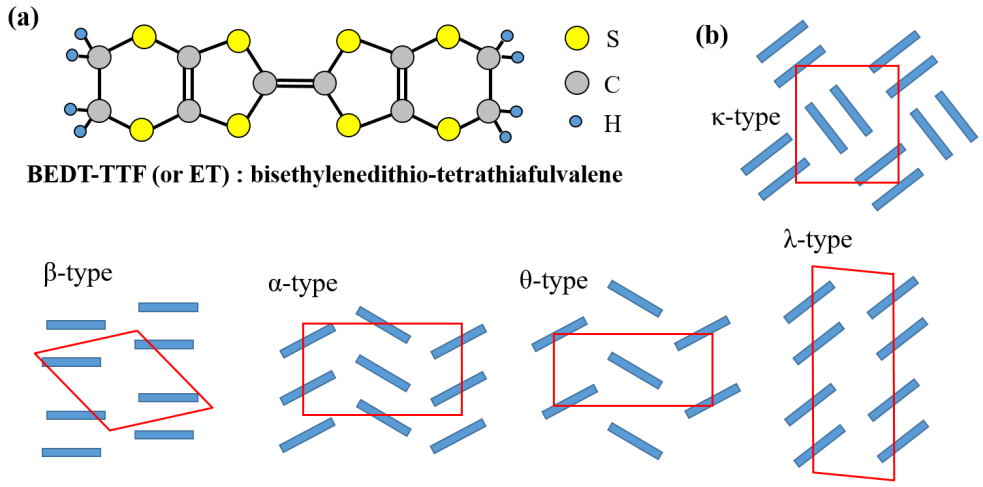

Figure 1.3: Schematic picture of (a) the molecular structure of BEDT-TTF (or simply ET) and (b) various stacking patterns of ET molecules. The blue thick line and red rectangle represent the ET molecule and the unit cell, respectively. [21]

The interplay between magnetism and superconductivity has been an intriguing subject not only for the TMTSF salts but for κ-type ET salts where the antiferromagntism exists adjacent to the superconductivity as for the high-T_c cuprates. In order to expand or improve the ET molecule yielding superconductors, partial substitutions of S atoms with other atoms has been carried out. To promote intermolecular interaction, Se atoms, which have larger orbits, were introduced. Among such molecules BETS (bis(ethylenedithio) tetraselenafulvalene) was synthesized by Kobasyshi *et al*. [22] (See Fig. 1.4), where Se atom is expected to increase the stability of the metallic state. The details of the BETS based compounds are introduced in the next section.

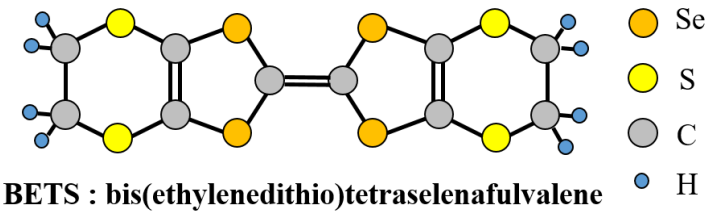

Figure 1.4: Molecular structure of of BETS molecule [22]

Subsequently, DMET (dimethylenthylenedithio-diselenadithiafulvalene) was synthesized by Kikuchi *et al*. [23], which is an asymmetrical donor molecule regarded as a hybrid between ET and TMTSF as shown in Fig. 1.5. DMET salts have also superconductivity below 4 K [24].

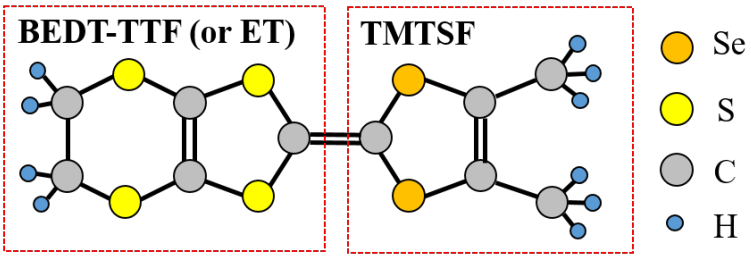

DMET : dimethylenthylenedithio-diselenadithiafulvalene

Figure 1.5: Asymmetrical donor molecule DMET [23, 25]

1.2 π-d molecular conductors

For molecular application, the giant magnetoresistance in molecular materials is one of a key phenomenon. To achieve such physical property, it is important to promote interaction between conductivity and magnetism. Hence, several studies have been focused on molecular conductors having an interaction between the conducting π-electrons and the magnetic d-electrons known as the π-d interaction (See Fig. 1.6). The localized d-electrons of the magnetic anions play a role of magnetism, and are interacting with the π-electrons of molecular (or organic) conductors.

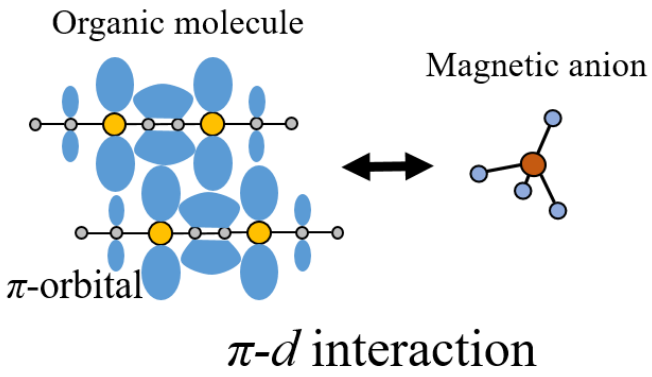

Figure 1.6: Schematic picture of the π-d interaction in molecular conductors

1.2.1 Transport properties of π-d molecular conductors

One of the well-known π-d molecular conductors is the $(DMET)_2FeBr_4$ [23, 25, 26]. DMET is already shown in Fig. 1.5, and $FeBr_4^-$ is an anion with Fe^{3+} (S=5/2). Fig. 1.7 shows the crystal structure of $(DMET)_2FeBr_4$, where the electrons are transfered from DMET dimers to the $FeBr_4^-$ anions. Short intermolecular Br $\cdots$ S contacts, which are the origin of the π-d interactions, are shown in Fig. 1.7 (The solid lines are π-d, d-d interactions). The electrical conductivity shows a metallic state down to $T_{MI} = 40$ K, and a Mott insulating state is stabilized below T_{MI}. The magnetic d-electrons of the $FeBr_4$ anion have an antiferromagnetic (AF) long-range order at $T_N = 3.7$ K [26]. The magnetization and the resistance of $(DMET)_2FeBr_4$ were reported by Enomoto *et al.* as shown in Fig. 1.8 [26]. These observations show the relation between the magnetic and the electronic properties. Some resistive changes are seen at the spin-flop field $B_{\mathrm{sf.d}}$ and the saturation field B_2. Thanks to the π-d interaction, the magnetotransport properties are affected by the magnetic properties.

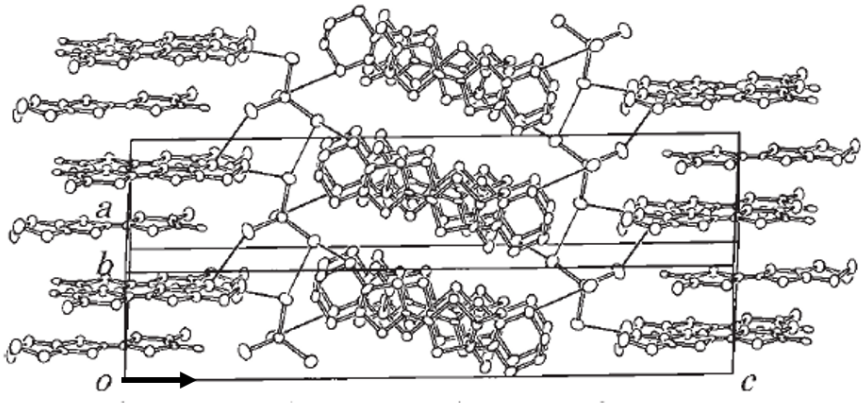

Figure 1.7: The crystal structure of $(DMET)_2FeBr_4$ where the solid lines are the contacts S $\cdots$ Br and Br $\cdots$ Br [26].

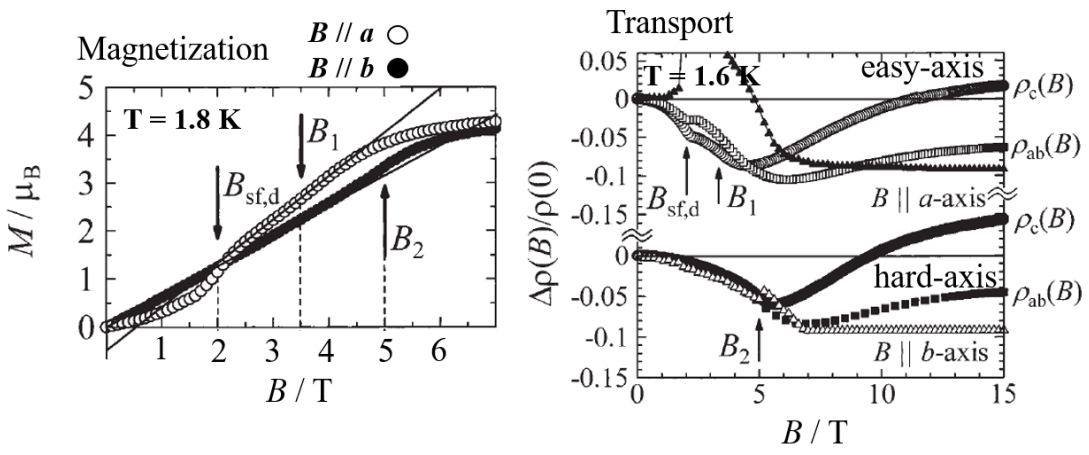

Figure 1.8: The magnetization curve of $(DMET)_2FeBr_4$ measured at 1.8 K and the field dependence of resistance measured at 1.6 K [26].

$Fe(Pc)(CN)_2$ is another type of the π-d molecular conductor, where Pc is phthalocyanine [27]. There are two type of anion : $[Fe^{2+}(Pc)(CN)_2]^{2-}$ anion and $[Fe^{3+}(Pc)(CN)_2]^{-}$ anion. In this thesis, only the Fe^{3+} case will be introduced. $Fe(Pc)(CN)_2$ with Fe^{3+} (low-spin state $S = 1/2$) is shown in Fig. 1.9(a) [28]. In $Fe(Pc)(CN)_2$, there is localized magnetic d-electron in the center of the molecule, and the d-electron is surrounded by the molecular π-electron [27, 29]. Hanasaki *et al.* have reported the giant negative magnetoresistance of $TPP[Fe(Pc)(CN)_2]_2$ at low temperature, where TPP is tetraphenylphosphonium [28]. The $TPP[Fe(Pc)(CN)_2]$ is a charge-transfer salt, where TPP is a donor and $Fe(Pc)(CN)_2{}^{-}$ is an anion. Due to the existence of the axial CN ligands, the $Fe(Pc)(CN)_2$ molecules are stacked face-to-face with π-orbital partially overlapped between Pc rings. The stacking forms a quasi 1-dimensional structure along the c-axis as shown in Fig. 1.9(b). The Fig. 1.9(c) shows the giant negative magnetoresistance of $TPP[Fe(Pc)(CN)_2]_2$ where the negative magnetoresistance is enhanced when the temperature is lowered. These results suggest that the giant negative magnetoresistance are caused by the π-d interaction inside the $Fe(Pc)(CN)_2$ molecule [30].

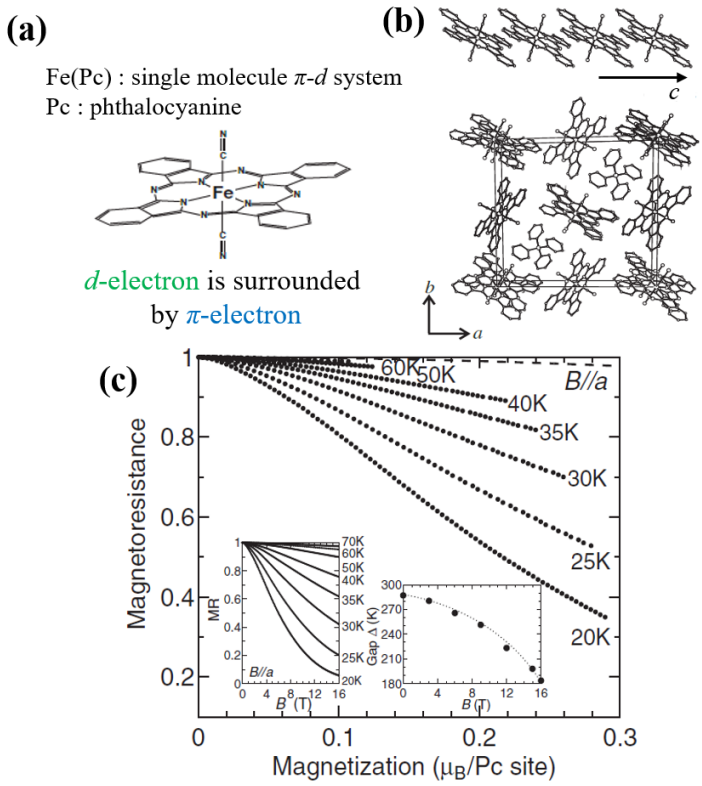

Figure 1.9: Schematic picture of (a) the crystal structure of $Fe(Pc)(CN)_2$ where the planar ring part of the molecules is Pc. (b) (top) Stacking of molecules along the c-axis and (bottom) the crystal structure of $TPP[Fe(Pc)(CN)_2]_2$. (c)The magnetoresistance of $TPP[Fe(Pc)(CN)_2]_2$ (2006) The physical Society of Japan [28]

1.2.2 Transport properties of λ-$(BETS)_2FeCl_4$

The π-d molecular conductors based on BETS molecule have two kinds of arrangement : λ-type and κ-type (See Fig. 1.3(b)). The BETS molecule is already shown in Fig. 1.4. Several BETS salts were synthesized with magnetic counter anions such as $FeCl_4$, $FeBr_4$, $CoCl_4$, $MnCl_4$, $MnBr_4$, $NiCl_4$, $NiBr_4$, $CuCl_4$, $CuBr_4$, and else [31]. The π-electrons in BETS molecules interact with the magnetic d-electrons on the anion sites, thanks to the short π-d contacts. In this subsection, needle-shaped crystal λ-$(BETS)_2FeCl_4$ will be introduced [31].

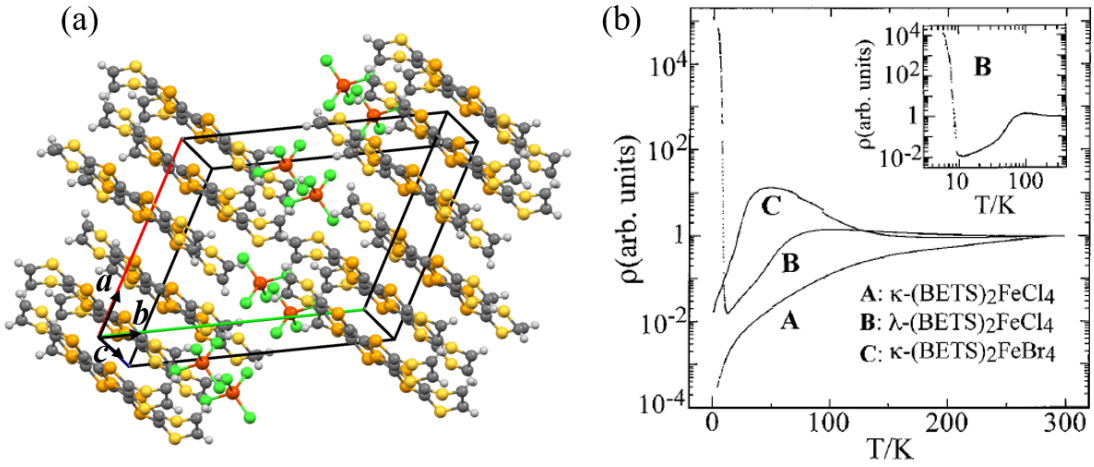

Figure 1.10: (a) Crystal structure of λ-$(BETS)_2FeCl_4$ (b) Temperature dependence of the resistance for κ-$(BETS)_2FeCl_4$, λ-$(BETS)_2FeCl_4$ and κ-$(BETS)_2FeBr_4$ [31].

The λ-$(BETS)_2FeCl_4$ have a triclinic crystal structure with the space group of $P\bar{1}$, having only one inversion center except for the translational symmetry operation. The crystal structure of λ-$(BETS)_2FeCl_4$ is shown in Fig. 1.10(a). The first transport properties of λ-$(BETS)_2FeCl_4$ was reported by Kobayashi *et al.* as shown in Fig. 1.10(b) [31]. λ-$(BETS)_2FeCl_4$ is metallic in the high temperature region, and shows a MI transition at T_{MI} = 8.3 K. As explained later, this MI transition is related with the antiferromagnetic transition. Fig. 1.11 shows the field dependence of the resistance in λ-$(BETS)_2FeCl_4$ [32]. In relation with the full magnetization, the metallic state is recovered above 10.5 T as shown in Fig. 1.11 [32].

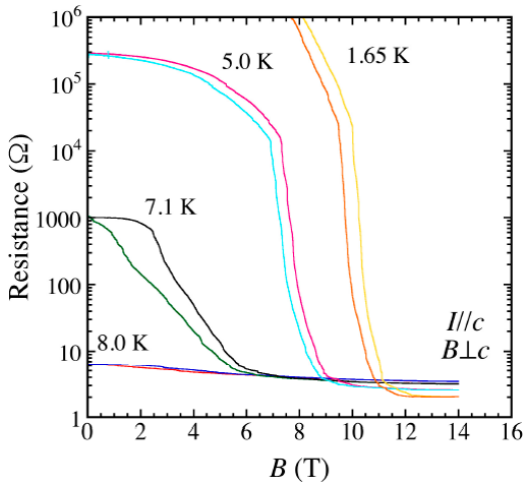

Figure 1.11: The magnetoresistance of λ-$(BETS)_2FeCl_4$ at several temperature [32].

By applying more higher magnetic field, a field-induced superconductivity is observed above 17 T when the magnetic field is parallel to conducting-plane (See Fig. 1.12(a)) [33]. The mechanism of the FISC phase can be explained by the Jaccarino-Peter compensation mechanism [33–37] (See Fig. 1.13). The strong external field polarizes the d-electrons, and the polarized d-electron induces internal field to the π-electron due to the π-d interaction. And then, the internal field is compensated by the external field. Hence, the effective magnetic field becomes zero, and Zeeman effect, which kills the superconductivity, disappears. This is known as the Jaccarino-Peter compensation mechanism. Furthermore, as long as the external field is parallel to the conducting layers, the orbital effect is virtually suppressed due to the highly 2-dimensional electronic state. Hence, a field-induced superconductivity can be achieved by applying high magnetic field parallel to the conducting-plane. The phase diagram of the mixed compounds λ-$(BETS)_2Fe_xGa_{1-x}Cl_4$ is shown in Fig 1.12(b). Here, $GaCl_4$ is a non-magnetic anion, and π-d interaction can be controlled by substituting the $FeCl_4$ anion to the $GaCl_4$ anion. The AFI phase shrinks with decreasing the $FeCl_4$ contents, and the FISC phase moves to lower magnetic field since the internal field decreases with the increase of non-magnetic contents. These results support that strong π-d interaction exists in λ-$(BETS)_2FeCl_4$. The internal field $H_{\rm int}$ can be obtained from the superconducting phase diagram, where the $H_{\rm int}$ is determined at highest critical temperature of the FISC phase. The value of $H_{\rm int}$ is 33 T. And, the exchange interaction $J_{\pi d} \sim 17.7$ K is obtained by $J_{\pi d} \sim \frac{g\mu_B H_{\rm int}}{S_d}$, where the g-value is $g = 2$, the μ_B is Bohr magneton, and $S_d = 5/2$ is the spin of the d-electron [33, 38].

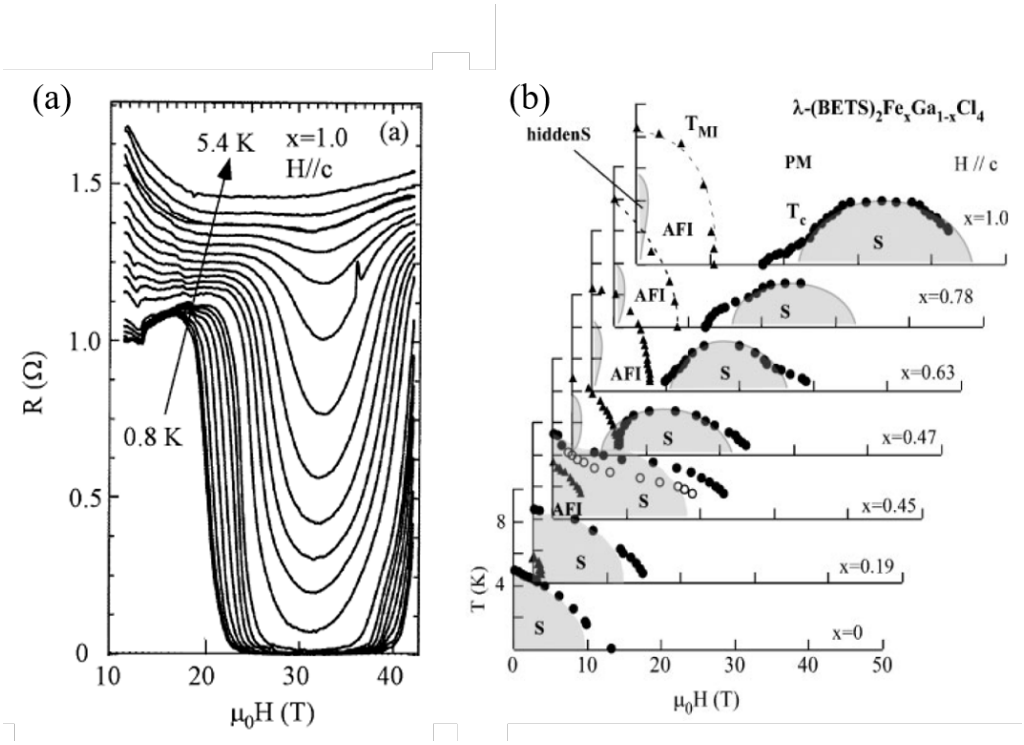

Figure 1.12: (a) In λ-$(BETS)_2FeCl_4$ field-dependence of resistance between 0.8 and 5.4 K. (b) The phase diagram for λ-$(BETS)_2Fe_xGa_{1-x}Cl_4$ (2006) The physical Society of Japan [33]

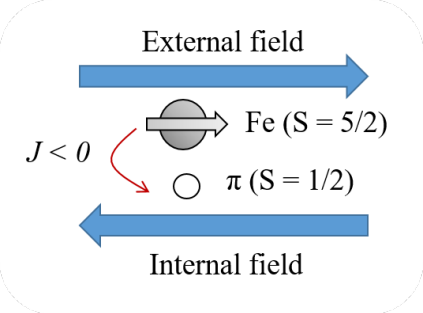

Figure 1.13: Schematic picture of the Jaccarino-Peter compensation mechanism.

1.2.3 Other physical properties of λ-$(BETS)_2FeCl_4$

The crystal structure of λ-$(BETS)_2FeCl_4$ was first reported by Kobayashi *et al.* (See Fig. 1.14) [31]. The crystal structure of λ-$(BETS)_2FeCl_4$ was determined at room temperature and 10 K. The lattice parameters are given in Table 1.1. The BETS molecules with conducting π-electrons ($S_\pi = 1/2$) are stacked along the a-axis. Two BETS dimers and one $FeCl_4^-$ anion are crystallographically independent [31, 39]. The localized magnetic d-electrons ($S_d = 5/2$) exist in the $FeCl_4^-$ anion. The d_n ($n = 1, 2, \cdots 5$) in Fig. 1.14 is the short contacts between Cl $\cdots$ S(Se), which is the origin of strong π-d interaction.

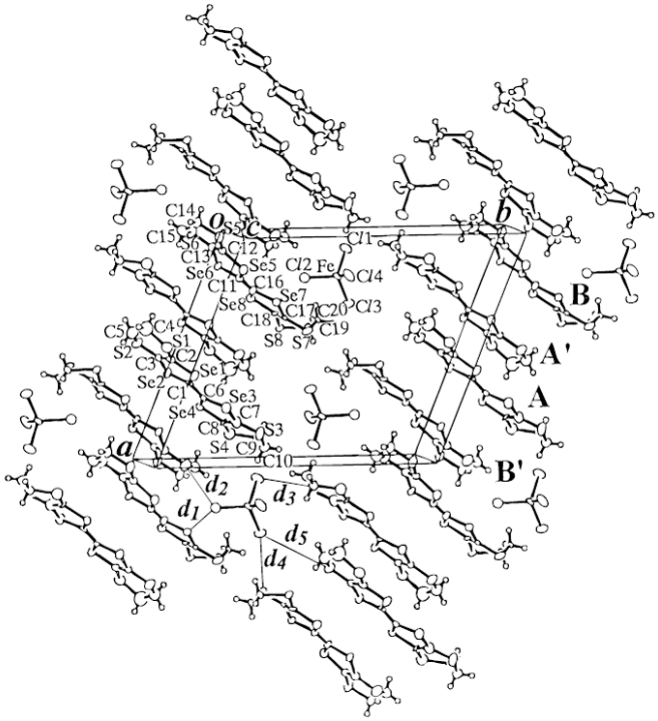

Figure 1.14: The crystal structure of λ-$(BETS)_2FeCl_4$ [31].

λ-$(BETS)_2FeCl_4$		
Chemical formula	$C_{20}S_8Se_8H_{16}GaCl_4$	
Space group	$P\bar{1}$	
Temperature	room temperature	10 K
a (Å)	16.164(3)	15.890(7)
b (Å)	18.538(3)	18.378(8)
c (Å)	6.5928(8)	6.531(4)
α (°)	98.40(1)	98.61(4)
β (°)	96.67(1)	96.67(1)
γ (°)	112.52(1)	112.05(3)
V (Å^3)	1773(5)	1716(1)

Table 1.1: Lattice parameters of λ-$(BETS)_2FeCl_4$ [31].

Tokumoto *et al.* reported the magnetic susceptibility of λ-$(BETS)_2FeCl_4$ as shown in Fig. 1.15 [40, 41]. The magnetic susceptibility shows the AF behavior below $T_N = 8.3$ K. The magnetic susceptibility shows a step around 8.3 K when the magnetic field parallel to the c-axis. The step is reduced by applying a high magnetic field. This magnetic susceptibility step is expected to be due to the localized π-electrons since the MI transition is observed at $T_{MI} = 8.3$ K (See Fig. 1.10(a)). The correlation with the magnetic susceptibility and the resistivity suggests the existence of strong interaction between the conducting π-electron and magnetic d-electron. In the high temperature phase, the magnetic and the electric properties of λ-$(BETS)_2FeCl_4$ are paramagnetic and metallic, respectively. This high temperature phase is called the paramagnetic metal (PM) phase. λ-$(BETS)_2FeCl_4$ becomes antiferromagnetic and insulating below 8.3 K, and the phase is called as the antiferromagnetic-insulating (AFI) phase [31, 41, 42].

The magnetic torque measurements were reported by Sasaki *et al.* [43] (See Fig. 1.16). As shown in Fig 1.16(a), the AF easy-axis is found to be at $\theta_{AF} = 122 \sim 125°$, which is tilted 30° from the c-axis. A sharp structure is observed at 1.2 T in Fig. 1.16(b), which is the spin-flop (SF) transition. The SF transition is the first order transition of Fe spins.

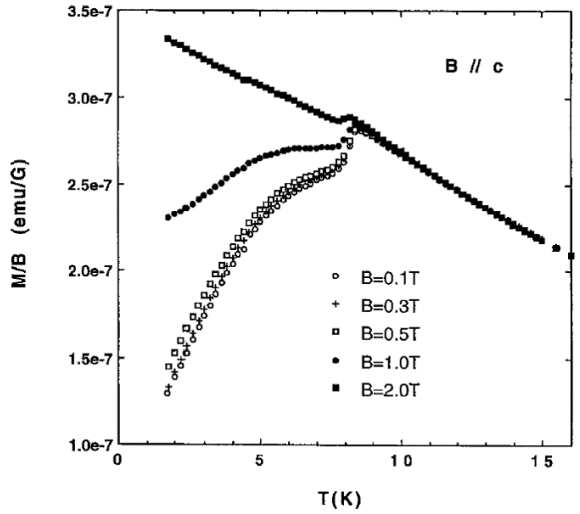

Figure 1.15: Temperature dependence of the magnetic susceptibility with B // c-axis [40, 41].

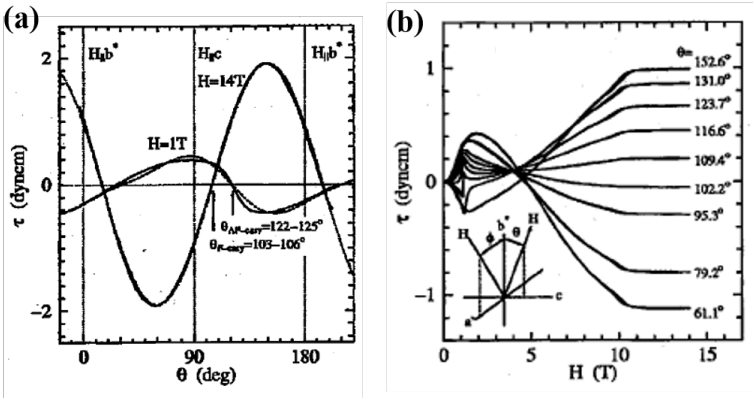

Figure 1.16: (a) Angular dependence of magnetic torque of λ-$(BETS)_2FeCl_4$ at 1 T (AF phase) and 14 T(ferromagnetic phase), and (b) field-dependence of magnetic torque of λ-$(BETS)_2FeCl_4$ at 4.5 K. [43].

Negishi *et al.* reported the first specific heat measurement of λ-$(BETS)_2FeCl_4$ [44]. They have observed a transition peak at 8.3 K, which is due to the AF transition. They also observed a huge excess specific heat below 8.3 K, where they attributed to the short-range order of Fe spins. Akiba *et al.* also performed heat capacity measurements [45], and the result is shown in Fig. 1.17(c). From their result, the origin of the large excess heat capacity was explained from the Schottky contribution of paramagnetic Fe-spins. From their explanation, the transition peak at 8.3 K is not due to the AF order of Fe spins, but is due to the Mott transition of the π-electrons, and the π-electrons become antiferromagnetic long-range ordered as shown in Fig. 1.17(b). Then, the π-electrons induce an internal field to the d-electrons,

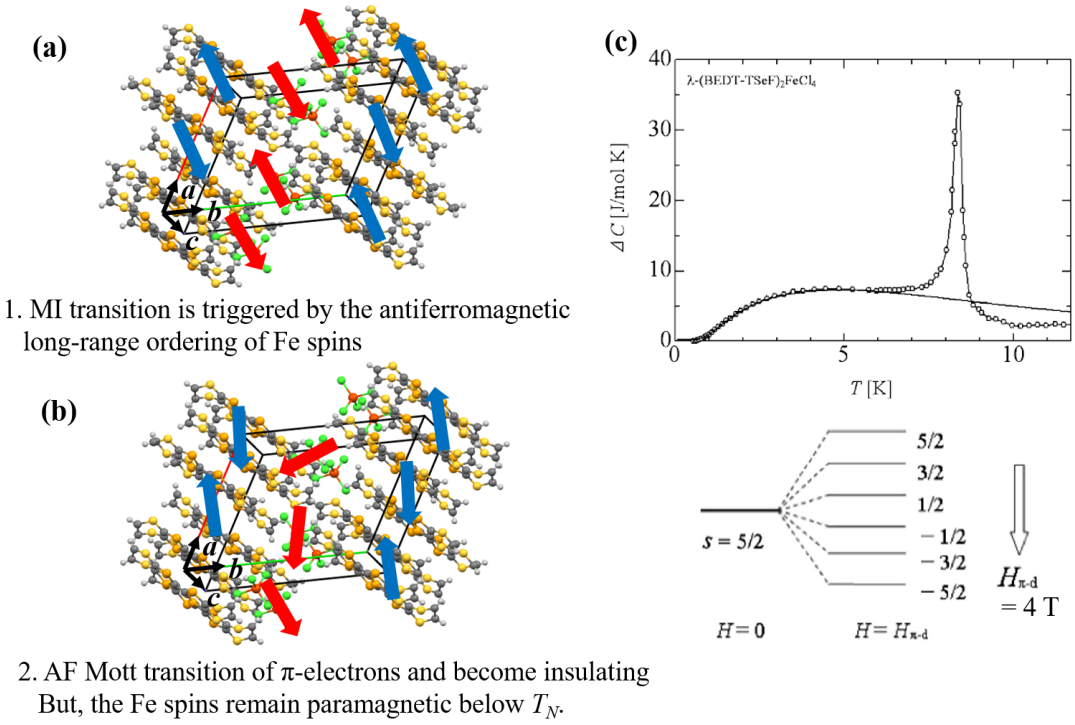

Figure 1.17: (a, b) The origin of the AFI phase models and (c) the heat capacity measurement results by Akiba *et al.* (2009) The physical Society of Japan [45]

thanks to the π-d interaction, and split the degenerated energy levels of Fe as shown at the bottom of Fig. 1.17(c). They claimed that the excess specific is due to the Schottky anomaly of the split energy levels. Recent transport, magnetic torque and magnetocaloric studies by Sugiura *et al.* seem to agree with this 'paramagnetic Fe model' [46, 47].

^{57}Fe Mössbauer measurement is reported by Waerenborgh *et al.* [48]. Above 8.3 K, the spectre presents a single line typical of paramagnetic Fe. Although the authors are supporting the paramagnetic Fe model, the Mössbauer measurements clearly indicate the AF long-range order of Fe below T_{MI} as shown as a sextets in Fig. 1.18. As temperature is decreased, the gradual increase of the hyperfine field is observed down to the lowest temperature. Doublet peaks in the sextets are also observed between 3.2 and 8 K. These fine structures of the sextets might be due to two AF spin states.

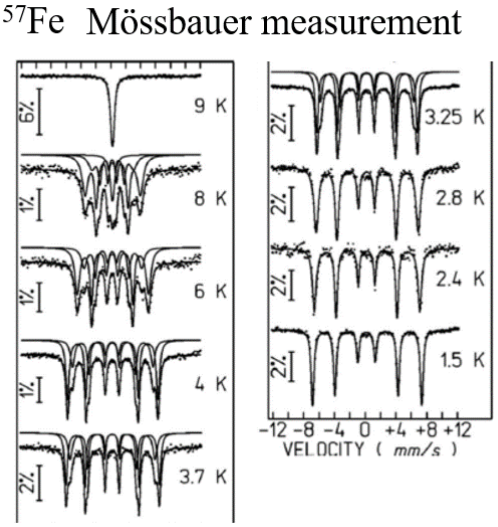

Figure 1.18: ^{57}Fe Mössbauer measurement results [48]

Many groups investigated the λ-$(BETS)_2FeCl_4$ by NMR measurements. The first ^{1}H-NMR measurement is performed by Endo *et al*, where a single peak splits into three asymmetric peaks at 70 K [49]. ^{1}H-NMR spin-echo measurement was performed by Wu *et al*. at 9 T [50]. A large slow beat structure is observed in the spin-echo decay, which originates from a large inhomogeneous local field generated by the Fe^{3+} spin moments. They also observed a discontinuous $1/T_2$ is observed at 3.5 K under high magnetic field (9 T), which is due to the change in the orientation of the Fe spins from the PM to the AFI phases. The ^{77}Se-NMR is performed by Hiraki *et al*. in the high-field PM and the FISC phases [51, 52]. When the magnetic field was applied parallel to the BETS layer, the linewidth broadening was observed at low temperature. Hiraki *et al*. suggested that the linewidth broadening is due to the charge disproportionation in the BETS layer. Although it seems that neither ^{77}Se-NMR and/or ^{13}C-NMR study of the AFI phase has been reported thus far, the NMR signal might also be very broad even for ^{77}Se or ^{13}C due to the effects of many local fields and the disproportionation of the π-electrons around the AFI phase boundary.

Besides the NMR measurements, the ESR measurements for λ-$(BETS)_2FeCl_4$ were reported by several groups [31, 41, 53]. Brossard *et al*. reported temperature dependence of the g-value and the linewidth when the magnetic field parallel to the c- and u-axis, where the u-axis is an undefined-axis. Due to the needle-shape single crystal, the u-axis could not be

determined, which is perpendicular to the c-axis. A large anisotropy was observed for both linewidth and g-factor at room temperature. The ESR linewidth is around 18 mT, and the g-factor is 2.05 when the magnetic field parallel to the u-axis. The linewidth becomes very broad, and the g-factor is 2.22 when the magnetic field parallel to the c-axis. As temperature decreased, they observed two kinds of ESR signals when the magnetic field parallel to the c-axis, where the higher g-value is about 2.6 and the lower g-value is about 2. (See Fig. 1.19) [41]. Kawamata *et al.* reported the angular- and temperature-dependence of EPR for λ-$(BETS)_2FeCl_4$ using a single crystal [53]. However, they observed only one ESR signal when the magnetic field parallel to the c-axis in contrast to the results from Brossard *et al* (See Fig. 1.19 [41]). Below T_N, the ESR signals related to the AF ordering is observed. The angular dependence of the resonance field below T_N is shown in Fig. 1.20(a). Brossard *et al.* observed the bubble-like structure, where this bubble-like structure is a rotation pattern characteristic of antiferromagnetic resonance (AFMR) [41]. From these results, Brossard *et al.* concluded that the AFMR is due to the long-range order of the Fe spins below T_N, and the AF ordering induces the localization of π-electron.

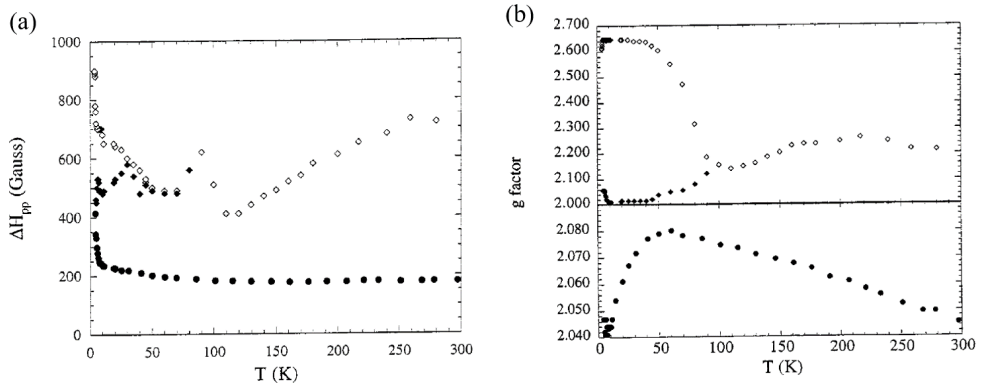

Figure 1.19: Temperature dependence of (a) ESR linewidth and (b) g-factor for the magnetic field applied along u (lower part) or c-axis (upper part) [41].

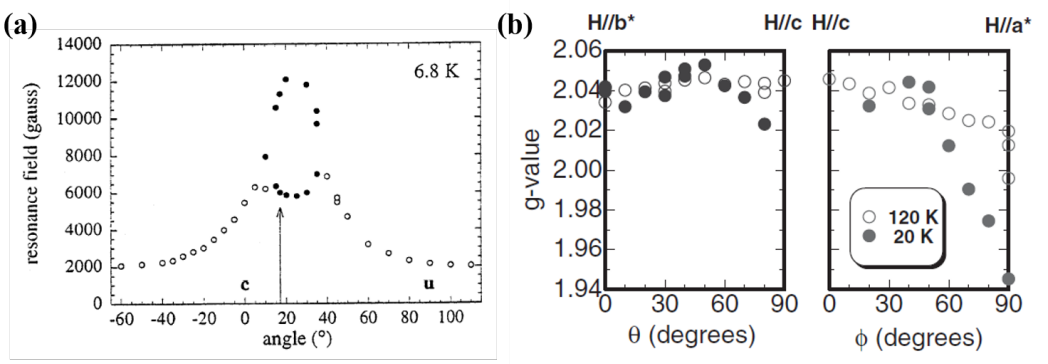

Figure 1.20: (a) Angular dependence of the resonance field at 6.8 K [41]. (b) Angular dependence of the g-value at 20 and 120 K (2006) The physical Society of Japan [53].

Suzuki *et al.* also performed the ESR measurements below T_N where the results are shown in the Fig. 1.21(b) [54]. These results are consistent with a conventional AFMR theory where the frequency-field dependence is presented in Fig. 1.21(a). Although a conventional AFMR is observed, Suzuki *et al.* proposed that the AFMR signal is due to the long-range order of π-electron. Rutel *et al.* have also performed ESR measurements below T_N, and observed conventional frequency-field plots of AFMR at the lowest temperature [55]. Around this period, intense debates whether d-electron or π-electron order first have started.

Moreover, the dielectric anomaly of λ-$(BETS)_2FeCl_4$ is also first reported at $T_{FM} = 70$ K by Matsui *et al.* (See Fig. 1.22) [56]. Matsui *et al.* observed an anomaly in the cavity response with a large dielectric constant by cavity perturbation technique at 16.3 GHz. They ascribed it to a ferroelectric transition. The microwave loss is enhanced anomalously in the range of $T_N < T < T_{FM}$, although the dc resistivity indicates a highly metallic state. Moreover, the dielectric constant along the c-axis shows a broad maximum near 30 K for 44.5 GHz (See Fig. 1.23), where the authors attributed it to a relaxor ferroelectric behavior [57]). They proposed that dielectric domains or stripes with less metallic conduction emerge inhomogeneously in the π-electron system. The X-ray diffraction results support this interpretation since the width of (007) Bragg reflection becomes broader and the peak splits at T_{FM} [58, 59].

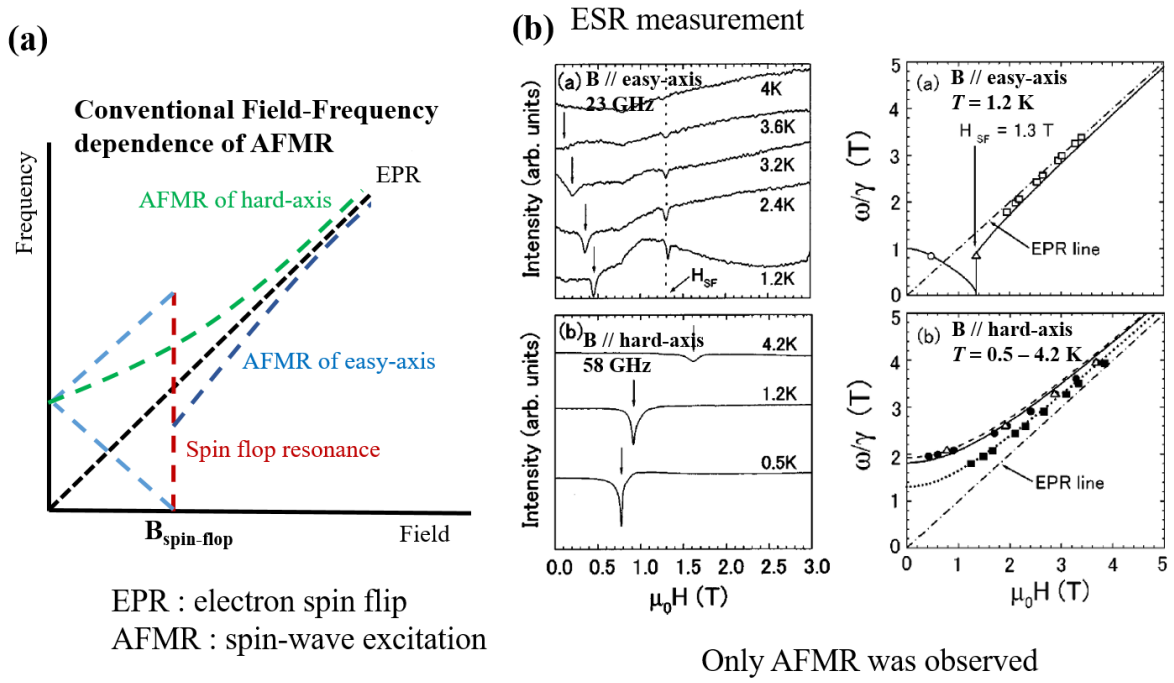

Figure 1.21: (a) Convetional field-frequency diagram of AFMR. (b) (left) the ESR spectra and (right) field-frequency dependence of AFMR [54]

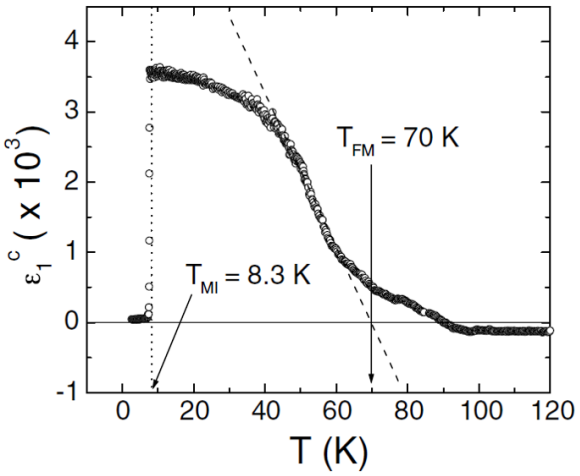

Figure 1.22: Temperature dependence of dielectric constant ε (2001) The physical Society of Japan [56]

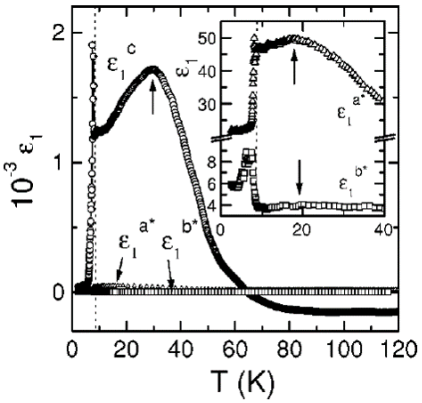

Figure 1.23: Temperature dependence of dielectric constant ε [57]

Related to the above experiments in the PM phase, Toyota and co-workers investigated $I-V$ characteristic in the AFI phase [60]. A drastic non-linear transport phenomenon was observed in the $I-V$ curve (See Fig. 1.24), where this phenomenon is known as the negative resistance effect. This observation indicates that some carrier decondensation occurs by applying electric field. They supposed that these dielectric states are intrinsic instabilities in the π-electron system, which may be strongly influenced by applying electric field.

From the above measurements, Negishi *et al.* suggest a charge ordering-induced polarization model [61]. Due to the exclusively large π-d exchange interaction between the π-orbitals at selective Se sites in BETS molecules, the charge as well as the spin of the π-electrons are expected to be localized at these Se sites. Hence, they expect a partial charge ordering

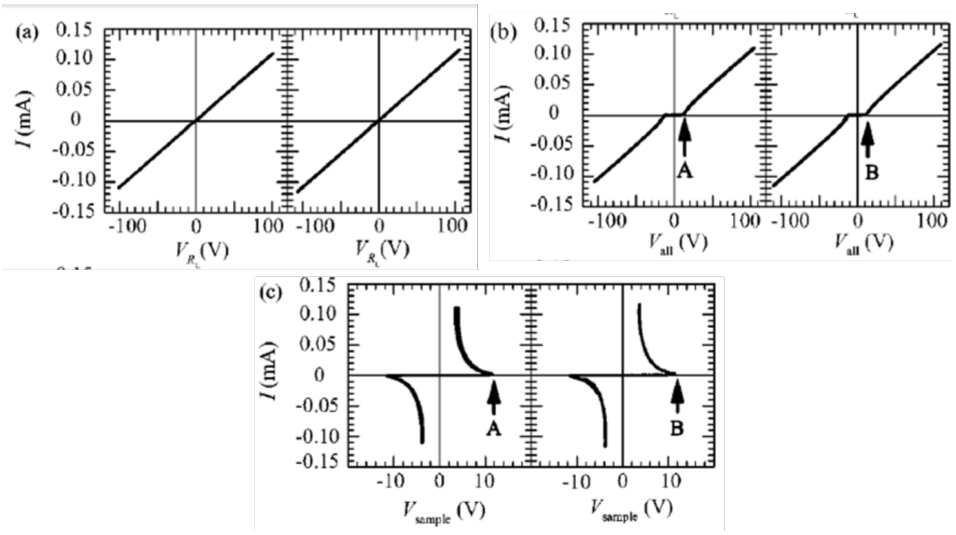

Figure 1.24: $I - V$ curve with $R_L = 1\text{M}\Omega$ measured by (left) current (I) and (right) voltage (V) at 1.5 K, where $V_{sample} = V_{all} - V_{R_L}$ [60]

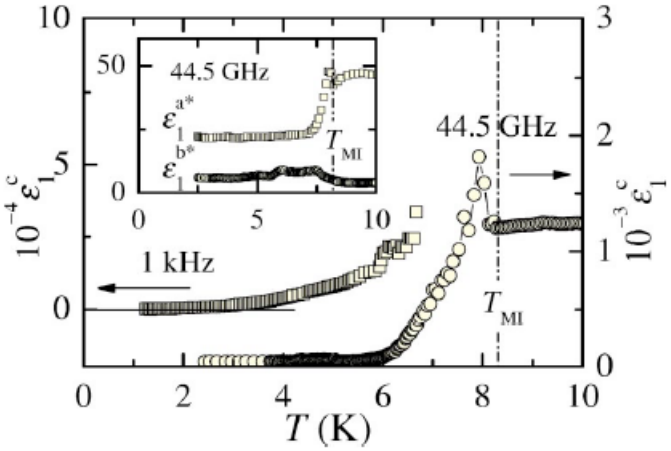

Figure 1.25: Temperature dependence of dielectric constant ε along the c-axis at 1 kHz and 44.5 GHz. The inset shows the dielectric constant ε along the a^* and b^* at 44.5 GHz. [61]

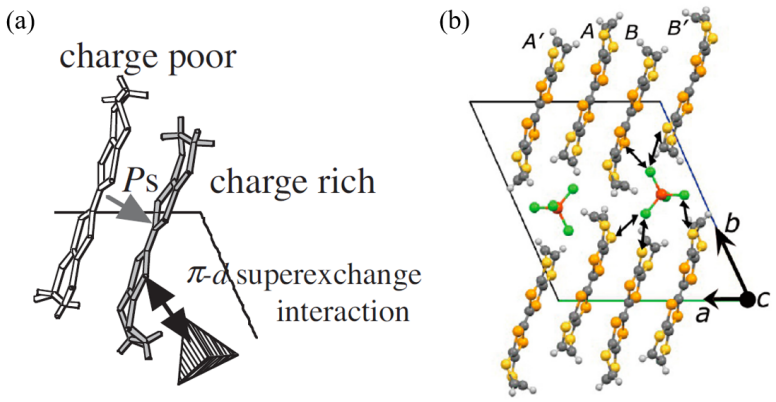

Figure 1.26: (a) Schematic picture of the charge disproportionation between BETS molecules (2001) The physical Society of Japan [59]. (b) The crystal structure of λ-$(BETS)_2FeCl_4$ where two crystallographically independent BETS molecules exist as labeled A and B [32].

occurs in BETS molecules. The charge disproportionation between BETS molecules is shown in Fig. 1.26(a) [59]. The AF order could be associated with the energy gain of the magnetic ordering of the π- and d-electrons, which overcompensates the intersite Coulomb energy in the BETS layer. They suggest that the charge ordering of the π-electrons is the origin of the AFI phase. In AFI phase, the π-electrons are localized at the Se sites, then, these π-electrons are considered to be delocalized or melted by applying the magnetic field.

Rutel *et al.* measured the high-frequency cavity response of λ-$(BETS)_2FeCl_4$ by sweeping temperature and the magnetic field, and a huge change in the cavity response was observed inside the AFI phase (See Fig. 1.27) [55]. They suggest that this anomalous behavior is due to the metastable state of the π-electron within the AFI phase. Negishi *et al.* also obtained similar results by measuring the capacitance and conductance in the AFI phase (See Fig. 1.25) [61]. A huge dielectric change was observed inside the AFI phase, which they have called 'colossal magnetodielectricity'. The magnetic field, where the divergence of the dielectric constant occurs, is similar to the results on the depolarization by Rutel *et al.*

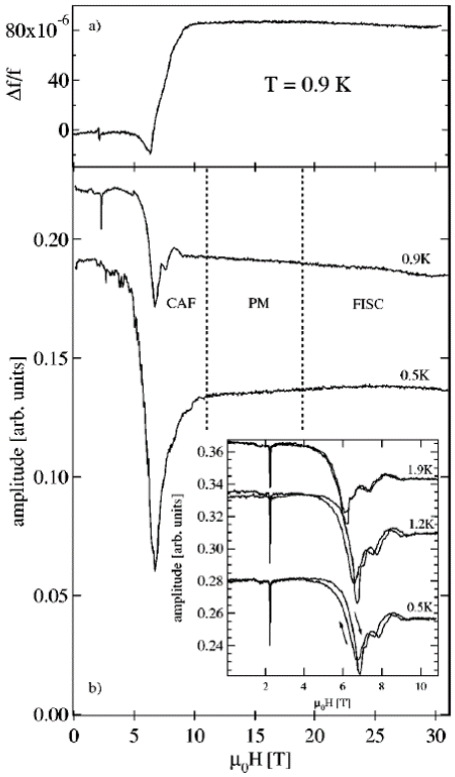

Figure 1.27: Field dependence of mm wave cavity response of λ-$(BETS)_2FeCl_4$ at 66.9 GHz for 0.9 K and 75.4 GHz for 0.5 K [55].

1.2.4 Theoretical Studies for λ-$(BETS)_2FeCl_4$

The first mechanism of the AFI phase of λ-$(BETS)_2FeCl_4$ was proposed in Ref. [41]. A Hubbard-Kondo model was introduced where four conduction bands associated with the BETS layers, and a Kondo coupling between the localized Fe spins and the conduction π-electrons were taken into account. For small Coulomb repulsion on the BETS molecule, the periodic potential due to the magnetic ordering of Fe spins opens energy gaps at the Fermi surface. And then, the fully-polarized magnetic moments destroy the periodic potential and restoring the Fermi surface by applying the magnetic field. However, a Kondo coupling of $J > 70$ K is needed to suppress the entire Fermi surface and the on-site Coulomb repulsion is empirically not small [41].

Hotta and Fukuyama introduced another model for the AFI phase [62]. They categorized the BETS system into a unified phase diagram from a mean-field calculation including the Hubbard model and the π-d interaction. λ-$(BETS)_2FeCl_4$ and λ-$(BETS)_2GaCl_4$ are very close to the MI boundary of the Mott insulator. Its ground state is influenced by the π-d interaction. They pointed out a lack of degeneracy in the energy dispersion of the two anti-bonding HOMO bands, where the lack of degeneracy is due to the molecular arrangement and the fairly large dimerization of the BETS molecules. This splitting makes it easier to form a gap between the anti-bonding band where the Fermi level is situated, which means only a small on-site Coulomb repulsion is needed to be an insulator. Hence, the MI transition at T_{MI} is proposed to be a Mott transition of the π-electrons, and then, the π-d interaction induces the long-range order of the Fe spins [62]. However, this model can not explain why the metallic state is restored by a strong magnetic field. Cépas *et al* proposed an effective Hubbard-Kondo model with Zeeman energies to resolve this problem [63]. The AFI phase is explained that the Kondo coupling drives the system into an insulating phase in order to gain some magnetic energy. The energy of a metallic state crosses that of the insulator as the magnetic field increases, leading to a first-order transition into a metallic state.

In summary, two types of mechanisms for the MI transition were proposed for λ-$(BETS)_2FeCl_4$: The spin-driven insulating mechanism and the charge-driven insulating mechanism. For the spin-driven insulating mechanism, the Fe spins become magnetically ordered due to Kondo couplings, and the periodic potential of the magnetic ordering opens a gap at the Fermi

surface and the system becomes insulating (i.e. spin-density-wave-like insulator). For the charge-driven mechanism, the π-electrons make the insulating state by the Mott transition or charge ordering, and then, the Fe spins become AF or remain paramagnetic.

Furthermore, the exchange energies in λ-$(BETS)_2FeCl_4$ are estimated by means of the extended Hückel method [38]. The exchange interactions between the π- and the d-electrons are estimated to be $J_{\pi\pi} = 448$ K, $J_{\pi d} = 14.6$ K, and $J_{dd} = 0.64$ K. From the estimated $J_{\pi d}$, the internal field created by the Fe spins is about 33 T, which is agreement with the experiment on FISC [64]. The $T_N = 6.22$ K is also deduced from these exchange couplings, which agrees with the experimental results [38].

1.3 Motivations

As mentioned in the previous section, λ-$(BETS)_2FeCl_4$ has a fascinating phase diagram, such as the PM, AFI, and FISC phase, as a function of temperature and the magnetic field thanks to the strong π-d interaction. The FISC phase of λ-$(BETS)_2FeCl_4$ is now well-understood by the Jacarino-Peter compensation mechanism [33]. However, the AFI phase of λ-$(BETS)_2FeCl_4$ is not completely understood, and is still under debate. The MI transition of λ-$(BETS)_2FeCl_4$ has been thought to be triggered by the AF long-range ordering of Fe spins. Below T_N, the Fe spins become AF ordered, and the periodic potential of the AF ordering opens a gap at the Fermi surface. But recently, theoretical studies claim that the origin of the MI transition is due to the Mott transition of the π-electrons. And then, the π-d interaction induces AF ordering of Fe spins. In contrast, Akiba *et al.* claim that the MI transition is induced by Mott transition, however, the Fe spins remain paramagnetic down to the lowest temperature from the observation a large excess specific heat below T_N [45]. Latest studies of magnetic torque measurement and magnetocaloric measurement support this paramagnetic Fe model [48, 65].

Nevertheless, the paramagnetic Fe model is not consistent with the existence of strong π-d interaction. Because, if the π-electrons become AF ordered, the Fe spins should be also AF ordered due to the strong π-d interaction. Moreover, it is important to note that no EPR is observed below T_N in the previous ESR studies [31, 41, 53]. Hence, it is clear that the paramagnetic Fe model need to be reconsidered.

A huge change of dielectric properties is observed within the AFI phase [52, 55–57, 60, 61]. There are two suggestions for the explanation of such dielectric anomalies. Negishi *et al.* proposed a charge ordering-induced polarization model, where the charge is disproportionated on one side of the BETS molecule dimer making a charge rich and poor sites [61]. Interestingly, the charge disproportionation on the BETS molecule is suggested in the PM phase by ^{77}Se-NMR measurements. It is possible that the MI transition is induced by the charge order or charge disproportionation of π-electrons. Meanwhile, Rutel *et al.* proposed that the origin of the high frequency response is due to the metastable nature of the π-electrons around the phase boundary, where the localized and conducting π-electrons coexist. Recently, Oshima *et al.* observed kink structures in the resistance below T_{MI} (See Fig. 1.28) [32].

Below T_{MI}, the resistance increases gradually with decreasing temperature. The same kind of behavior is observed by the other studies [60, 65]. These kink structures might suggest that the charge disproportionation develops and/or the π-electrons are not fully localized below T_{MI}. Thus, the gradual change of resistance in Fig. 1.28 might suggest that, as the temperature is decreased, the charge disproportionation enhances and/or the π-electrons are gradually localized. Such gradual change of the charge disproportionation or the gradual localization of the π-electrons with temperature should affect the magnetic properties of the Fe^{3+} spins through the π-d interaction, which might induce a gradual transition from the PM to the AFI phase. Mössbauer measurements clearly indicate the AF long-range ordered of Fe spins below T_{MI} [48], and the gradual increase of the hyperfine field is observed.

Although many recent studies support the paramagnetic Fe model [45], these studies never consider the lack of EPR observation below T_N or the anomalous dielectric properties in the AFI phase. It is possible that the observation of the excess specific heat is due to the charge disproportionation and/or the metastable state of the π-electrons, which affects the magnetic properties. Hence, the origin of the dielectric anomalies (i.e. the development of the charge disproportionation and/or the gradual localization of the π-electrons) and its effect on the magnetic properties need further investigation inside AFI phase.

The main purpose of this study is to investigate and clarify the AFI phase of λ-$(BETS)_2FeCl_4$ by ESR measurements. Especially, the effects of π-electrons to the AFI ground state is studied. Hence, this thesis focuses on the precise ESR measurements as a function of temperature and magnetic field around the AFI phase boundary of λ-$(BETS)_2FeCl_4$.

Furthermore, the AF easy-axis of λ-$(BETS)_2FeCl_4$ is known to be 30° from the c-axis to the b^*-axis, where the symbol * expresses the reciprocal lattice [43]. And, the AF easy-axis is important for studying AFI phase. As mentioned in the previous subsection, the needle-direction of λ-$(BETS)_2FeCl_4$ is easily defined as the c-axis. However, the a^*- and b^*-axis are difficult to define due to the needle-shape and the triclinic unit cell of the λ-$(BETS)_2FeCl_4$ as shown in Fig. 1.29. Hence, the relation between the crystal-axes and the principal-axes of the g-value is investigated. In this thesis, a new method to find the AF easy-axis from the ESR measurements will be considered from these relations.

In the meantime, the π-d interaction of this system is an indirect exchange between the π-electron on the BETS molecule and the d-electron of the Fe via a non-magnetic Cl^-. However,

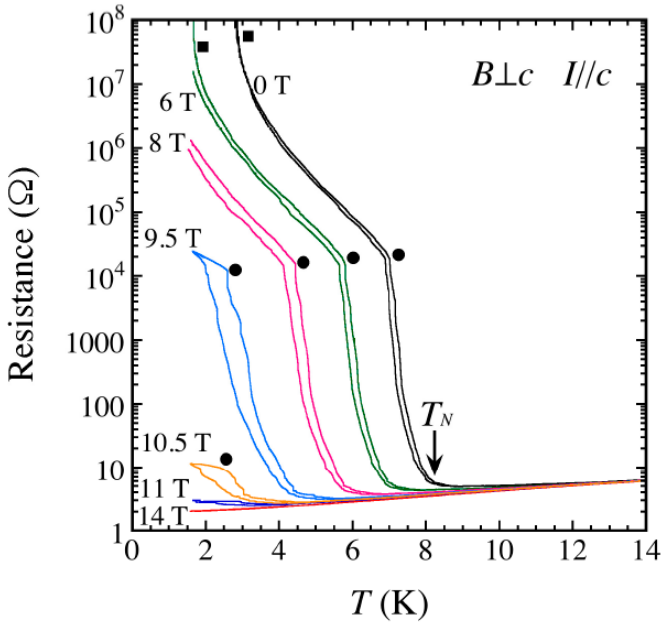

Figure 1.28: Temperature dependence of the resistance where the current is applied along the c-axis and the magnetic field perpendicular to the c-axis [32].

there are several short Se/S $\cdots$ Cl contacts between various BETS molecules and the $FeCl_4^-$ anion (See the Fig. 1.29(b)), which lead to complex exchange paths with different exchange energies between the $FeCl_4^-$ and several BETS molecules inside the unit cell [39, 66]. It is not trivial how the g-anisotropy will be affected by such π-d exchange couplings with several exchange paths. Hence, the precise angular dependence of EPR is also studied.

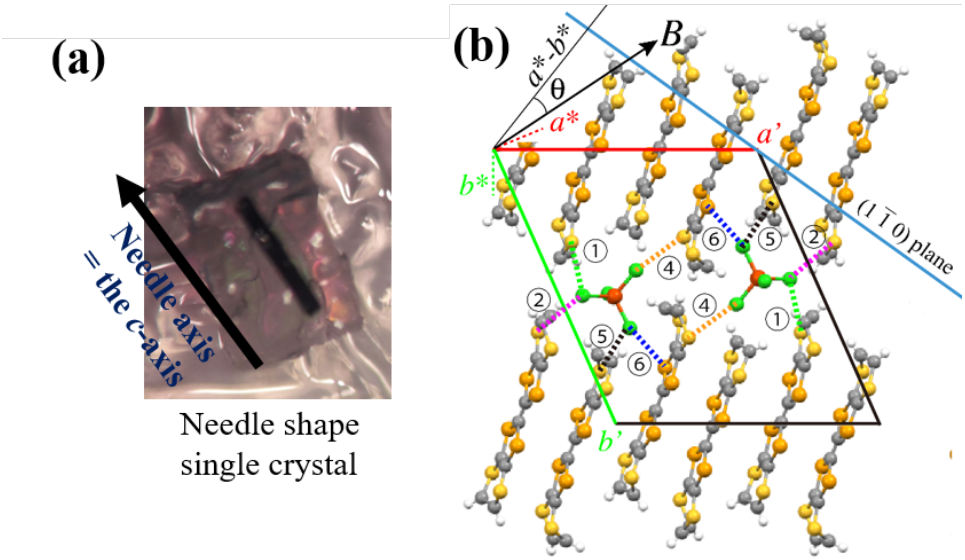

Figure 1.29: (a) The photo of λ-$(BETS)_2FeCl_4$ single crystal and (b) Crystal structure of λ-$(BETS)_2FeCl_4$ in the a^*b^*-plane

Chapter 2

Experimental

2.1 Synthesis and X-ray results

Needle-shaped single crystal of λ-$(BETS)_2FeCl_4$ were prepared by electrochemical oxidation of BETS in a mixed solvent of 90% chlorobenzene and 10% ethanol with the tetraethylammonium salt of $FeCl_4^-$ as a supporting electrolyte under argon atmosphere. Single crystal X-ray diffraction data were collected using a Rigaku HyPix-6000 AFC system with monochromated Mo Ka radiation down to 85 K. The temperature was controlled by a nitrogen gas cooling system (DX-Cs190LD, Japan Thermal Engineering Co., Ltd.) with cooling rate of 1.5 K/min. The crystal structures were solved and refined using SHELXT-2015/5 and SHELXL-2017/1 Below 20 K, single crystal X-ray diffraction data were collected by a Rigaku UltraX-6-E Imaging Plate system with monochromated Mo Ka radiation. The single crystal was mounted in the cryostat, cooled by a GM refrigerator, with cooling rate of 1.0 K/min. The crystal has a triclinic unit cell with space group $P\bar{1}$. The crystal data at room temperature and 7 K (*italic values in parentheses*) are as follows; a = 16.193 (*15.906*) Å, b = 18.577 (*18.395*) Å, c = 6.602 (*6.536*) Å, α = 98.425 (*98.652*)°, β = 96.627 (*95.706*)°, γ = 112.545 (*112.045*)°, V = 1782.14 (*1726.84*) Å^3.

2.2 Electrons Spin Resonance (ESR)

ESR spectroscopy is a method for studying materials with unpaired electrons. In classical electromagnetism, the relation between the magnetic moment and the angular momentum can be demonstrated by Einstein-de Hass and Barnett effects, where Einstein-de Hass and Barnett effects show the phenomena that a rotation of ferromagnetic rod and the magnetization induced by each other. Hence, the magnetic moments are associated with angular momentum. And thus, the magnetic moment $\vec{\mu}$ is given by

$$\vec{\mu} = \gamma \vec{L} \tag{2.1}$$

where γ is a constant known as the gyromagnetic ratio or magnetogyric ratio. In magnetic field $\vec{B}$, a magnetic moment has an energy equal to $E = -\vec{\mu} \cdot \vec{B}$. So that the energy is minimized when the magnetic field and the magnetic moment are same direction. And, there will be a torque $\vec{G}$, which is equal to

$$\vec{G} = \vec{\mu} \times \vec{B} \tag{2.2}$$

Since the magnetic field is associated with the angular momentum $\vec{L}$ by equation 2.1. A torque $\vec{G}$ is the rate of change of angular momentum, $\vec{G} = \frac{d\vec{L}}{dt}$. Hence, we can rewrite equation 2.2 as

$$\frac{d\vec{\mu}}{dt} = \gamma \vec{\mu} \times \vec{B} \tag{2.3}$$

Equation 2.3 verifies the change of the magnetic moment $\vec{\mu}$ is perpendicular to both $\vec{\mu}$ and $\vec{B}$. It means that the magnetic field $\vec{B}$ does not only induce the magnetic moments $\vec{\mu}$ to line up, but also can cause the direction of the magnetic moment $\vec{\mu}$ to precess around the magnetic field.

Now, the magnetic momentum of the electron will be considered. An electron has a negative charge $-e$ and mass m_e. In atom, the motion of an electron is orbiting with the orbital period τ around the nucleus, where the motion of an electron causes the current $I =$ -e/τ around the atom. The orbital period τ is equal to $2\pi r/v$, where v and r are the speed of an electron and the radius of the circular orbit, respectively. The angular momentum of

the electron must be defined as $\hbar$ in the ground state. Hence, the magnetic moment of the electron can be defined as

$$\mu_B = \frac{e\hbar}{2m_e} \tag{2.4}$$

where μ_B is known as the Bohr magneton. This is a convenient unit of magnetic moment.

In quantum mechanics, the orbital motion of an electron is known as the orbital angular momentum, which depends on the electronic state occupied by the electrons. And, we must consider the intrinsic angular momentum of an electron, where this angular momentum is known as the electron spin. Both angular momentums are characterized by angular momentum l and spin s quantum number, respectively. In general for electrons in atoms there may be both orbital and spin angular momenta, where orbital and spin angular momenta combine. Hence, the magnetic moment on an atom is associated with its total angular momentum $\hbar\vec{J}$, which is a sum of the orbital angular momentum $\hbar\vec{L}$ and the spin angular momentum $\hbar\vec{S}$.

$$\hbar\vec{J} = \hbar\vec{L} + \hbar\vec{S} \tag{2.5}$$

Hence, the equation 2.1 can be rewritten as

$$\vec{\mu} = \gamma\hbar\vec{J} \tag{2.6}$$

The Bohr magneton μ_B is defined as equation 2.4, which is closely equal to the magnetic moment of a free electron. The equation 2.6 is therefore considered by μ_B, where the equation 2.6 can be defined as

$$\vec{\mu} = g\mu_B\vec{J} \tag{2.7}$$

where g is called the g-factor or the spectroscopic splitting factor, which is the ratio of the magnetic moment to the angular momentum expressed in dimensionless units by means of the Bohr magneton. The free electron spin has $g = 2.0023$, usually taken as 2.00. However, it is already mentioned that both orbital and spin angular momenta combine in real atoms. Therefore, the g-factor can take different values in real atoms depending on the relative contributions of orbital and spin angular momenta, where g-factor is given by the *Landé* equation,

$$g = 1 + \frac{J(J+1) + S(S+1) - L(L+1)}{2J(J+1)} \tag{2.8}$$

Now, we will consider the energy levels of the electrons in a magnetic field, which is obtained by $E = -\vec{\mu} \cdot \vec{B}$,

$$E = g m_J \mu_B B \tag{2.9}$$

where m_J is the azimuthal quantum number and has the values $J, J-1, \cdots, -J$. For a single spin with no orbital moment we have $m_J = \pm\frac{1}{2}$ and $g = 2$. Hence, the energy levels can be split in the magnetic field by an amount $g\mu_B B$ where the energy splitting is known as *Zeeman splitting*.

The magnetic field can induce precession of that the magnetic moment at an angular frequency given by γB, where an angular frequency can be obtained by equation 2.3. And, this magnetic moments can absorb energy at this angular frequency. And, the energy of electromagnetic wave can be defined by $E = h\nu$, where h and ν are Plank's constant and frequency, respectively. Thus, the resonant absorption of energy can be observed from the electromagnetic wave tuned to the correct frequency, which is the magnetic resonance. Hence, the absorption energy ΔE is defined as

$$\Delta E = h\nu = g\mu_B B \tag{2.10}$$

The range of resonant frequency can be estimated by equation 2.10. The resonant frequency is proportional to $\frac{\mu_B}{h}$, where μ_B and h have the values 9.274×10^{-24} J/T and 6.626×10^{-34} J/Hz, respectively. And thus, the units of $\frac{\mu_B}{h}$ is

$$\frac{9.274 \times 10^{-24}}{6.626 \times 10^{-34}} Hz/T = 13.996 \times 10^9 Hz/T \tag{2.11}$$

where 10^9 Hz/T is equal to GHz/T. Actually, the magnetic filed is applied around few Tesla (T) when ESR measurements are performed. Hence, the range of resonant frequency is GHz.

Above explanation is basically for the electron paramagnetic resonance (EPR). Now, a uniaxial antiferromagnet with spins on two sublattices will be considered, where sublattices labels + and −. The thesis supposes that the magnetization $\vec{M}_+$ on sublattice + is directed along the +z-axis by an anisotropic field $B_A\hat{z}$ in Fig. 2.1. The anisotropy field results from an anisotropy energy density $U_k(\alpha) = K\sin^2\alpha$. Here α is the angle between $\vec{M}_+$ and the z-axis, hence $B_A = 2K/M$, with M is the magnitude of $\vec{M}_+$ and $\vec{M}_-$. The magnetization $\vec{M}_-$ is directed along the −z-axis by an anisotropy field $-B_A\hat{z}$. If +z is the easy-axis of

magnetization, so is −z. If one sublattice is directed along +z, the other is directed along −z (See Fig. 2.1).

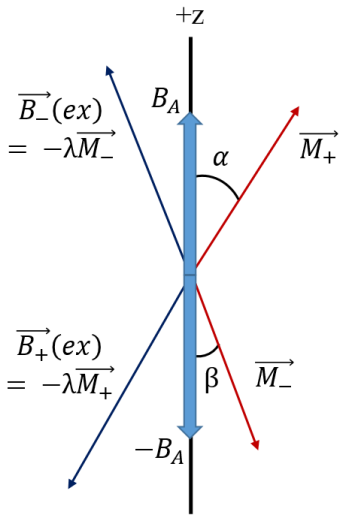

Figure 2.1: Effective field in antiferromagnetic resonance (AFMR).

The exchange interaction between the magnetizations of sublattice + $\vec{M}_+$ and − $\vec{M}_-$ is treated in the mean-field approximation. The exchange fields, $\vec{B}_+(ex)$ and $\vec{B}_-(ex)$, are defined as

$$\vec{B}_+(ex) = -\lambda\vec{M}_- \tag{2.12}$$

$$\vec{B}_-(ex) = -\lambda\vec{M}_+ \tag{2.13}$$

where λ is the molecular field constant which is absolute value (i.e., positive). (Actually, the molecular field constant is negative in antiferromanetic system.) Here $\vec{B}_+$ is the field that acts on the spins of sublattice +, and $\vec{B}_-$ acts on sublattice −. If the external magnetic field applied, the total field acting on $\vec{M}_+$ is $B_+ = \vec{B}_+ = -\lambda\vec{M}_- + B_A\hat{z}$; the total field on $\vec{M}_-$ is $B_- = \vec{B}_- = -\lambda\vec{M}_+ - B_A\hat{z}$ (See Fig. 2.1). In other word, the magnetization $\vec{B}_+$ of sublattice + sees a field $-\lambda\vec{M}_- + B\hat{z}$, and the magnetization $\vec{M}_-$ sees $-\lambda\vec{M}_+ - B\hat{z}$. The z-axis is the easy-axis.

The linearized equation of motion are defined as

$$dM_+^x/dt = \gamma[M_+^y(\lambda M + B_A) - M(-\lambda M_-^y)] \tag{2.14}$$

$$dM_+^y/dt = \gamma[M(-\lambda M_-^x) - M_+^x(\lambda M + B_A)] \tag{2.15}$$

$$dM_-^x/dt = \gamma[M_-^y(-\lambda M - B_A) - (-M)(-\lambda M_+^y)] \tag{2.16}$$

$$dM_-^y/dt = \gamma[(-M)(-\lambda M_+^x) - M_-^x(-\lambda M - B_A)] \tag{2.17}$$

where $M = M_+^z$, $-M = M_-^z$. And, M_+ and M_- are defined as $M_+^x + iM_+^y$ and $M_-^x + iM_-^y$, respectively. Then the above equations, 2.14 $\sim$ 2.17, become for time dependence $\exp(-i\omega t)$,

$$-iwM_+ = -i\gamma[M_+(B_A + \lambda M) + M_-(\lambda M)] \tag{2.18}$$

$$-iwM_- = i\gamma[M_-(B_A + \lambda M) + M_+(\lambda M)] \tag{2.19}$$

The equations 2.18 and 2.19 are have the solutions with the exchange field $B_E = \lambda M$: If $B < B_{sf}$, where B_{sf} is the spin-flop field, the AFMR frequency ν is given by

$$\omega/\gamma = \sqrt{2B_E B_A} \pm B \tag{2.20}$$

If $B > B_{sf}$, the AFMR frequency f is given by

$$\omega/\gamma = \sqrt{B^2 - 2B_E B_A} \tag{2.21}$$

The equations 2.20 and 2.21 are the solutions for the easy-axis mode of AFMR. If external magnetic field B is applied perpendicular to the z-axis (i.e., perpendicular to the easy-axis), the AFMR frequency is given by

$$\omega/\gamma = \sqrt{2B_E B_A + B^2} \tag{2.22}$$

The conventional field-frequency dependence of AFMR is presented from the equations 2.20, 2.21, and 2.22 in Fig. 2.2 [67]. The black dotted line is the EPR line by $g\mu_B B = h\nu$. Hence, the AFMR and EPR show completely different results.

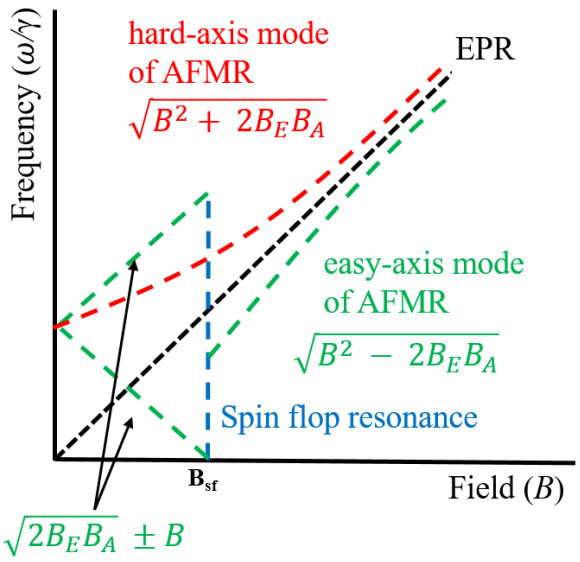

Figure 2.2: The conventional field-frequency dependence of AFMR.

2.2.1 Cavity perturbation technique

The resonant cavity is a good tool for high sensitivity measurements. The resonant cavity has some merits to have high sensitive signals and to control the electromagnetic environment (i.e. AC electric field E and AC magnetic field H) inside cavity. At resonance, the cavity is resonating microwave oscillations, which is an interference pattern from superposed microwaves reflected from the cavity walls. The resonating oscillation is related to the cavity size and shape, where the standing wave configuration is called modes. When $E_z = 0$, which modes are called as TE modes, and TM modes are called when $H_Z = 0$. We used cylindrical cavities with TE mode in this study. The general cylindrical TE_{mnp} modes, the subscripts n, m, and p refer to the number of half cycle variations in a cylindrical coordinate (radial r, angular ϕ, longitudinal z), are given by

$$H_r = \frac{k_z H_0}{(k_c^2 + k_z^2)^{1/2}} J'_m(k_c r) \cos m\phi \cos k_z z \tag{2.23}$$

$$H_\phi = -\frac{m k_z H_0}{(k_c^2 + k_z^2)^{1/2}} \frac{J_m(k_c r)}{k_c r} \sin m\phi \cos k_z z \tag{2.24}$$

$$H_c = \frac{k_c H_0}{(k_c^2 + k_z^2)^{1/2}} J_m(k_c r) \cos m\phi \sin k_z z \tag{2.25}$$

$$E_r = -m(\frac{\mu}{\epsilon})^{1/2} H_0 [\frac{J_m(k_c r)}{k_c r}] \sin m\phi \sin k_z z \tag{2.26}$$

$$E_\phi = -(\frac{\mu}{\epsilon})^{1/2} H_0 J'_m(J_c r) \cos m\phi \sin k_z z \tag{2.27}$$

$$E_z = 0 \tag{2.28}$$

$$k_c = \frac{(k_c a)_{mn}}{a}, k_z = \frac{p\pi}{d} \tag{2.29}$$

where $J_m(k_c r)$ is the Bessel function of m-th order, $J'_m(k_c r)$ is the derivative Bessel function of m-th order, and a, d are a cavity radius and length, respectively. When we design the resonant cavity, the Quality (Q) factor must be considered. When the Q of a resonant cavity arises only from the ohmic losses in the walls it is called the unloaded quality factor Q_u. And, the Q factor for the TE_{mnp} cylindrical mode is given by

$$Q_u \frac{\delta}{\lambda} = \frac{(1/2\pi)[1 - m/(k_c a)'^2_{mn}][(k_c a)'^2_{mn} + (p\pi a/d)^2]^{2/3}}{(k_c a)'^2_{mn} + 2(2a/d)(p\pi a/d)^2 + (1 - 2a/d)[mp\pi a/d(k_c a)'_{mn}]^2} \tag{2.30}$$

where δ is skin depth, and λ is wavelength. The results for TE_{0np} modes are shown in Fig. 2.3(a), where the TE_{0np} mode has a maximum value of Q when the cavity length d equals the diameter $2a$.

The schematic figures of typical TE_{0np} modes are shown in Fig. 2.3(b). In general, H-field coupling is used to observe ESR. Provided that a sample placed inside a resonant cavity acts as a small perturbation of the H-field distribution within the cavity, we can determined the complex electrodynamic response of the sample from the changes of the Q factor and the resonance frequency (f_0). The magnitude A and phase ϕ of the electromagnetic waves in the resonant cavity is related to the resonance frequency f_0 and the Q factor.

$$|A(f)|^2 = \frac{A_0^2}{(f_0/2Q)^2 + (f - f_0)^2} \tag{2.31}$$

$$\phi = -\arctan \frac{2(f - f_0)}{f_0/2Q} \tag{2.32}$$

where A_0 is the notional amplitude of the field supplying energy of the cavity and f is the frequency used. Hence, the phase and amplitude of mm-wave transmitted can be monitored through a resonant cavity containing the sample under investigation.

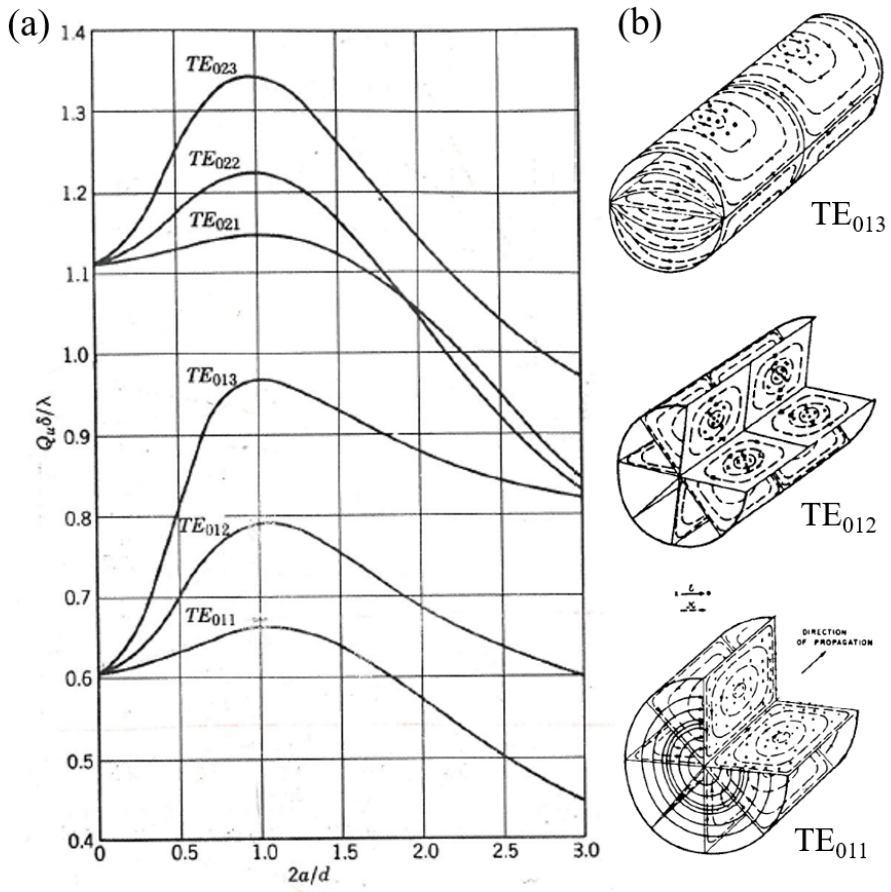

Figure 2.3: (a) $Q_u(\delta/\lambda)$ versus $2a/d$ for several TE_{0np} modes (b) Schematic figures of typical resonant modes

2.2.2 X-band ESR measurements

The conventional X-band ESR system uses the magnetic field modulation technique for high-sensitive measurements. The static magnetic field B is applied with an AC magnetic field ΔB_{AC} whose amplitude is smaller than the resonance absorption line width, which is called the magnetic field modulation technique [68]. The ESR observation with the magnetic field modulation can offer signals that are proportional to the absorption line slope. Hence, the ESR signal is observed as a first-derivative lineshape [68]. In this study, all the observed ESR spectra have a Lorentzian lineshape. The obtained ESR spectra were therefore fit with the first-derivative of a Lorentzian lineshape,

$$L'(B) = \frac{16 I'_m (\frac{B_0 - B}{0.5\Delta B_{pp}})}{[3 + (\frac{B - B_0}{0.5\Delta B_{pp}})^2]^2} \tag{2.33}$$

where I'_m is the peak-to-peak intensity of the ESR signal, B is the external field, B_0 is the resonance field and ΔB_{pp} is the peak-to-peak linewidth. B_0 and ΔB_{pp} were obtained from the fitting of the ESR spectra using the least squares method of the equation 2.33.

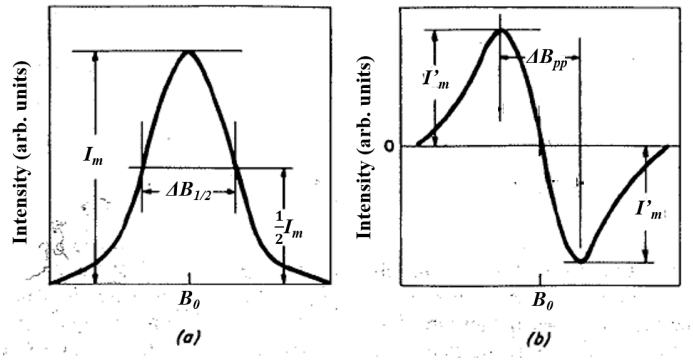

Figure 2.4: (a) Typical ESR signal with Lorentzian lineshape and (b) its derivative lineshape.

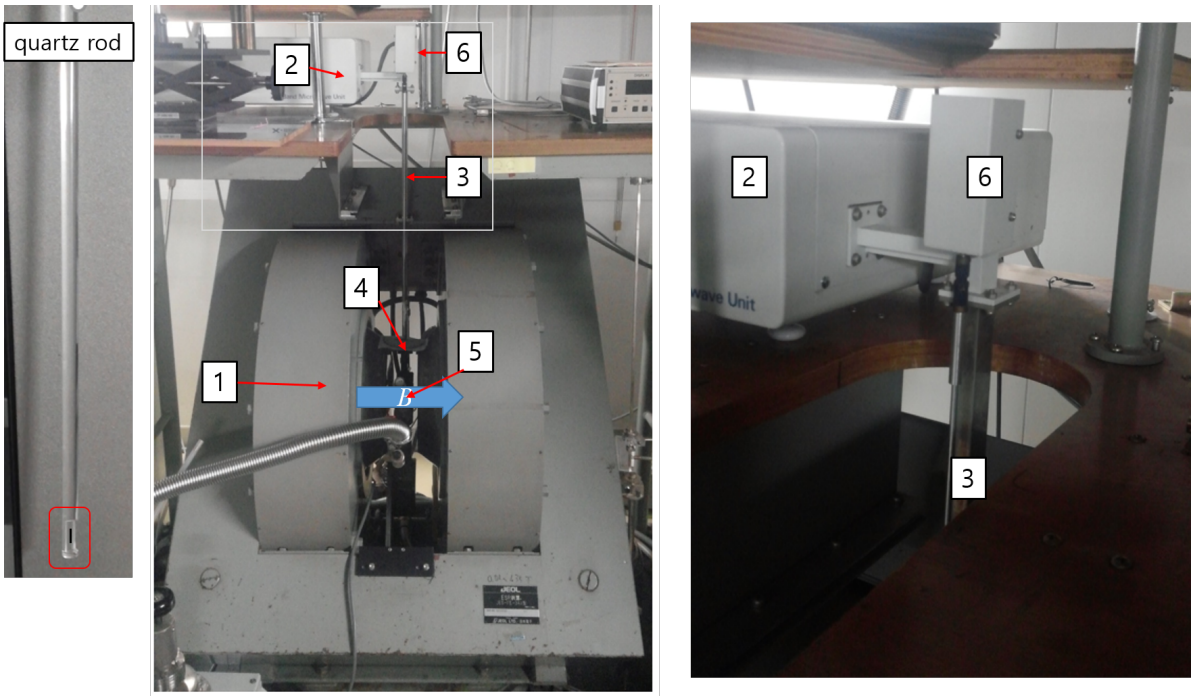

Figure 2.5: 1. Electromagnet, 2. Spectrometer, 3. Waveguide, 4. Sample tube holder, 5. Resonant cavity, 6. Step motor for iris The sample tube is the quartz rod, where the sample is located in red rectangle.

The X-band ESR system (JEOL-JES-RE3X, 9-10 GHz) consists of the electromagnet, the spectrometer, the waveguide, the resonant cavity, and the iris (See Fig. 2.5). The magnetic field is applied perpendicular to the quartz rod (sample holder), where the magnetic field range is between 50 and 1350 mT. The gunn oscillator generates microwave. The waveguide connects between the resonant cavity and directional coupler. The directional coupler has two waveguides which are joined so that their tube-axes intersect on their broad surfaces (i.e., cross-shaped coupling holes). When the angular and temperature dependence of ESR are performed, the sample is mounted on a quartz rod, and inserted in the cylindrical cavity with TE_{011} mode [68]. The sample was set on the quartz rod using a silicon grease.

Sample configurations in measurements are shown in figure 2.6(a) and 2.6(b). In the figure 2.6, the θ and the ϕ are the angles between the magnetic field and $a^* - b^*$-axis or $-b^*$-axis, respectively [69]. The magnetic field was applied horizontally to the quartz rod, and the angular dependence of ESR was measured by rotating the quartz rod. The error range was about few degrees.

The crystal plane of the sample was checked beforehand by the X-ray diffraction method. We chose a single crystal where the largest surface of the needle-shaped crystal corresponds to

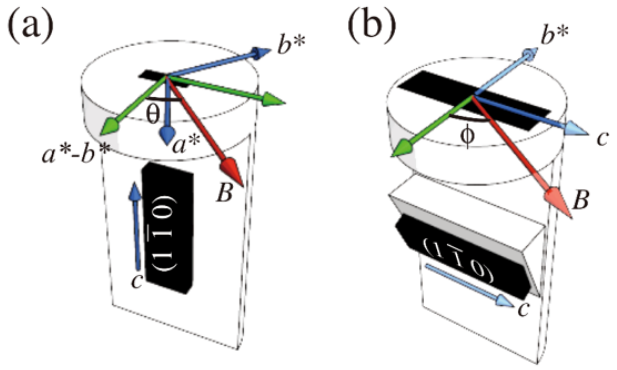

Figure 2.6: Sample configurations in measurements for B // a^*b^*-plane and B // b^*c-plane, respectively [69].

the (1 $\bar{1}$ 0)-plane. Hence, the $\theta = 0°$ correspond to the $a^* - b^*$-axis for the a^*b^*-plane rotation. Note tote that a^*b^*-axis of the reciprocal lattice is perpendicular to the bc-/ac-plane of the real lattice, respectively. The same sample on the triangular prism-shaped polyethylene jig for applying the magnetic field parallel to the b^*c-plane. For this rotation, the direction of the magnetic field is defined by the angle ϕ, where $\phi = 0°$ is set to the $-b^*$ direction i.e. the angles $\phi = 90°$ and $= 180°$ correspond to the c- and the b^*-axis, respectively. When the EPR and AFMR were measured, the magnetic field was swept linearly over the range between 50 and 550 mT for EPR, and between 550 and 1350 mT for AFMR measurements.

When the temperature dependence of ESR was measured, the temperature was controlled by a liquid-helium flow cryostat (Oxford Instruments). A thermocouple was used as a temperature sensor. The initial cooling rate was about 3 K/min, and the temperature range was between 4.3 K and room temperature.

2.2.3 High-field ESR measurements

The high-field ESR measurements were performed using the millimeter vector network analyzer (AB millimetre, MVNA-8-350-1-2). The frequency range is between 33 and 220 GHz (Q-band : 33−50 GHz, V-band : 50−75 GHz, W-band : 75−110 GHz and G-band : 140−220 GHz). The MVNA is based on two yttrium-iron-garnet (YIG) oscillators, master and slave, which are continuously tunable between 8 and 18 GHz. The YIG oscillators are phase locked and the slave YIG follows the frequency of the master. The master YIG is set to a frequency ($Freq1$) between 8 and 18 GHz, and the microwave is sent to the harmonic generator, which acts as a transducer, emitting harmonic electromagnetic waves which are then sent to the measurement probe. The harmonic generator (Schottky diode) generates multiplied frequency of $Freq1$, $Freq_{mm} = N \times Freq1$ with $N = 1, 2, 3, \cdots$. Meanwhile, the slave YIG oscillates at $Freq2 = Freq1 - f$, where f is a fixed frequency. The signal from the slave is sent to the harmonic mixer. The harmonic mixer mixes $NFreq2$ with the signal received from the probe, i.e. $Freq_{mm}$, and downconvert the signal to Nf which is about 34 MHz, and its amplitude and the phase are obtained from the vector receiver.

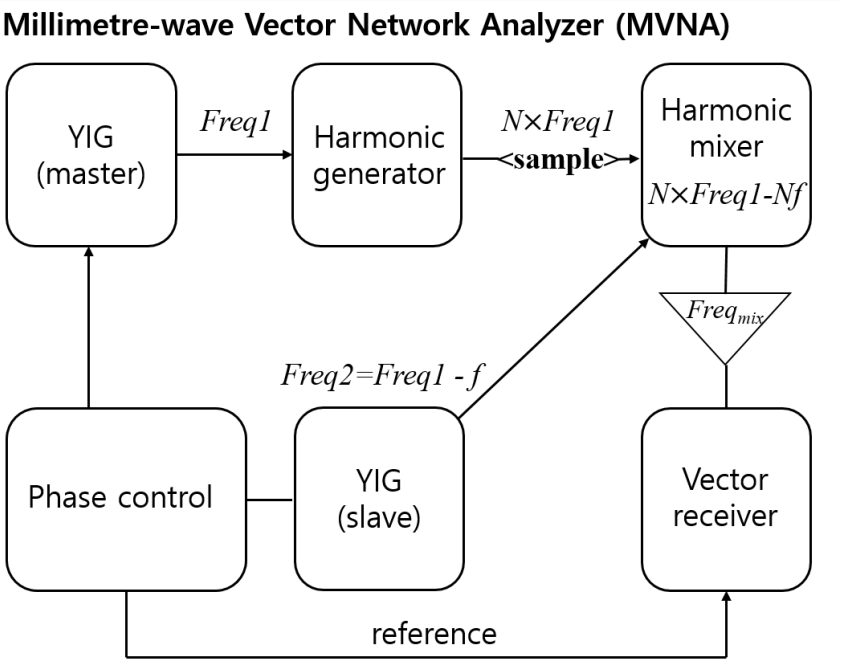

Figure 2.7: Schematic diagram of Millimetre-wave Vector Network Analyzer

$$Freq_{mix} = |NFreq1 \pm N(Freq1 - f)| = Nf \tag{2.34}$$

Two YIG are phase locked to each other so that the phase noise of two YIG is canceled and the phase of the signal from the experiment is preserved:

$$\phi_{mix} = |N\phi_1 - N\phi_2 + \delta\phi| \tag{2.35}$$

where ϕ_1 and ϕ_2 are phases of two YIG and $\delta\phi$ is the phase shift due to the experiment. In the vector receiver, $Freq_{mix}$ is downconverted by mixing signals derived from the source in order to keep the phase information. Hence, the amplitude and the phase information of mm-wave transmission can be obtained by the MVNA with the wide frequency range of 33 to 220 GHz.

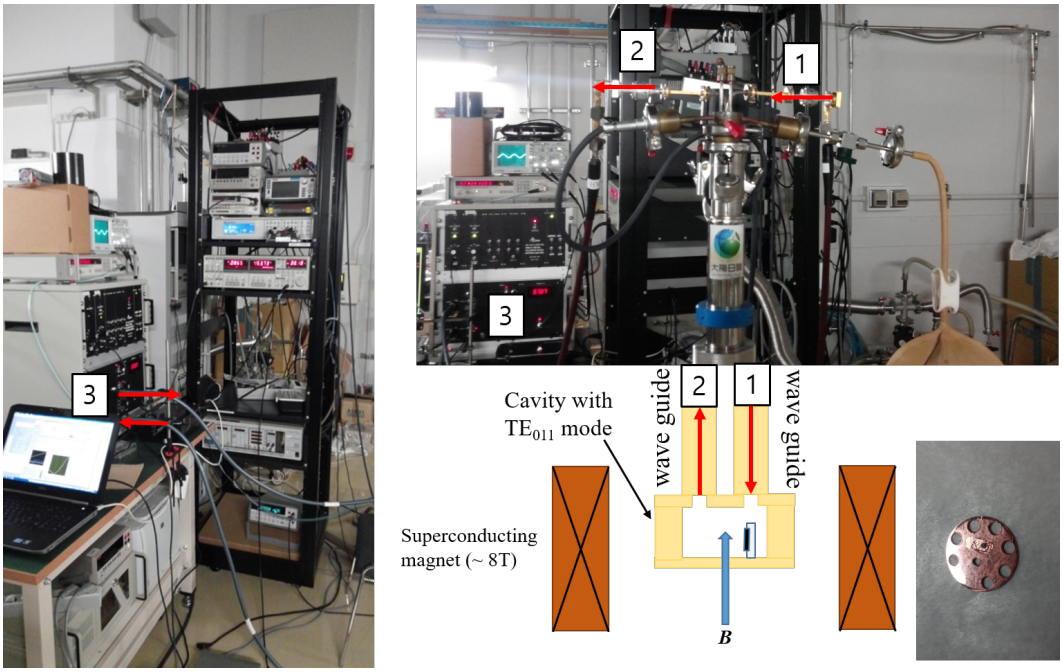

Figure 2.8: 1. Harmonic mixer, 2. Harmonic generator, 3. Vector Network Analyzer system. The cylindrical resonant cavity with TE_{011} mode. The red arrows are the direction of wave.

For the high-field ESR measurements, the magnetic field ($\sim$ 8T) was applied perpendicular to the plate of the cylindrical cavity. And, the sample was mounted on the bottom-plate of the cylindrical cavity with the polyethylene jig. (See Fig. 2.8). The sample was set on the bottom-plate of the cylindrical cavity with TE_{011} mode using a silicon grease. The sample

configuration for measurements is presented in Fig. 2.9(right). The Fig. 2.9 shows that the sample with polyethylene jig mounted on the bottom-plate of the cavity along the easy- and the crystal-axes. The information of the easy-, the a^*, and the b^*-axis is obtained from the angular dependence of EPR in the a^*b^*- and b^*c-planes (There is the detail explanation in the X-band ESR measurements section). In contrast, the c-axis is easily defined from the needle-axis.

Figure 2.9: (left) The photo is the configuration in measurement for B // the easy-axis, where the red circle is the position of the sample. (right) Sample configurations for measurements B // easy-, c, a^*, and b^*-axes.

Chapter 3

ESR measurements of λ-$(BETS)_2FeCl_4$

3.1 X-band ESR measurements ($B \leq B_{sf}$)

3.1.1 Results

The temperature and the angular dependence of ESR measurements are performed below the spin-flop field B_{sf}∼1.2 T. The measurement area covered by X-band ESR is shown as a red rectangle in Fig. 3.1.

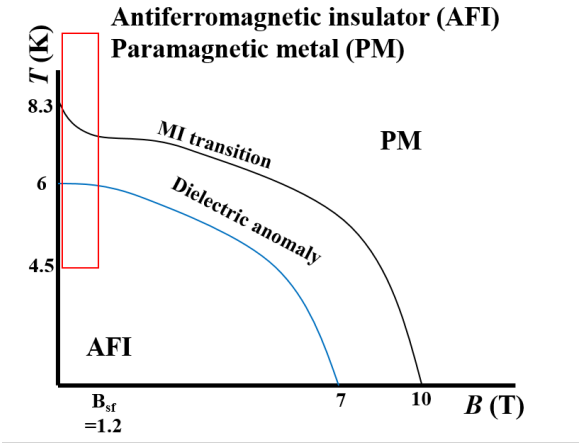

Figure 3.1: Phase diagram of λ-$(BETS)_2FeCl_4$ as a function of magnetic field and temperature.

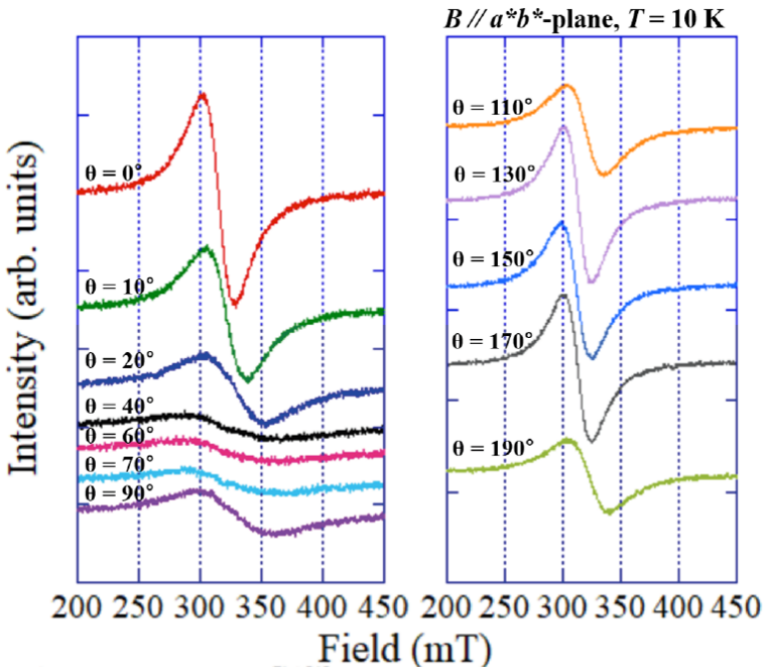

Figure 3.2: Angular dependence of the EPR signal at 10 K. the θ is the angle between the magnetic field and [1 $\bar{1}$ 0]-axis in the a^*b^*-plane.

The typical angular dependence of the ESR spectra at 10 K is presented in Fig. 3.2. Only a single EPR line is observed, which is consistent with previous ESR report [53]. The raw EPR signal is observed as a first derivative lineshape because of the filed modulation method is employed. Hence, the resonance field and the peak-to-peak EPR linewidth are obtained from the first derivative of a Lorentzian lineshape (See Eq. 2.33). In Fig. 3.2, the resonance field shifts with the direction of the magnetic field. The angle θ is the angle between the magnetic field and the [1 $\bar{1}$ 0]-axis in the a^*b^*-plane.

The g-value of EPR is obtained from $g = \frac{\mu_B B_{res}}{h\nu_{res}}$, where μ_B is the Bohr magneton, h is the Planck's constant, B_{res} is the resonance field, and ν_{res} is the resonance frequency. The angular dependences of the EPR signal in the a^*b^*-plane are obtained at 10, 30, 100, 150, 230, 270, 280, and 300 K, and its g-value and EPR peak-to-peak linewidth are shown in Fig. 3.3(a) and 3.3(b), respectively. The $g_{\max}$ and the $g_{\min}$ for 300 K are about 2.05 and 2.04, and the principal-axes of the g-tensor correspond to the b'- and the a'-axes, respectively. Note that the a'- and b'-axes are defined as the projection of the a- and the b-axes in the a^*b^*-plane, respectively. (See Fig. 3.4) The principal-axes are related to the ligand field of the $FeCl_4$ anion where $g_{\max}$ is along the Fe-Cl bond parallel to the b'-axis as shown in Fig 3.4.

As the temperature is lowered, two minimum g-values are observed around $\theta = 30$ and 90°, starts to develop below 270 K (See Fig. 3.3(a)). Two minimum g-values at 10 K are about 1.98 for $\theta = 30°$ and 1.99 for $\theta = 90°$, respectively. The maximum g-value for $\theta = 130°$ is about 2.05 at 300 K. The maximum g-value increases drastically to 2.11 at 30 K. And then, the angle θ for the maximum g-value shifts towards $\theta = 150°$ at 10 K (See Fig. 3.3(a)). The maximum and the minimum of the EPR linewidth are observed nearby the a'- and b'-axes, respectively. The EPR linewidth becomes extremely broad at 10 K along the a'-axis (See Fig. 3.3(b)), where the a'-axis is parallel to the conducting plane.

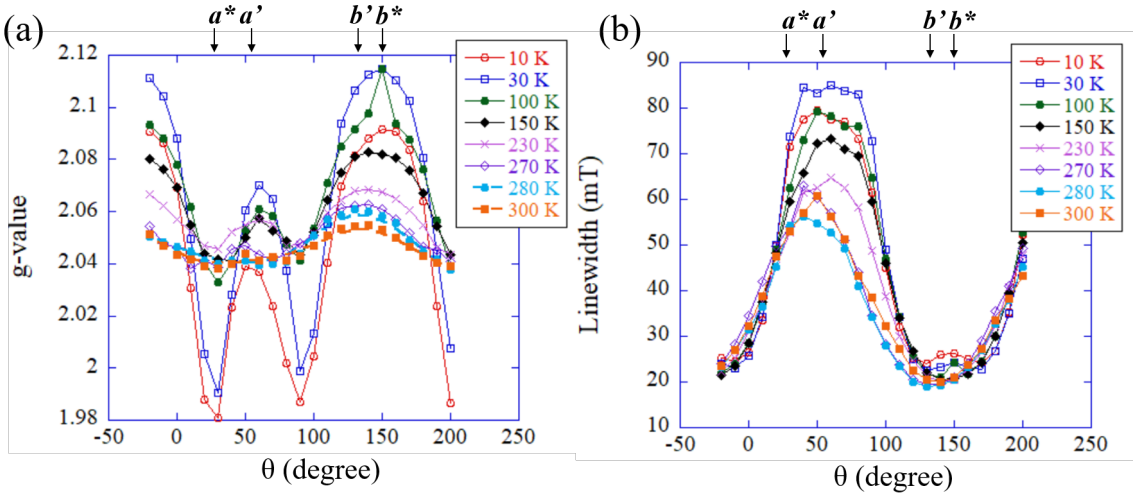

Figure 3.3: Angular dependence of (a) the g-value and (b) the peak-to-peak linewidth from the EPR in the a^*b^*-plane

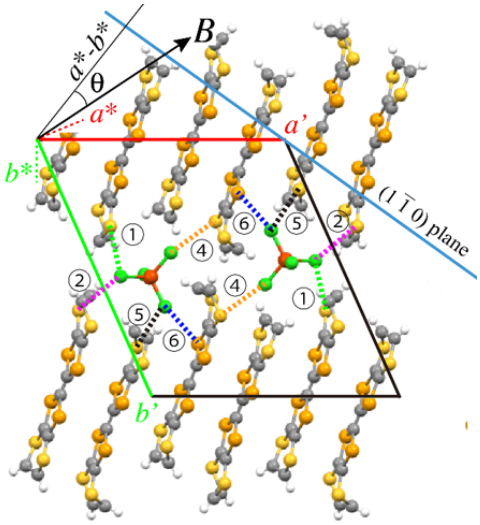

Figure 3.4: Crystal structure of λ-$(BETS)_2FeCl_4$ in the a^*b^*-plane.

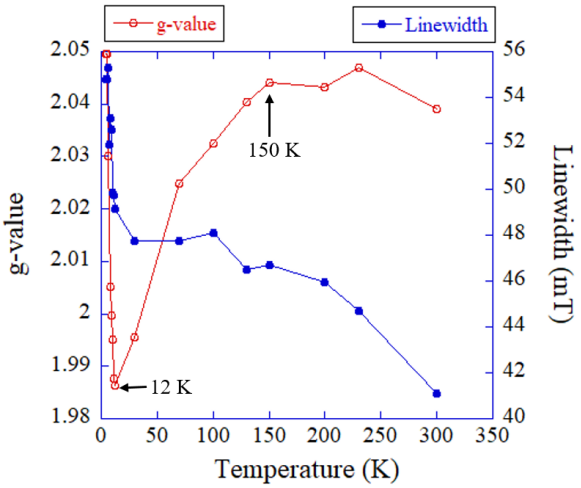

Figure 3.5: Temperature dependence of the g-value and the peak-to-peak linewidth at $\theta = 20°$

The temperature dependence of the EPR signal shows a distinct feature at $\theta = 20°$, where the $\theta = 20°$ is around the minimum g-value at 10 K (See Fig. 3.3). In Fig. 3.5, the g-value at $\theta = 20°$ starts to decrease below 150 K, and sudden increase is observed below 12 K. As the temperature is lowered, the EPR linewidth gradually increases, and a steep EPR linewidth broadening is observed below 12 K.

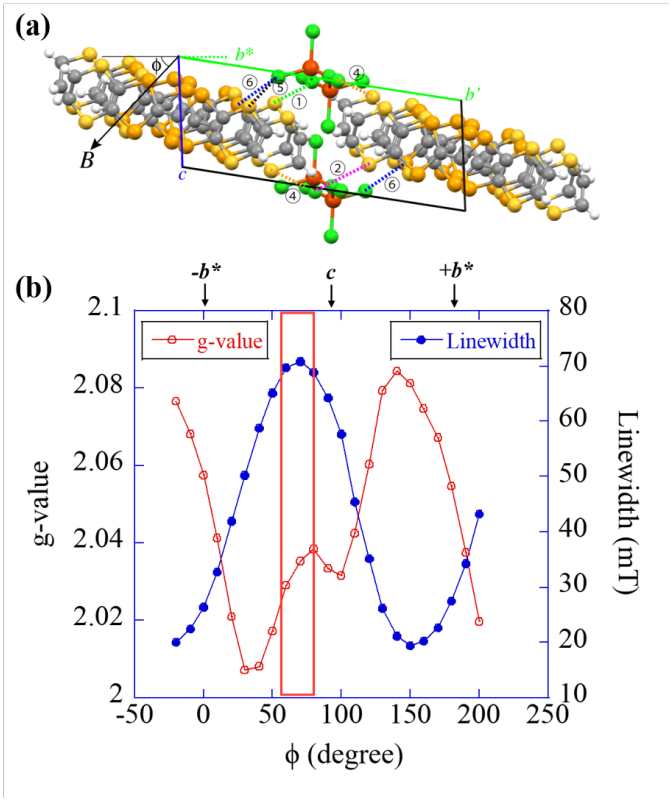

Figure 3.6: (a) Crystal structure of λ-$(BETS)_2FeCl_4$ and the direction of the magnetic field projected to the b^*c-plane. (b) Angular dependence of the g-value and linewidth within the b^*c-plane at 10 K. The red box is the area where AFMR is observed at 4.5 K.

The crystal-axes can be identified by the minimum and the maximum of the g-values within the a^*b^*-plane. The b^*-axis corresponds to the maximum g-value, and the a^*-axis to one of the minimum g-value at about 120° from the b^*-axis. (See Fig. 3.3(a)). Hence, the b^*-axis is defined from the g-value in the a^*b^*-plane rotation, and it is possible to perform the EPR measurement in the b^*c-plane by using a triangular prism jig. The angle ϕ indicates the direction of the external magnetic field, and the sample was set so that the direction of $\phi =$ 90 and 180° are along the c- and b^*-axes, respectively (i.e., ϕ is the angle between $-b^*$-axis and the magnetic field). The direction of the magnetic field in the crystal structure is shown

in Fig 3.6(a). The angular dependences of the g-value and the linewidth within the b^*c-plane measured at 10 K as shown in Fig. 3.6(b)). In this plane, an asymmetric angular dependence of the g-value with two different minima is observed at 10 K, where the g-values are 2.01 and 2.03 at $\phi = 30$ and 100°, respectively. Similarly to the results of the a^*b^*-plane rotation, a broad EPR linewidth is observed between the first and the second minimum of g-values.

It is known from the magnetic torque measurement by Sasaki *et al.* that the AF easy-axis of λ-$(BETS)_2FeCl_4$ is tilted about 30° from the c-axis to the b^*-axis [43]. This angle of the AF easy-axis corresponds to $\phi = 60°$, where a linewidth maximum of the EPR line is observed as shown in Fig. 3.6(b). As shown in Fig. 3.7(a), conventional EPR is observed around 320 mT using X-band ESR system ($\sim$ 9GHz), and two AFMR: easy-axis mode and spin-flop resonance, are expected to be observed at higher field. Hence, the angular dependence of the ESR spectra between 550 and 1350 mT at 4.5 K, namely in the AFI phase, is presented in Fig. 3.7(b). Two ESR signals are observed around 950 and 1150 mT at $\phi = 60°$, and more clear and stronger signals are observed for $\phi = 65°$ (See Fig. 3.7(b)). As explained later, these two ESR signals can be attributed to two AFMRs: easy-axis mode and spin-flop resonance. At $\phi = 55$ or 70°, the signal intensity decreases rapidly since the magnetic field is tilted from the AF easy-axis, and the two AFMR lines merge to a single line. Then, AFMR completely disappears at $\phi = 50$ and 80°. This observation suggests that the two AFMR signals only appear for the magnetic field orientation between $\phi = 60$ and 65°. Hence, the direction of the AF easy-axis corresponds to the $\phi = 60 \sim 65°$. This result is consistent with the previous magnetic torque report [43].

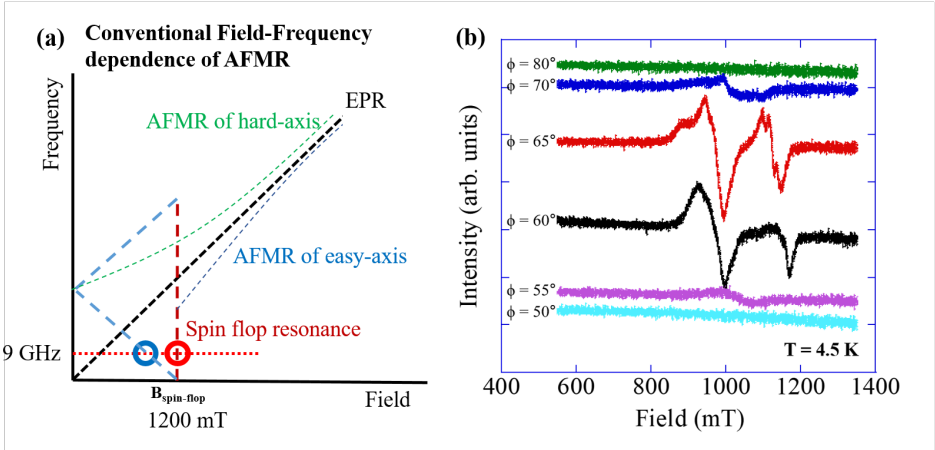

Figure 3.7: (a) Conventional field-frequency AFMR. (b) ESR spectra in the high field region for $\phi = 50$, 55, 60, 65, 70, and 80° at 4.5 K.

In general, two AFMR signals can be observed in the low-frequency region when the magnetic field is applied parallel to the AF easy-axis. If the magnetic field is tilted from the AF easy-axis, the AFMR mode changes to the hard-axis mode, and the AFMR signals can not be observed in the low-frequency region (See Fig. 3.7(a)). Therefore, angular dependence of AFMR has a characteristic bubble-like structure around the AF easy-axis. And, the center of the bubble structure corresponds to the AF easy-axis.

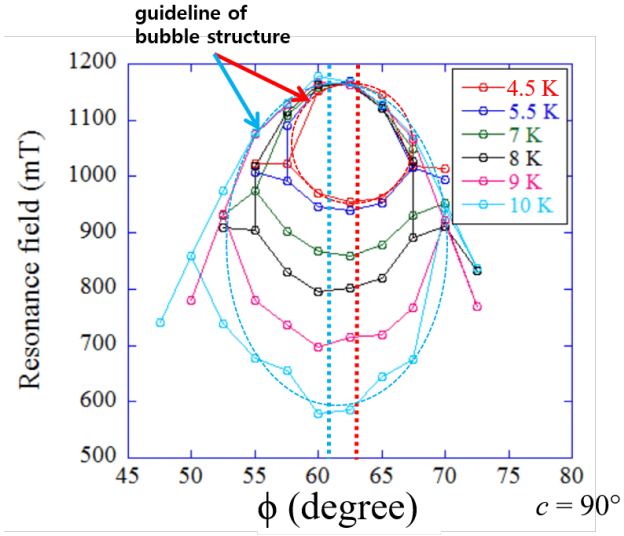

Figure 3.8: Angular dependence of AFMR in the b^*c-plane.

The angular dependence of ESR nearby the easy-axis with different temperature are shown in Fig. 3.8. It has a typical bubble-like structure, and it can be concluded that the two ESR are AFMR. The red circle is the guideline for 4.5 K and the sky blue circle is the guideline for 10 K. Surprisingly, the center of bubble structure shifts with temperature. It means that the AF easy-axis is gradually changing with decreasing temperature.

The temperature dependence of the AFMR spectra are shown in Fig. 3.9(a). The easy-axis mode shifts with temperature, which spin-flop resonance does not shift with temperature. The spin-flop resonance of AFMR is observed below 11 K (See Fig. 3.9(a)). The intensity of AFMR is rather small at 11 K, suggesting the AF transition is only partial, and the intensity is enhanced as temperature decreases. Furthermore, as it can be seen in the spin-flop resonance of 4.5 and 7 K, a fine double-peak structure of the spin-flop resonance, is observed below T_{MI} (See Fig. 3.9(a)). As shown in Fig. 3.9(b), this fine double-peak structure consists of two resonance with the same resonance field but different linewidth. The double peak structure is also observed in the easy-axis mode of AFMR at 4.5 K (See Fig. 3.9(a)). This double peak structure suggests that two kinds of AF spin states exist.

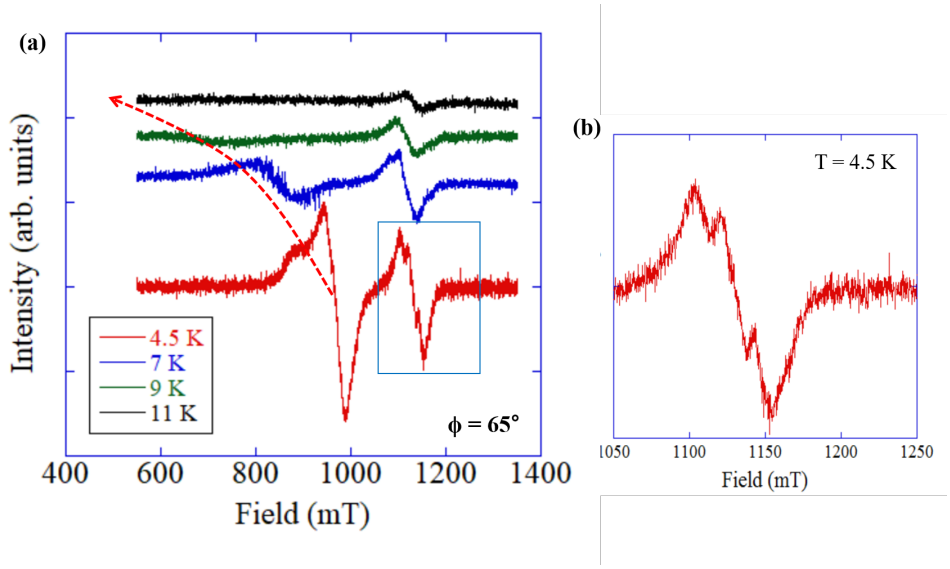

Figure 3.9: (a) Temperature dependence of ESR spectra at $\phi = 65°$. The broken arrow is an eye-guide for the resonance shift of the easy-axis mode of AFMR with temperature. (b) The focusing of the fine double peak structure at 4.5 K.

The spin-flop resonance is starting to be observed from 11 K (See Fig. 3.9(a)), and the integrated intensity gradually increases with decreasing temperature (See Fig. 3.10(a)). The integrated intensity is considered only spin-flop resonance, and this spin-flop resonance signals are asymmetrical line-shape above 7 K. This asymmetric line-shape induces difficulty to analysis for integrated intensity. Although the integrated intensity of AFMR has some error above 7 K due to asymmetric line-shape, the hysteresis of integrated intensity is observed above 7 K. Meanwhile, the EPR signals are also observed down to 6 K, which is slightly smaller than $T_{MI} = 8.3$ K. The integrated intensity of EPR at $\theta = 150°$ is shown in Fig. 3.10(b). Here, the temperature is swept up from 4.8 to 17 K, and then, swept down to the lowest temperature. In Fig. 3.10(b), a gradual decrease of the integrated intensity is observed below 14 K (down to 7 K). Moreover, the hysteresis of integrated intensity, which is probably due to the first order transition, is observed between 8 and 14 K.

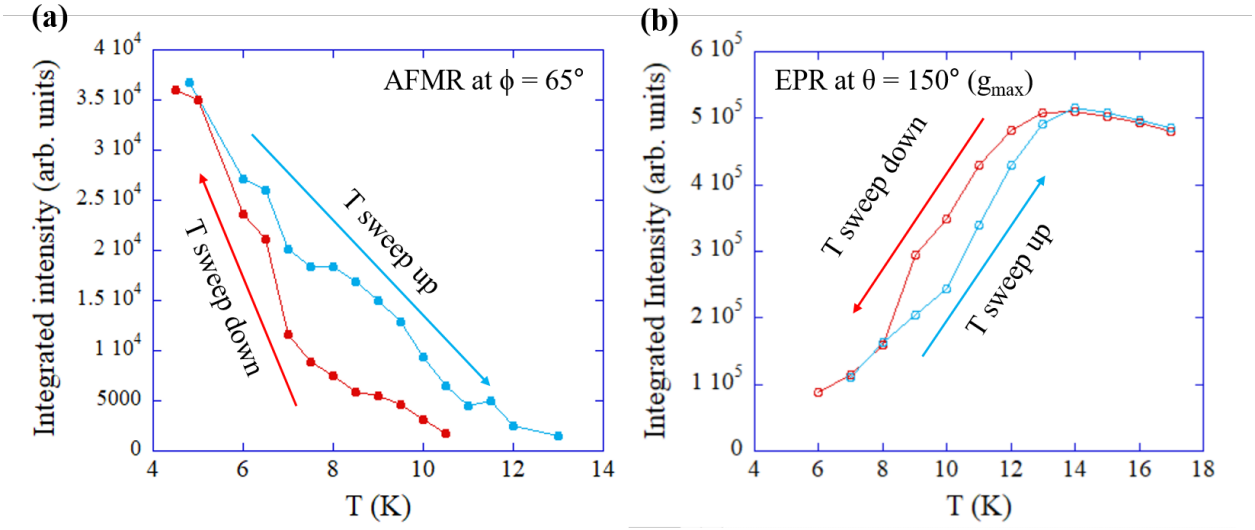

Figure 3.10: Integrated intensity of (a) AFMR at $\phi = 65°$ and (b) EPR at $\theta = 150°$ around $T_{MI} = 8.3$ K

3.1.2 Discussions

i) EPR behaviors

The π-d exchange interaction is important in this study. If there is no π-d interaction, two EPR signals from π- ($S_\pi = 1/2$) and d-electrons ($S_d = 5/2$) should be observed separately. However, if a strong exchange interaction exists, the local field is averaged out due to the fast exchange, and the EPR spectra should merge to a single line. This is known as the 'exchange narrowing' [70, 71].

The angular dependence of EPR spectra at 10 K is presented in Fig. 3.2. Only a single EPR line is observed in the a^*b^*-plane, which is consistent with previous ESR report [53]. This suggests that the π- and d-electrons are strongly coupled in λ-$(BETS)_2FeCl_4$.

The typical angular dependence of the g-value is observed at 300 K in Fig. 3.3(a). In general, microscopic information surrounding the magnetic ions can be obtained from the angular dependence of the g-value since the g-tensor reflects the symmetry of the ligand field, and its angular dependence behaves as effective g-value $g_{\rm eff}$, which is equal to $\sqrt{g_{\rm max}^2 \cos^2\theta + g_{\rm min}^2 \sin^2\theta}$ (i.e., rotational ellipsoid). Hence, typical angular dependence of the g-value has a sinusoidal curve. The maximum and the minimum g-values for 300 K are about 2.05 and 2.04, respectively (See Fig. 3.3(a)). And then, the principal-axes of the maximum and the minimum g-values correspond to the b'- and the a'-axes, respectively. The principal-axes are related to the ligand field of the $FeCl_4$ anion where $g_{\rm max}$ is along the Fe-Cl bond parallel to the b'-axis as shown in Fig 3.4. In previous studies, the ESR signal of λ-$(BETS)_2GaCl_4$ has the g-value of about $1.99 \sim 2.02$, where λ-$(BETS)_2GaCl_4$ has only π-electrons in the BETS molecule [53] (i.e. the $GaCl_4$ is non-magnetic anion). Hence, the g-factor of the BETS molecule is different with the observed g-value. These results suggest that the EPR signals come mainly from the Fe spin in λ-$(BETS)_2FeCl_4$. For λ-$(BETS)_2FeCl_4$, it is considered that the contribution of the Fe spins should be dominant in the EPR signal since the magnetic moment of Fe is larger and the π-electrons are itinerant [32].

As the mentioned above, typical angular dependence of the g-value has a sinusoidal curve at high temperature. However, two minima of the g-values are observed around $\theta = 30°$ and 90°, and starts to develop below 270 K as shown in Fig. 3.3(a). This anomalous g-value structure is called as '*canine-teeth*' structure in this thesis. The two minima of the g-values are about 1.98 and 1.99 for $\theta = 30°$ and 90° for 10 K, respectively. The direction of the minimum

g-value at $\theta = 30°$ appears to be along the projection of two cation-anion contacts in the a^*b^*-plane, #2 S$\cdots$Cl (3.836Å) and #4 S$\cdots$Cl (3.650Å) contacts, which are shown as purple and orange dotted lines in Fig. 3.4, respectively. The values in the parentheses are their interatomic distances at room temperature. The labels of the corresponding cation-anion contact are shown in Fig. 3.4, where the labels of the contacts are according to the theoretical study by Mori *et al.* [38]. In this study, Mori *et al.* estimated the exchange interactions between π- and d-electrons from the crystal structure at room temperature, and its values are 0.39 K for #2 and 0.50 K for #4, respectively. Meanwhile, the minimum g-value at $\theta = 90°$ corresponds to the projection of the cation-anion contacts #1 and #6 shown as green and blue dotted lines in Fig. 3.4, respectively. The estimated exchange couplings are 1.44 K for #1 and 14.14 K for #6, respectively. There is no g-value anomaly along the #5 contact. Note that the smallest and the second smallest π-d couplings are contacts #7 and #3, where #7 and #3 contacts are omitted for clarity in Fig. 3.4. The interesting point is that the two minimum g-values are observed along the projection of cation-anion contacts with noticeable exchange interaction.

Then, the question is 'what makes the *canine-teeth* structure in the low temperature region?'. In the transition metal coordination compounds, it is well known that the 'covalent' character of the metal-ligand bond appears in the ligands such as oxides, halides, and sulfides [70]. The 'cloud-expanding effect' can be occurred by this covalency of the metal-ligand bond. In such a case, the spin density of the central metal ion spread out to the surrounding non-magnetic ions. The expansion of the spin density from the central ion has two main effects: (i) the spin-orbit coupling decreases and (ii) the interaction increases with the surrounding atoms. The former affects the g-value to be close to the g-value of the free electron, where the g-value is equal to 2.0023, and the latter broadens the EPR linewidth since the contribution of the super hyperfine coupling increases [70]. The latter effect also contributes to the super exchange interaction if adjacent magnetic ions are present [72, 73]. The ligand field of the isolated $FeCl_4$ anion was studied theoretically and experimentally, and it was shown that the cloud-expanding effect reduces the spin-orbit coupling, and the expansion of the Fe spin density affects the g-value and the single ion anisotropy [74, 75].

In the previous studies of isolated $FeCl_4$ anion, the typical g-anisotropy with rotational ellipsoid is observed [74,75]. However, the *canine-teeth* structure observed in λ-$(BETS)_2FeCl_4$

is quite different. This difference might come from the magnetic interactions surrounding the $FeCl_4$ anion since the previous studies examined isolated $FeCl_4$ [74, 75]. Considering that the two minima of the g-values are observed along the S/Se$\cdots$Cl contacts with noticeable interactions, and its g-value is close to the free electron ($g \sim 2$) and the maximum linewidth is observed (See Fig. 3.3(b)), the *canine-teeth* structure might be a result of the cloud-expanding effect where the spin density of the central metal ion is expanded toward the p-orbital of the Cl^- which has significant exchange path with the BETS molecule. Hence, the observation of the *canine-teeth* structure with $g \sim 2$ might indicate that the π-d interaction is strong along $\theta = 30$ and 90°.

The temperature dependence of the EPR signal at $\theta = 20°$, where $\theta = 20°$ is around the minimum g-value, is presented in Fig. 3.5. The EPR linewidth gradually increases with decreasing temperature, and a steep EPR linewidth broadening is observed below 12 K. And then, the g-value gradually decreases with decreasing temperature, and sudden increases is observed below 12 K. These observations suggest that the gradual decrease of the g-value and the gradual linewidth broadening between 12 and 150 K are due to the development of the π-d correlation. In contrast, the drastic g-shift and the linewidth broadening below 12 K are due to the development of the AF spin correlation.

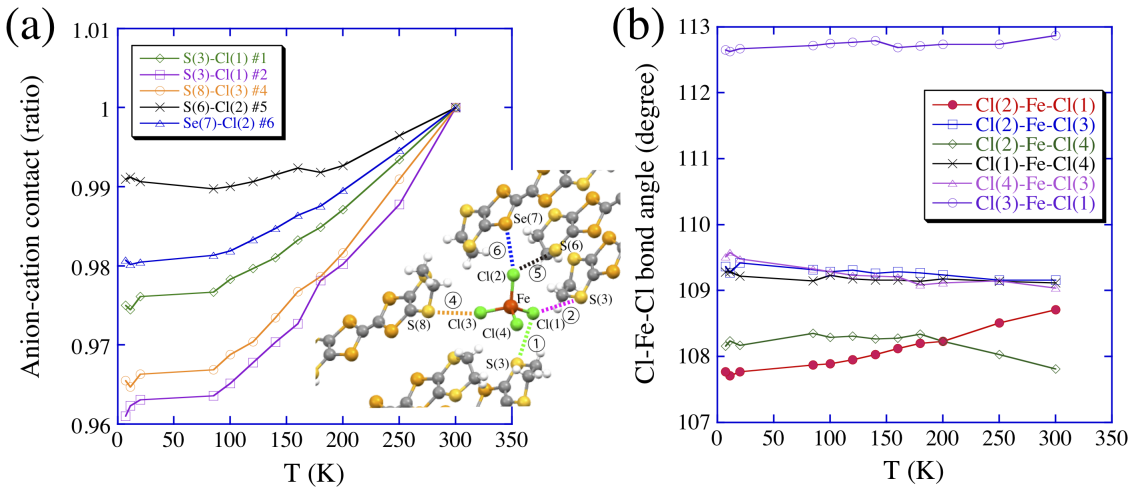

Figure 3.11: Temperature dependence of (a) the ration of the inter-atomic distance of the S/Se$\cdots$Cl compared with the distance at room temperature, and (b) the Cl-Fe-Cl bond angles in the $FeCl_4$ anion. The inset in (a) shows the S/Se$\cdots$Cl contacts surrounding the $FeCl_4$ anion

The interesting point is that the *canine-teeth* structure develops with decreasing temperature. It is expected that the decrease of the g-value suggests the spin-orbit coupling gradually reduces and the spin density of Fe^{3+} expands with decreasing temperature. If this argument is correct, there should be some increase of the π-d correlation with decreasing temperature. Hence, we verified whether the inter-atomic distance of the S/Se$\cdots$Cl contacts and the bond angles of the $FeCl_4$ anion are affected by temperature. The inter-atomic distance of typical S/Se$\cdots$Cl contacts and the Cl-Fe-Cl bonds angles as a function of temperature are shown in Fig. 3.11(a) and (b), respectively. The inset in Fig. 3.11(a) is the crystal structure around the $FeCl_4$ anion with the S/Se$\cdots$Cl contacts. The #3 and #7 contacts are not shown in Fig. 3.11 for clarity since these contacts are smallest and second smallest π-d coupling. The distance of the S/Se$\cdots$Cl contacts are normalized with the one at room temperature [38]. It is found that inter-atomic distances of #2 (purple) and #4 (orange) contacts become much shorter than other S/Se$\cdots$Cl contacts with decreasing temperature (See Fig. 3.11(a)). It suggests that the π-d couplings #2 and #4 are more enhanced with decreasing temperature. Let us remind that the #2 and #4 contacts are related with the minimum g-value observed around $\theta = 30°$. On the other hand, the #1 S$\cdots$Cl contact and #6 Se$\cdots$Cl contact are related to the minimum g-value around $\theta = 90°$, but it only shows a modest contraction of the inter-atomic distance in Fig 3.11(a). However, the bond angles of the $FeCl_4$ anion show significant changes in the Cl(2)-Fe-Cl(1) and Cl(2)-Fe-Cl(4) bond angles with temperature (See Fig. 3.11(b)). The changes of these two bond angles suggest that the Fe-Cl(2) bond is pointing toward the Se(7) of the BETS molecule with decreasing temperature. Indeed, the bond angle of Fe-Cl(2)-Se(7) changes from 160.2° at 300 K to 162.5° at 7 K, enhancing the π-d coupling #6. Therefore, the enhancement of the *canine-teeth* structure in the low temperature region might be owing to the development of the π-d coupling in λ-$(BETS)_2FeCl_4$.

Thanks to the *canine-teeth* structure of the g-value, the crystal-axes can be identified within the a^*b^*-plane (i.e., the crystal-axes can be easily found from the ESR measurement.). In Fig. 3.3(a), the b^*-axis corresponds to the maximum g-value, and the a^*-axis to one of the minimum g-value at about 120° from the b^*-axis. Hence, the b^*-axis is defined from the g-value in the a^*b^*-plane rotation, and it is possible to perform the EPR measurement in the b^*c-plane by using a triangular prism jig.

The angular dependence of the g-value and the linewidth at 10 K in the b^*c-plane is

presented in Fig. 3.6. In the b^*c-plane, an asymmetric *canine-teeth* structure of the g-value is observed at 10 K. This asymmetric *canine-teeth* structure has the first minimum and second minimum, where the g-values are 2.01 and 2.03 for $\phi = 30$ and 100°, respectively. Similarly to the results of the a^*b^*-plane rotation, a broad EPR linewidth is observed between these minima. The projections of the π-d contacts, such as #6 Se$\cdots$Cl (blue dotted line), #1 S$\cdots$Cl (green dotted line), and #2 S$\cdots$Cl (purple dotted line) contacts, correspond to the first g-value minimum at $\phi = 30°$ as shown in Fig 3.6(a). They are the same contacts that contributed to the g-value minimum in the a^*b^*-plane. On the other hand, there is no corresponding projection of the S/Se$\cdots$Cl contacts around $\phi = 100°$, where the g-value dip is about 2.03, and no g-value minimum is observed along the projection of the #4 S$\cdots$Cl (orange dotted line), where the projection is around $\phi = 150°$. In contrast to the a^*b^*-plane rotation which shows two minimum g-value with $g \sim 2$, the second minimum for $\phi = 100°$ is around $g \sim 2.03$. The difference of the effective g-value from $g = 2$ is due to the effect of the spin-obit coupling, therefore, it seems that the spin-orbit coupling is still effective at $\phi = 100°$ ($g \sim 2.03$) in comparison with $\phi = 30°$ ($g \sim 2.01$). Considering that there is no projection of the S/Se$\cdots$Cl contact and the g-value is around 2.03 at $\phi = 100°$, the second minimum at $\phi = 100°$ might not be due to the cation-anion contact but due to the minimum g-tensor reflecting the ligand field of $FeCl_4$ anion. Furthermore, the lack of g-value anomaly along $\phi = 150°$ might suggest the absence of the cloud-expanding effect for the #4 S$\cdots$Cl contact. Hence, the #2 S$\cdots$Cl contact might be the main origin of the minimum g-value at $\theta = 30°$ in the a^*b^*-plane. It is not clear why there is no sign of the cloud-expanding effect for the #4 S$\cdots$Cl contact despite that the exchange coupling is finite, 0.50 K at room temperature [38].

To summarize this section, the detailed angular and temperature dependence of ESR are performed using X-band ESR. Peculiar angular dependence of the g-value with the *canine-teeth* structure in the a^*b^*-plane is observed below 270 K. This *canine-teeth* structure develops with decreasing temperature, where the minimum g-values correspond to the projection of the cation-anion contacts with noticeable π-d interaction. The origin of the *canine-teeth* structure is ascribed to the strong π-d exchange interaction, where the expansion of the spin-density of $FeCl_4$ anion occurs along the π-d exchange paths. The crystal structure analysis by X-ray also revealed that the inter-atomic S$\cdots$Cl distances and the deformation of the $FeCl_4$ anion play an important role on the development of the *canine-teeth* structure. The change of the inter-

atomic distances and the deformation of the tetrahedral coordination in the $FeCl_4$ anions with temperature affects the π-d couplings, and its exchange interactions develop with decreasing temperature. Moreover, the maximum/minimum of the EPR linewidth is generally related with the magnetic anisotropy, and it is understandable that the AF easy-axis appears at the maximum linewidth. Therefore, the easy-axis mode of AFMR can be easily found at the linewidth maximum of EPR linewidth below T_N in the AFI phase.

——— ii) AFMR behaviors ———

Thanks to the *canine-teeth* structure of the g-value, the crystal-axes can be identified within the a^*b^*-plane. (i.e., the crystal-axes can be easily found from the ESR measurement.) It can be an alternative method to determine the crystal-axes other than the X-ray diffraction analysis. Moreover, an useful two-step method by to determine the AF easy-axis is found, which is: (i) Find the maximum g-value in the a^*b^*-plane. Namely, the direction of the maximum g-value in the a^*b^*-plane corresponds to the b^*-axis. (ii) Find the maximum linewidth in the b^*c-plane. The direction of the maximum linewidth in the b^*c-plane corresponds to the AF easy-axis.

By applying the two-step method, and applying the magnetic field along the AF easy-axis, the expected two AFMR; the easy-axis mode and the spin-flop resonance, have been observed in the AFI phase. As shown in Fig. 3.9(a), the spin-flop field is independent with the temperature. In contrast, the easy-axis mode of AFMR approaches to the EPR line (i.e. shifts to lower field) with increasing temperature because the antiferromagnetic state is changing to a paramagnetic state with the increasing temperature. The spin-flop field of λ-$(BETS)_2FeCl_4$ was reported by the magnetic torque measurement by Sasaki *et al.* [43], and the spin-flop field is observed at 1200 mT. This is consistent with the observed AFMR for B // easy-axis since the spin-flop resonance is observed at 1170 mT as shown in Fig. 3.8. Meanwhile, the intensity for both AFMR signals decreases with increasing temperature. This observation also supports that both ESR signals are AFMR.

A typical bubble-like structure of AFMR is observed as shown in Fig. 3.8, and the center of the bubble structure corresponds to the AF easy-axis. In general, AF easy-axis does not change with temperature. However, the gradual change of AF easy-axis is observed with temperature (See Fig. 3.8). As mentioned above, a strong π-d interaction exists in this

system. However, a huge change of the dielectric properties are observed within the AFI phase [55, 60, 61], where the dielectric anomalies is explained by the charge ordering on the BETS dimer [61] or the metastable π-electrons [55]. Negishi *et al.* suggested the charge polarization in BETS dimer is the orgin of the dielectric anomalies [61]. Meanwhile, Hiraki *et al.* observed the linewidth broadening from ^{77}Se-NMR measurements in the PM phase, where the linewidth broadening is also proposed to be due to the charge disproportionation on the BETS layer [52]. Hence, it is not a surprise that the charge disproportionation is enhanced around phase boundary and induces dielectric anomaly. One the other hand, Rutel *et al.* observed a huge change of the permittivity within the AFI phase, where they attributed it to the metastable state of the π-electrons. The metastable state of the π-electrons suggests that there is coexistence of localized and conducting π-electrons around the boundary of the AFI phase. Moreover, the kink structures in the resistance are observed below T_{MI} [32]. The resistance increases gradually with decreasing temperature. These reports might suggest that the π-electrons localize gradually with decreasing temperature inside the AFI phase. Hence, the change of the AF easy-axis might be due to the development of the charge disproportionation or the metastable state of the π-electrons within the AFI ground state as the temperature decreases.

The fine double peak structure at $\phi = 65^\circ$ is observed below T_{MI} as shown in Fig. 3.9(b), where the fine structure suggests two AF states. Previous study of Mössbauer spectroscopy also reported the fine structures of sextets between 3.2 and 8 K. These fine structures also suggest two different environments of the Fe. Although only one Fe site is crystallographically independent down to 10 K, the fine double peak structure of AFMR is related to the magnetic splitting observed in the Mössbauer measurements [31]. It is supposed that the two different environments of the AF Fe sites are due to the surrounding π-electrons, which are localized and conducting due to the metastable state or the charge disproportionation with the charge rich and poor. Two AF state near phase boundary will be discussed more detail in the section 3.2.2.

Furthermore, the EPR intensity start to diminish below 14 K, and the EPR signal is completely lost below 6 K in the AFI phase (See Fig. 3.10). Meanwhile, the AFMR is starting to be observed from 11 K, and the AFMR signal gradually increase with decreasing temperature as shown in Fig. 3.9. The EPR and AFMR coexist between 6 and 11 K, and

there is a cross-over from EPR to AFMR nearby the boundary of the AFI and PM phases. Hence, the mixed state between the paramagnetic and the antiferromagnetic state exist at the phase boundary. The relation between the magnetic mixed state and the π-electron state will be discuss in 3.2.2 section.

As the mentioned above, the EPR signal disappears below 6 K, which suggests that there is no paramagnetic ground state. The paramagnetic Fe model was proposed from the observation of the excess specific heat below T_N. However, paramagnetic Fe model is not suitable anymore since (i) there is no paramagnetic ground state and (ii) the excess specific heat can be explained from the slow transition from AFI to PM by decreasing temperature.

3.2 High-field ESR measurements ($B > B_{sf}$)

3.2.1 Results

Few studies reported the dielectric anomaly inside the AFI phase [55, 76]. In the previous section, the temperature dependence of ESR is measured below the spin-flop field ($B < B_{sf}$), where the change of the easy-axis and the slow transition from the antiferromagnetic to the paramagnetic states are observed near the phase boundary. It is expected that these anomalous behaviors might be related to the dielectric anomaly. In order to check whether such antiferromagnetic anomalies exist also near the phase boundary at high magnetic field, we have investigated the high-field region above the spin-flop field ($B > B_{sf}$) using high-field ESR. In Fig. 3.12, the red rectangle is the measurements area, where the measurement field range is 1.2 to 8 T.

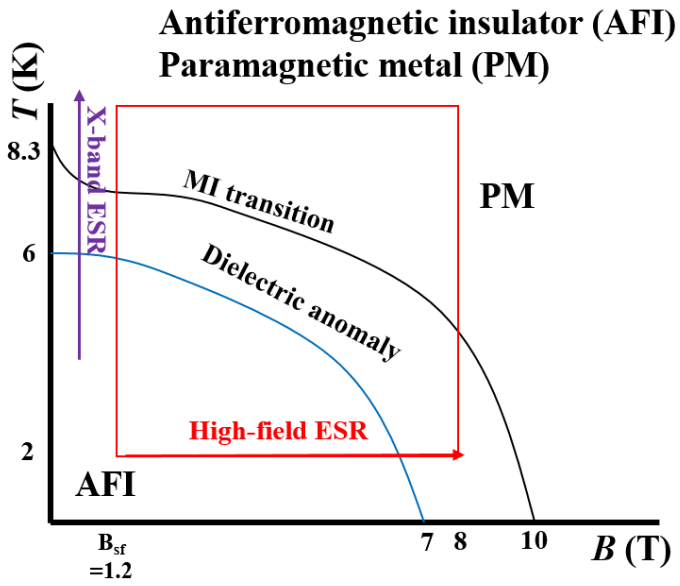

Figure 3.12: Schematic phase diagram of λ-$(BETS)_2FeCl_4$ as a function of magnetic field and temperature.

First, the sample was set so that the magnetic field is applied along the easy-axis using the two-step method described in Sec. 3.1.2. The typical ESR spectra for B // easy-axis as a function of temperature are presented in Fig. 3.13. Only one ESR signal is observed below 6 T (See Fig. 3.13(a)). The ESR signal observed in Fig. 3.13(a) is attributed to AFMR signal since the resonance field decreases with increasing temperature, which is a typical behavior

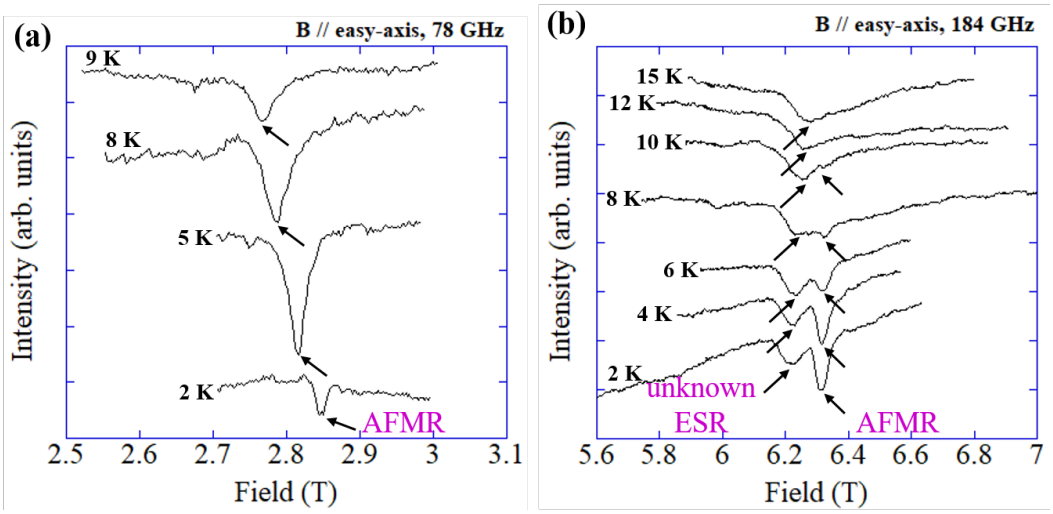

Figure 3.13: Temperature dependence of typical ESR spectra at (a) 78 GHz and (b) 184 GHz, when the magnetic field is applied parallel to the easy-axis.

of the easy-axis mode of AFMR. In contrast, the ESR signal splits above 6 T as shown in Fig. 3.13(b). At 2 K, the split ESR signals consist of a strong ESR signal and a weak ESR signal, where the strong signal appears at higher field than the weak signal. Considering the AFMR linewidth observed in Fig. 3.13(a), the strong ESR signal appearing at higher field in Fig. 3.13(b) is attributed as AFMR. In contrast, the weak signal needs more consideration. Hence, the weak ESR signal appearing at lower field in Fig. 3.13(b) is defined as 'unknown ESR' and unknown ESR will be discussed in the next section. As the temperature increases, the AFMR and the unknown ESR signals merge above 8 K as shown in Fig. 3.13(b), and the AFMR seems to vanish above 10 K. The contributions of ESR signals seem to change from AFMR to unknown ESR with increasing temperature. The change of the contribution will be also discussed later.

The frequency-field dependence of AFMR at 2 K, when the magnetic field is applied parallel to the easy-axis, is presented in Fig. 3.14. The conventional frequency-field dependence of AFMR is presented in Fig. 2.2. The result is fitted with a typical easy-axis mode of AFMR (Solid curve in Fig. 3.14). The unknown ESR appears above 6 T, and its resonance field is lower than the AFMR signal.

The frequency dependence of AFMR for B // c-axis is also measured. The results are similar with the aforementioned easy-axis results. Only a single ESR signal is observed below 6 T as shown in Fig. 3.15(a). The splitting of ESR signal is also observed above 6 T (See

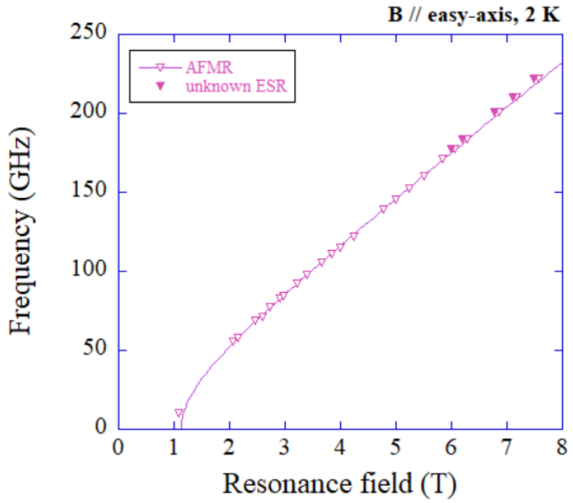

Figure 3.14: Frequency-field plots of AFMR for B // easy-axis at 2 K

Fig. 3.15(b)). The strong ESR signal also appears at higher field than the weak ESR signal, where the split ESR signals are also defined as AFMR (strong) and unknown ESR (weak), respectively. The frequency-field dependence of AFMR at 2 K, when the magnetic field is applied parallel to the c-axis, is presented in Fig. 3.16. Again, typical easy-axis mode of AFMR is observed for B // c-axis, and the split of ESR signal is observed above 6 T.

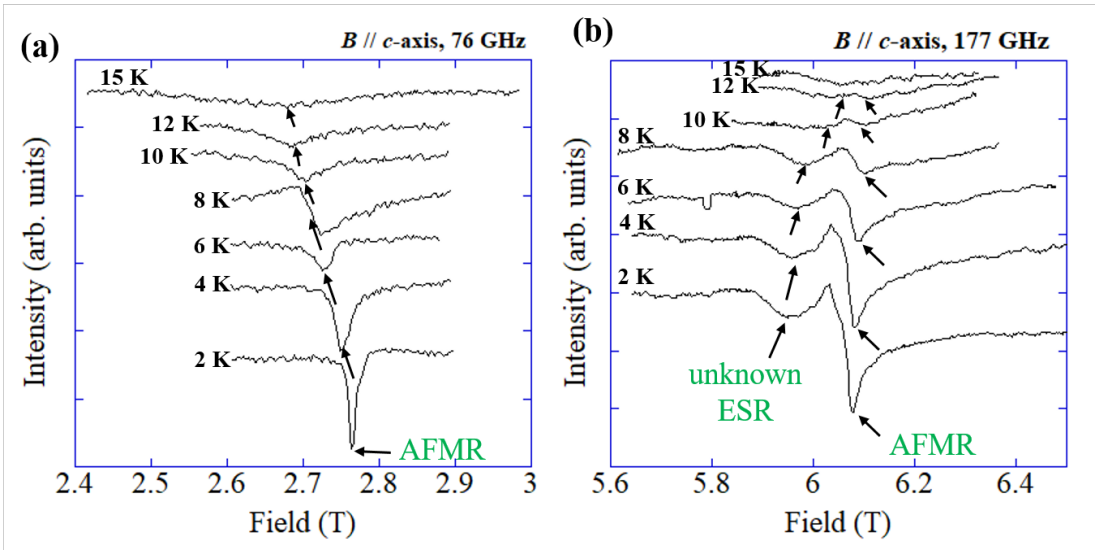

Figure 3.15: Temperature dependence of typical ESR spectra at (a) 76 GHz and (b) 177 GHz, when the magnetic field is applied parallel to the c-axis.

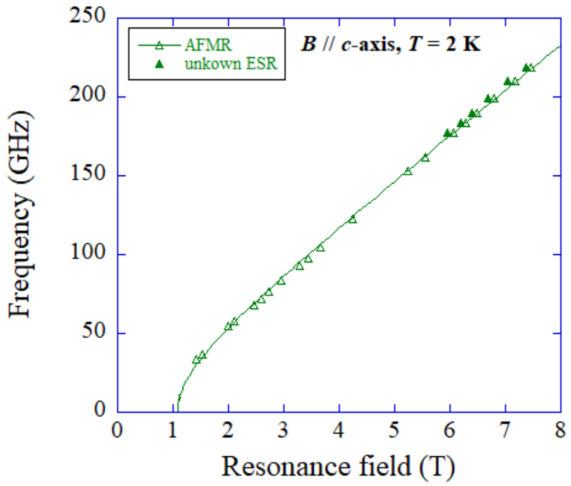

Figure 3.16: Frequency-field plots of AFMR for B // c-axis at 2 K

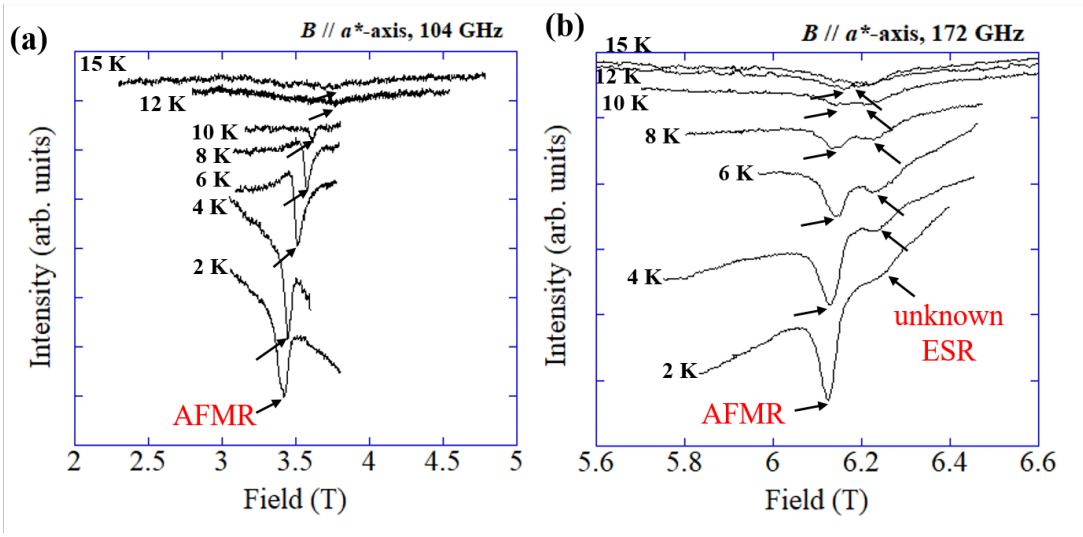

Figure 3.17: Temperature dependence of typical ESR spectra at (a) 104 GHz and (b) 172 GHz, when the magnetic field is applied parallel to the a^*-axis.

Next, the frequency dependence of AFMR for B // a^*-axis is also studied. The temperature dependence of ESR spectrum at 104 GHz is presented in Fig. 3.17(a), where only a single ESR signal is observed below 6 T. In contrast with B // easy-axis and B // c-axis results, the resonance field is shifting to higher field as a function of temperature. These behaviors are typical of the hard-axis mode of AFMR. Above 6 T, the AFMR signal splits again, which is consistent with the B // easy-axis and the B // c-axis results. A strong ESR signal and a weak ESR signal are observed, where the signals are also defined as AFMR (strong) and unknown ESR (weak). In contrast to the results for the B // easy-axis and the B // c-axis, the resonance field of the unknown ESR signal for B // a^*-axis appears at higher field than the AFMR signal (See Fig. 3.17(b)). The frequency-field dependence of AFMR for B // a^*-axis at 2 K is presented in Fig. 3.18. This result shows the typical hard-axis mode of AFMR at 2 K (The conventional frequency-field dependence of AFMR is presented in Fig. 2.2).

The AFMR for B // b^*-axis is also measured, where the b^*-axis is expected to the hard-axis. The temperature dependence of 191 GHz ESR spectrum, and the frequency-field plots of AFMR for B // b^*-axis are presented in Fig. 3.19(a) and (b), respectively. In the easy-, the c-, and the a^*-axes results, the splitting ESR signals are observed above 6 T. However, only a single ESR signal is observed for B // b^*-axis at 191 GHz, where the resonance field

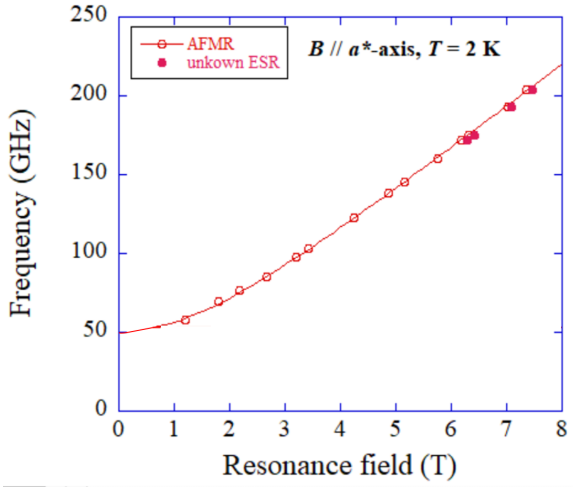

Figure 3.18: Frequency-field plots of AFMR for B // a^*-axis

is above 6 T (See Fig. 3.19(a)). As shown in Fig. 3.19(b), typical hard-axis mode of AFMR is observed for B // b^*-axis, and no splitting is observed.

Unknown ESR signals are observed along the easy-, c- and a^*-axes above 6 T. But, the different point is the position of unknown ESR signals. In Fig. 3.15(b), unknown ESRs along the easy- and c-axes appear at lower resonance field than the AFMR signal. In contrast, unknown ESR along the a^*-axis appears at higher resonance field than the AFMR signal (See Fig. 3.17(b)). Namely, the positions of unknown ESR are reversed. Meanwhile, it seems that the contributions of AFMR and unknown ESR change with the magnetic field (See Fig. 3.20). The spectra of splitting ESR signals along the c-axis for various frequencies are presented in Fig. 3.20(a). Intensity of AFMR is decreasing with increasing the magnetic field. In contrast, intensity of unknown ESR is growing with the increasing magnetic field. The results for B along the a^*-axis show similar behavior with the results for c-axis (See Fig. 3.20(b)). It suggests that the contribution changes from AFMR to unknown ESR with increasing the magnetic field.

The temperature dependence of AFMR and unknown ESR along the c- and a^*-axes are shown in Fig. 3.15(b) and 3.17(b), respectively. Both intensities of AFMR and unknown ESR are decreasing with increasing temperature. The intensity of AFMR is more rapidly decreasing than the intensity of unknown ESR with increasing temperature. Hence, the expectation is that the contribution of intensity changes from AFMR to unknown ESR with increasing temperature.

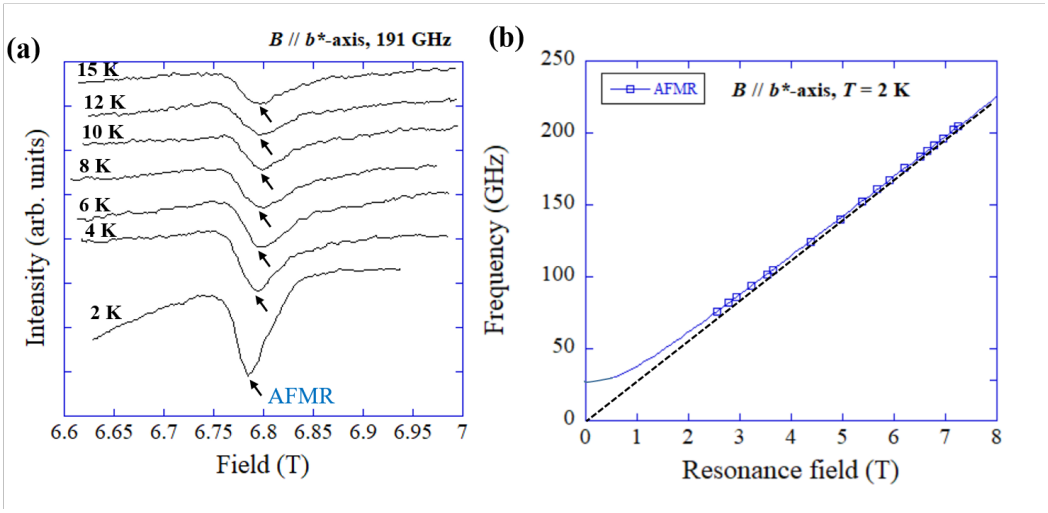

Figure 3.19: (a) Temperature dependence of typical ESR spectra at 191 GHz, when the magnetic field is applied parallel to the b^*-axis. (b) Frequency-field plots of AFMR for B // b^*-axis .

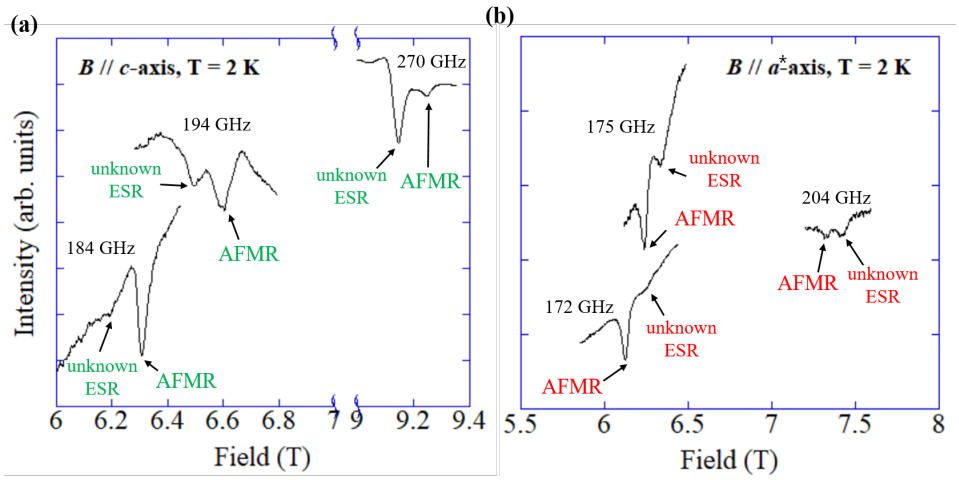

Figure 3.20: Spectra along (a) the c-axis and (b) the a^*-axis at several frequencies.

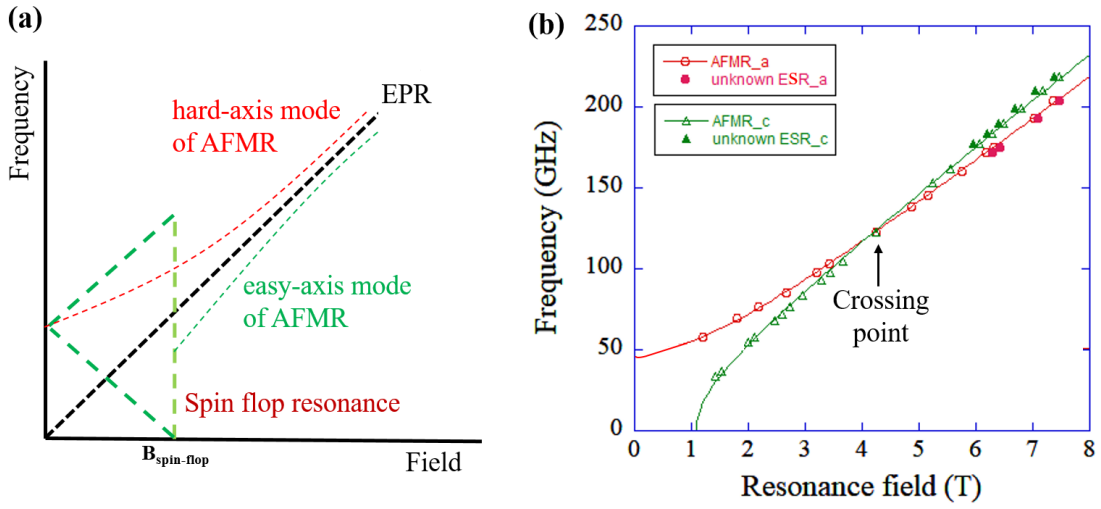

Figure 3.21: (a) Conventional field-frequency AFMR. (b) The frequency dependence of the resonance field along the c- and the a-axes.

In conventional AFMR theory, the easy-axis mode and the hard-axis mode approach to the EPR line with increasing magnetic field (See conventional frequency-field plots in Fig. 3.21(a)). Both AFMR modes should not cross with increasing the magnetic field. However, the crossing of the AFMR modes is observed at 4 T, when the results of B // a^*-axis and B // c-axis are presented together (See Fig. 3.21(b)). Below 4 T, the easy-axis mode of AFMR is observed along the c-axis and the hard-axis mode of AFMR is observed along the a^*-axis. Here, the result of b^*-axis is omitted for clarity in Fig. 3.21(b). Above 4 T, the resonance field for the c-axis becomes lower than the resonance field for the a^*-axis. The details of such crossing behavior of AFMR and the origin of unknown ESR will be discussed in Sec. 3.2.2.

3.2.2 Discussions

First, the question is 'what is the unknown ESR?' The unknown ESR is strarting to be observed above 6 T, and the contribution of unknown ESR is increasing with increasing the magnetic field. From the magnetotransport measurements, the PM state is recovered by the strong magnetic field above 10.5 T. Hence, it is expected that the unknown ESR is related to the PM state. The previous high-field ESR measurements have been performed in high-field region between 11 and 22 T [32], where this magnetic field range is completely in the paramagnetic state. Hence, the ESR signals between 11 and 22 T can be considered as EPR signals. In Fig. 3.22(a), the orange line is the EPR line from the previous ESR measurements [32]. This EPR line has the offset at zero-field due to the uniaxial anisotropy of $FeCl_4$ anion, where the offset is about $\sim$ 11.3 GHz (0.54 K). From the analysis, the unknown ESR is on the EPR line as shown in Fig. 3.22(b). This observation concludes that unknown ESR is EPR.

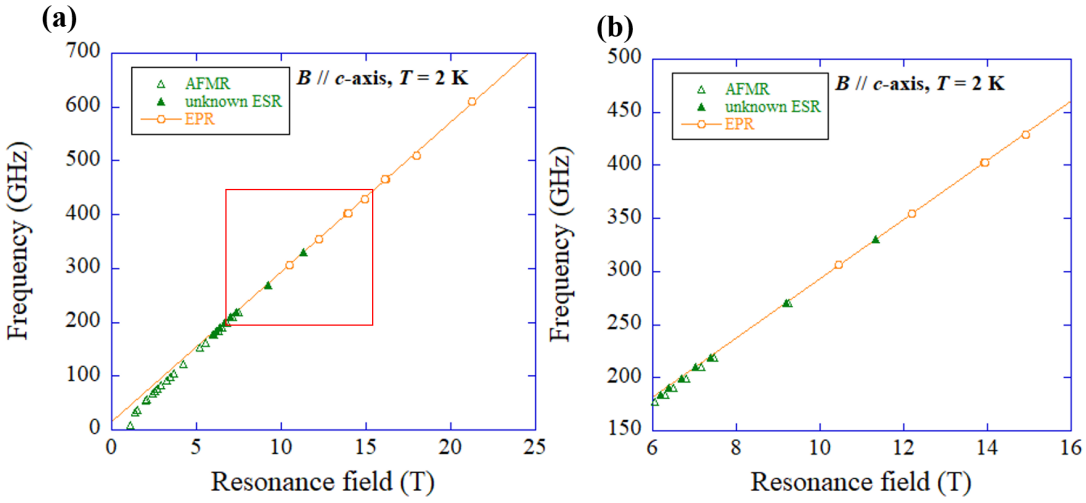

Figure 3.22: (a) Frequency-resonance field dependence of ESR along the c-axis, the orange line is the EPR line from the previous ESR measurements [32]. (b) The zoomed overview of the red area in Fig. 3.22(a).

The EPR signals are observed above 6 T for B // the easy-, the c-, and a^*-axes. However, no ESR splitting was observed for B // b^*-axis. As mentioned above, the EPR line along the c-axis has the offset at zero-field due to the uniaxial anisotropy of $FeCl_4$ anion [32]. Hence,

the offset should be angular dependent. In Figs. 3.23(a) and (b), the green dotted line along the c-axis has the offset 11.3 GHz, and the red dotted line along the a^*-axis has the offset -14.4 GHz. If there is also EPR for the b^*-axis, it is possible that frequency offset due to uniaxial anisotropy is nearly zero, and the AFMR and EPR are overlapped above 6 T as schematically shown in Fig. 3.24.

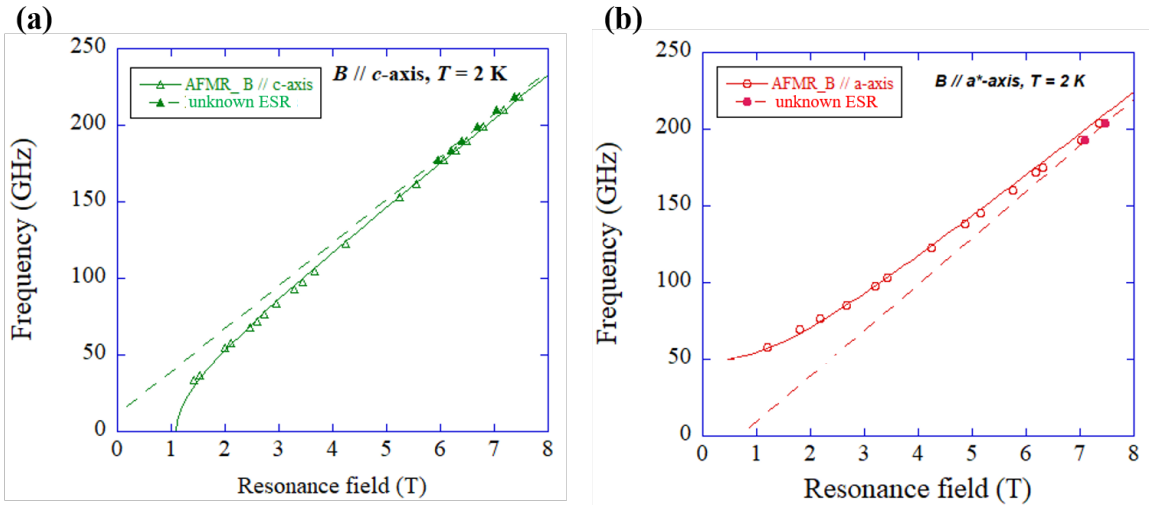

Figure 3.23: Frequency-field dependence of (a) the c-axis and (b) the a^*-axis.

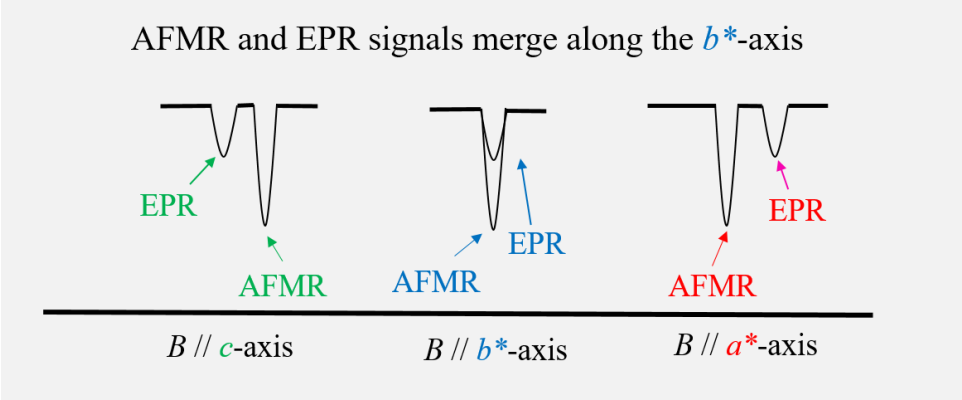

Figure 3.24: Schematic figure for the splitting AFMR signals along c-, b^*, and a^*-axes.

For a conventional frequency-field diagram of AFMR, the easy-axis mode of AFMR appears at higher field than the hard-axis mode of AFMR for a constant frequency (See Fig. 3.21(a)). And, the easy-axis mode and the hard-axis mode of AFMR approach to the EPR line with increasing the magnetic field (See Fig. 3.21(a)). The two AFMR modes never cross each other with increasing magnetic field. Below 4 T, the easy-axis mode of AFMR is observed

along the c-axis. In contrast, the hard-axis mode of AFMR is observed along the a^* and b^*-axes, where the results of b^*-axis are omitted for clarity in Fig. 3.21(b). Above 4 T, the resonance field for B // c-axis (green) appears at lower field than B // a-axis (red) (i.e., the AFMR modes are crossing at 4 T). In general, the AFMR mode changes from the easy-axis mode to the hard-axis mode when the magnetic field is tilted from the easy-axis. Hence, this crossing might suggest the change of AFMR mode with the magnetic field, where the change of AFMR mode indicates the change of AF easy-axis with the magnetic field.

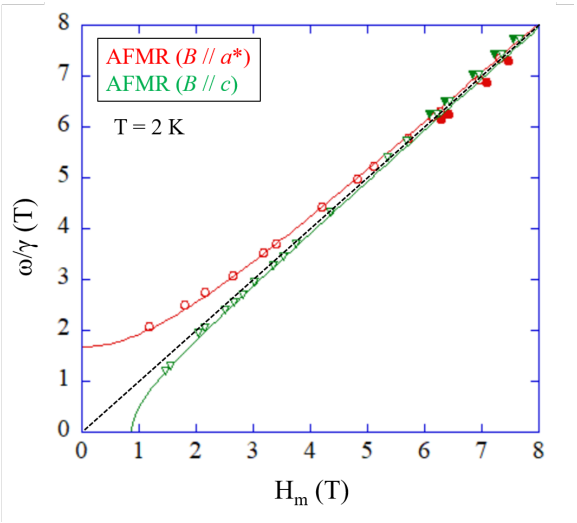

Figure 3.25: The ω/γ-modified field H_m plot for B // c (green) and a^* (red)

For a more detail analysis, the angular dependence of the g-value obtained from X-band ESR measurements is considered. The ω/γ-H_m plot for B // c- and a^*-axes is presented in Fig. 3.25. Such plot is very useful since EPR line can be described as $\omega/\gamma = H_m$, which is shown as a dotted line in Fig. 3.23. The modified field $H_m = (g/2)H_0$ and $\omega/\gamma = (h\nu)/(\mu_B g)$ can be defined by the g-values for several axes, where H_0 is the resonance field, ω is the precession frequency, γ is the gyromagnetic ratio, h is the Planck's constant, ν is the frequency, and μ_B is the Bohr magneton. If the EPR g-value for 10 K is taken into account for each axis, the AFMR modes approach to the EPR line as a function of the modified magnetic field. (See Fig. 3.25). Hence, if the g-values are considered correctly, the AFMR modes do not cross at 4 T.

As mentioned above, the EPR signal is starting to be observed above 6 T. Interestingly, a huge change of the high frequency response, both $\Delta f/f$ and amplitude in Fig. 3.26(b), is

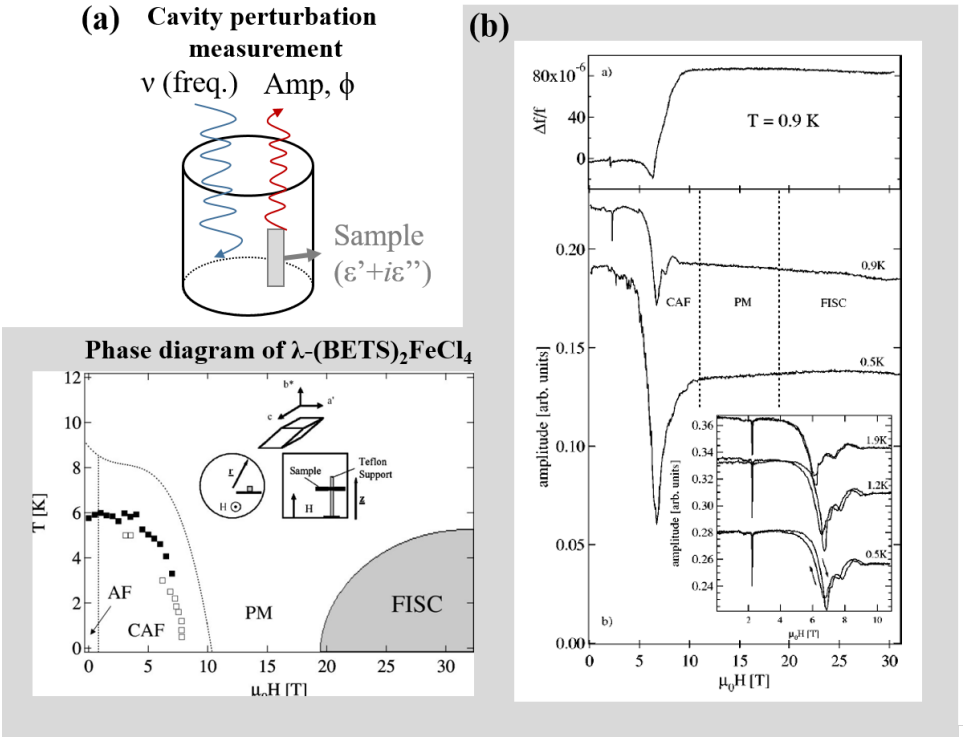

Figure 3.26: (a) Schematic figure for cavity perturbation measurement. (b) Phase diagram with sample configuration and measurement results [55]

also observed above 6 T [55]. Although it is an insulator in the AFI phase, the electronic state of the π-electrons seem to largely change above 6 T. Hence, the magnetic d-electrons might be affected by this drastic change of the π-electrons via the strong π-d interaction. Hence, it is expected that the coexistence of AFMR and EPR from 6 to 10.5 T is related with the observation of dielectric anomalies. Moreover, the contribution of intensity changes from AFMR to EPR with increasing the magnetic field. Intensity of AFMR is decreasing with increasing magnetic field. In contrast, intensity of EPR is growing with increasing magnetic field. This behavior suggests the slow transition/cross-over between the antiferromagnetic and the paramagnetic state occur nearby the phase boundary.

It is supposed that the gradual transition from the AFI to the PM phase with increasing the magnetic field is related to the dielectric anomaly. Then, the question remains, what is the origin of the dielectric anomalies? There are two candidates for the dielectric anomalies in the AFI phase. The charge order or charge disproportionation scenario proposed by Negishi *et al.* [52, 60, 61], and the metastable state scenario proposed by Rutel *et al.* [55]. Moreover,

the charge disproportionation of the conducting layer was reported by Hiraki *et al* [52]. They suggest that the charges are not ordered in the PM phase as rich or poor sites but there is a continuous distribution of charge in the conducting layer.

The C=C bond length in BETS molecule is generally increased when the site charge increases [77]. If the charge disproportionation exists in the BETS molecule, the C=C bond length should change. Hence, the C=C bond length in BETS molecule is investigated by X-ray. The results are shown in Fig. 3.27. The C=C bond length of B-type BETS molecule decreases with temperature. In contrast, the C=C bond length of A-type BETS molecule increases with temperature. Hence, the expectation is that charge disproportionation might exist in λ-$(BETS)_2FeCl_4$. And, the charge of the A-type BETS molecule is richer than the B-type BETS molecule.

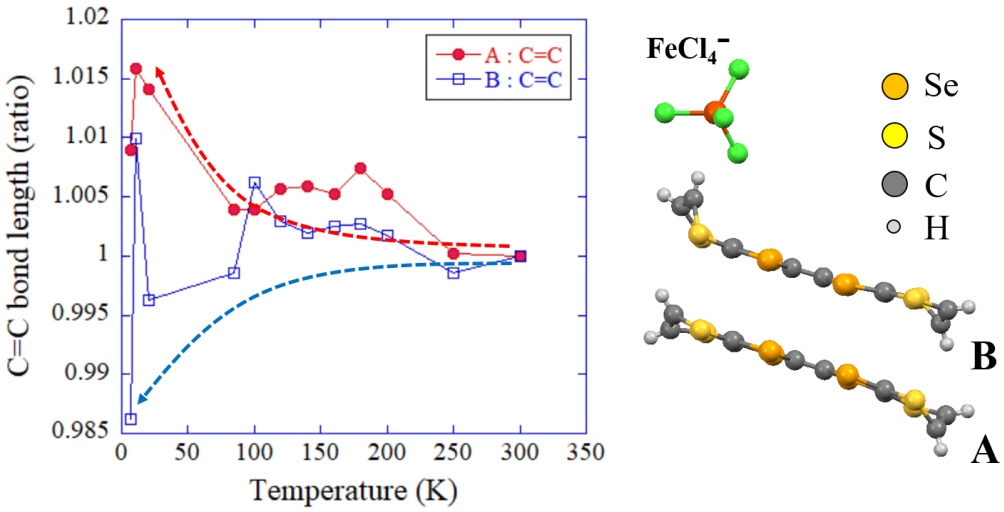

Figure 3.27: Temperature dependence of normalized C=C bond length, where the BETS molecules are labeled as A-type and B-type. The one of outer-ring in B-type is bent.

Moreover, the distance between BETS molecules also supports the charge disproportionation scenario. Fig. 3.28 shows the temperature dependence of distance between BETS molecules. B-B' distance shrinks more than the other distances between the BETS molecules, such as the A-A' and the A-B distances. This behavior might be due to Coulomb repulsion between BETS molecules. The BETS molecules have a positive charge, and, the B-type BETS molecule has a smaller charge than the A-type BETS molecule. Hence, the Coulomb repulsion between B-B' is weaker than A-B and A-B'. Therefore, temperature dependence of

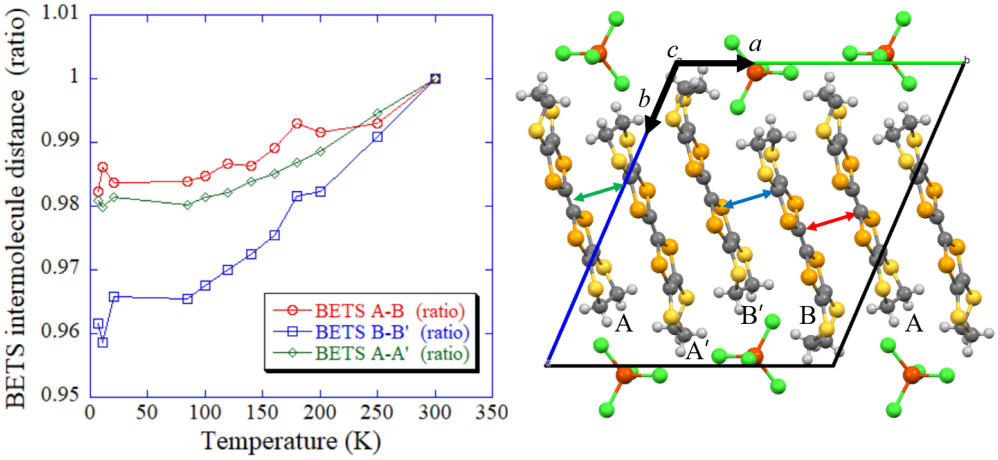

Figure 3.28: Temperature dependence of normalized distance between BETS molecules.

the distance between BETS molecules support the A- and B-type BETS molecules having different charges. The charge disproportionation seem to exist in this system from X-band ESR measurements. Although the metastable π-electrons scenario can explain the relation between the dielectric anomaly and our results of ESR measurements, such scenario can not explain our X-ray measurement results. Hence, the origin of the dielectric anomaly near the phase boundary is probably due to the charge disproportionation.

Chapter 4

Conclusion

Although the FISC phase of λ-$(BETS)_2FeCl_4$ is well-understood by Jaccarino-Peter compensation mechanism, the AFI ground state of λ-$(BETS)_2FeCl_4$ is still not well-understood. The phase boundary of the AFI ground state was previously obtained by the MI transition. However, the dielectric anomalies due to the metastable state of the π-electrons or the charge disproportionation were previously reported within the AFI phase [55,60,61]. Hence, we have investigated the magnetic properties of the AFI phase in detail using the ESR spectroscopy.

The AF easy-axis of λ-$(BETS)_2FeCl_4$ is known to be tilted 30° from the c-axis to the b^*-axis [43]. Although the c-axis is related to the needle-axis, the a^*- and b^*-axes are difficult to define due to the needle-shaped single crystal. It makes a problem when we want to investigate the antiferromagnetic properties since the AF easy-axis is important to study its magnetic properties. Hence, this study first aimed on how to find the AF easy-axis by ESR. When the X-band ESR measurements are performed, peculiar angular dependence of the g-value is observed in the a^*b^*-rotation. Two minima of the g-values are observed at θ = 30° and 90° in contrast to the typical angular dependence of the g-value which behaves as a sinusoidal curve. The angle of θ = 30° and 90°, where the two minima are observed, correspond to the projection of typical cation-anion contacts with noticeable π-d interaction. Hence, the origin of the two minima is due to the strong π-d interaction. Thanks to this characteristic angular dependence of the g-value, the crystal-axes can be easily found from the X-band ESR measurements. The maximum g-value at 10 K corresponds to the b^*-axis in the a^*b^*-plane, and the other crystal-axes can be also determined from the principal-axes

of the g-value (See Fig. 3.3). Furthermore, it is found from this study that the AF easy-axis can be determined by a simple two-step method, which is presented in the discussion part of X-band ESR measurements section. The two-step is (i) find the maximum g-value in the a^*b^*-plane, which is the b^*-axis and (ii) find the linewidth maximum in the b^*c-plane, which is the AF easy-axis of λ-$(BETS)_2FeCl_4$.

Although the AF easy-axis is usually not affected by temperature, the AF easy-axis of λ-$(BETS)_2FeCl_4$ seems to change with temperature. As shown in Fig. 3.8, the AF easy-axis is tilted few degrees in the AFI phase. Two reasons are expected for explaining such phenomenon, (i) the molecular deformation of $FeCl_4$ anion, or (ii) the effect of the π-electrons via the π-d interaction. For instance, the molecular structure might change with the change of the Cl-Fe-Cl bond-angle, and such change might affect the magnetic anisotropy and the AF easy-axis as well. The enhancement of the charge disproportionation on the BETS molecule might also affect the AF easy-axis since strong π-d interaction exists in the system. The previous dielectric measurements suggest the charge disproportionation or the metastable state of the π-electrons near the AFI phase boundary. The question is then what is the best scenario for the ground state of λ-$(BETS)_2FeCl_4$? From the X-ray measurement results, the C=C bond length change with temperature (See Fig. 3.27). The charge disproportionation can explain such change of the C=C bond length with temperature. In contrast, the metastable model,which suggests the coexistence of conducting and localized π-electrons, is difficult to explain the change of the C=C bond length. Hence, the electronic state of the π-electrons is a key for understanding the ground state of this system, and the X-ray results seem to support the charge disproportionation scenario, which affects the AF easy-axis.

Meanwhile, the double peak structure of AFMR is observed below T_{MI} (See Fig. 3.9), which suggests two different environments of Fe spin. Two AF states of Fe spins around the phase boundary are consistent with the previous Mössbauer measurements [48]. When the Fe spin interacts with the other Fe spins, the Fe spins connect not only by the shortest Cl $\cdots$ Cl contact but also the π-d network. And, the π-d network affects the charge disproportionation, which induces two different π-d network by the charge rich and poor sites. Hence, the expectation is that two different environments consist of the charge disproportionation on BETS layer, such as the charge rich and poor on the BETS layer.

On the other hand, the intensity of AFMR increases gradually with increasing temperature.

And, the intensity of EPR start to diminish below 14 K, and the EPR signal is completely lost below 6 K in the AFI phase (See Fig. 3.10). These observations suggest a slow transition (cross-over) between antiferromagnetic state and paramagnetic state in the wide temperature range (6 to 14 K). The lack of the EPR signal below 6 K suggests that there is no paramagnetic ground state in the AFI phase. Only a slow transition from the PM to the AFI phase is observed from the ESR measurements. Hence, the paramagnetic Fe model is not consistent with our results. A slow transition between antiferromagnetic and paramagnetic states indicates the mixed state of antiferromagnetic and paramagnetic in a wide temperature range near the phase boundary. When the magnetic field is increased, the splitting AFMR signals are observed above 6 T, which consists of AFMR and EPR. It suggests that there are mixed states of antiferromagnetic and paramagnetic states above 6 T. Hence, the mixed state is also observed in a wide magnetic field range ($6 \sim 10.5$ T near the phase boundary). Moreover, these splitting signals show the change of the contribution between AFMR and EPR with the magnetic field and temperature. This change of the contribution suggests a slow transition (or cross-over) between antiferromagnetic and paramagnetic states with the magnetic field and temperature. Meanwhile, the magnetocaloric effect shows the increased of the entropy above 6 T [47]. Although the interpretation of the results is different with us, this increased of the entropy supports that a mixed state appears above 6 T. Furthermore, the dielectric anomalies were also observed above 6 T [55], where the change of the high-frequency response might be due to the change of the charge disproportionation with the magnetic field. The Fe spins are polarized by the strong external field, where the AF internal field decreases with the magnetic field. And, the charge disproportionation becomes week with the magnetic field. Hence, the π-d network is destroyed by the strong magnetic field, which makes the magnetic mixed state above 6 T. Moreover, the Schottky anomaly below T_{MI} can be understood by the enhancement of the charge disproportionation. The charge disproportionation enhances gradually with decreasing temperature, which makes large excess specific heat blow T_{MI} [45]. The splitting ESR signals are therefore related to the change of the charge disproportionation with the magnetic field.

To end this chapter, the actual mechanism of the MI transition is proposed based from this study. Although the mechanism of the MI transition is still needed to be studied for clearer explanation, it is supposed from this study that the AF ordering of Fe spins triggers the MI transition, because the AFMR signals are observed above T_{MI}. If we look carefully the crystal structure, there is one short contact (3.557 Å at room temperature) between Cl $\cdots$ Cl. Although the other Cl $\cdots$ Cl contacts are faraway (longer than 6 Å), J_{dd} can not be neglected due to this shortest Cl $\cdots$ Cl contact because the ionic radius of Cl^- is 1.81 Å. Hence, this shortest-path can induce the superexchange interaction between Fe spins. It is expected that the AF long-range order of the Fe spins is induced by the RKKY-like ($J_{\pi d}$) and superexchange (J_{dd}) interactions, which supports that the MI transition is triggered by the AF ordering of the Fe spins. Although the π-electrons are completely metallic, the charge disproportionation exists in the PM phase [51, 57, 60, 61]. The ferroelectric properties was observed below 70 K (See Fig. 1.25) [61], which might be due to the charge disproportionation between the BETS dimers as described in Fig. 4.1(a). Although it is difficult to define how the BETS molecules are polarized, the BETS dimers might consist of the charge rich BETS dimer and the charge poor BETS dimer above T_{MI}. Such charge disproportionation between the BETS dimers should induce the ferroelectric properties, but the degree of disproportionation is low enough so that the π-electrons still conduct. Meanwhile, zero dielectric constant was observed below T_{MI} (See Fig. 1.25 [61]), which might be due to the antiferroelectric properties. Above T_{MI}, the BETS layer consists of the charge rich dimer (A-A′) and the charge poor dimer (B-B′). Meanwhile, the superexchange (J_{dd}) interactions and RKKY interaction induce the AF ordering of Fe spins. And, the internal field from the AF Fe spins affects the π-electron state due to the strong π-d interaction. Then, different type of charge disproportionation might occur in the BETS dimer at T_{MI} as shown in Fig. 4.1(b). Such intradimer charge disproportionation with charge rich A-type BETS and charge poor B-type BETS molecules induces the antiferroelectric properties and has lower conductivity. Hence, the MI transition occurs below T_{MI}. As temperature is decreased, the AF internal field of the Fe spins develops, which induces larger charge disproportionation, and the resistance gradually increases. The ground state at the lowest temperature is therefore expected to be completely antiferromagnetic and insulating. As the magnetic field is increased, the Fe spins are polarized by strong external field. And, this polarization decreases the AF internal field,

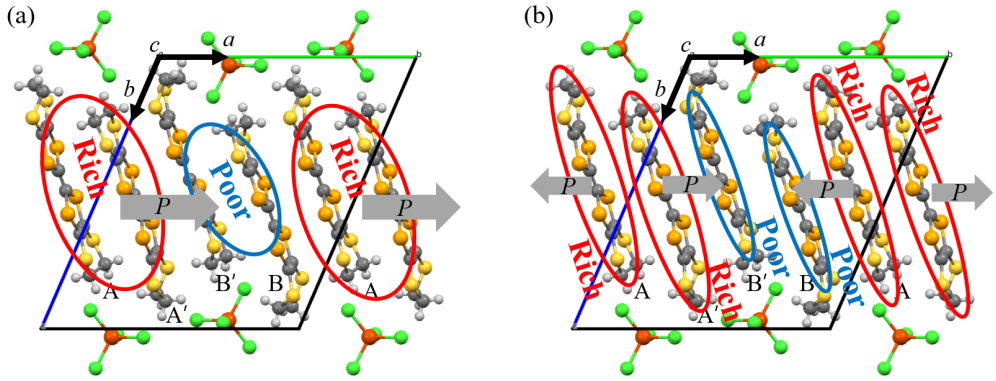

Figure 4.1: Schematic picture of (a) the charge disproportionation between the BETS dimers and (b) the intradimer charge disproportionation.

which also decreases the degree of the intradimer charge disproportionation. Above 10.5 T, the Fe spins are fully polarized, and the charge disproportionation type changes from the intradimer to the interdimer. Hence, the metallic state recovers above 10.5 T. In conclusion, the charge degree of freedom on the BETS layer and its π-d network play a very important role on the AFI ground state of λ-$(BETS)_2FeCl_4$.

Acknowledgements

I would like to thank Professor Yugo Oshima for his expert advice and extraordinary support in this thesis. Besides that, although I had some personal problems when I came to Japan, he understood my problems and supported me. It made that I can focus on my study. He gave to me the chance for a new life, hence, I can never forget his advice and support for me.

I would like to thank my laboratory members for their supports, Professor Reizo Kato, Professor Shigeki Fujiyama, Dr. Hengbo Cui, Dr. Yohitaka Kawasugi, Dr. Takaaki Minamidate, Dr. Masashi Uebe, and Yukiko Kurakata-san. Thanks to my laboratory members, I can finish my Ph.D. course. Especially, Fujiyama-sensei, Cui-sensei, and Minamidate-senpai supported for my thesis. And, Kurakata-san supported for my family. Every member has given me the good memories in my life.

Finally, I would like to thank my parents, a brother, and lovely my son and a wife. In particular, I would like to express my gratitude to Eunji and Shinyul.

References

[1] J. Ferraris, D. O. Cowan, J. V. Walatka, and J. H. Perlstein. *J. Am. Chem. Soc.*, **95**:948, (1973).

[2] L. B. Coleman, M. J. Cohen, D. J. Sandman, F. G. Yamagishi, A. F. Garito, and A. J. Heeger. *Solid State Commun.*, **12**:1125, (1973).

[3] D. S. Acker, R. J. Harder, W. R. Hertler, W. Mahler, L. R. Melby, R. E. Benson, and W. E. Mochel. *J. Am. Chem. Soc.*, **82**:6408, (1960).

[4] D. L. Coffen and P. E. Garret. *Tetrahedron. Lett.*, **10**:2043, (1969).

[5] D. L. Coffen. *Tetrahedron. Lett.*, **30**:2633, (1970).

[6] D. L. Coffen, J. Q. Chambers, D. R. Williams, P. E. Garret, and N. D. Canfield. *J. Am. Chem. Soc.*, **93**:2258, (1971).

[7] F. Wudl, G. M. Smith, and E. J. Hufnagel. *J. Chem. Soc., Chem. Commun.*, page 1453, (1970).

[8] F. Wudl, D. Wobschal, and E. J. Hufnagel. *J. Am. Chem. Soc.*, **64**:670, (1972).

[9] J. R. Kirtley and J. Mannhart. *Nature materials*, **7**:520, (2008).

[10] H. Jiang, X. Yang, Z. Cui, Y. Liu, H. Li, W. Hu, and C. Kloc. *Cryst. Eng. Comm.*, **16**:5968, (2014).

[11] T. J. Kistenmacher, T. E. Phillips, and D. O. Cowan. *Acta Cryst.*, **B30**:763, (1974).

[12] R. E. Peierls. *Quantum Theory of Solids*. (Oxford Univ., New York, London), (1955).

[13] K. Bechgaard, C. S. Jacobsen, K. Mortensen, H. J. Pedersen, and N. Thorup. *Solid State Comm.*, **33**:1119, (1979).

[14] D. Jérome, A. Mazaud, and M. Ribault. *J. Phys. Lett*, **41**:L95, (1980).

[15] G. Saito, T. Enoki, K. Toriumi, and H. Inokuchi. *Solid State Comm.*, **42**:557, (1982).

[16] R. Kato, H. Kobayashi, A. Kobayashi, S. Moriyama, Y. Nishino, K. Kajita, and W. Sasaki. *Chem. Lett.*, **1986**:507, (1986).

[17] H. Kobayashi, R. Kato, A. Kobayashi, S. Moriyama, Y. Nishino, K. Kajita, and W. Sasaki. *Chem. Lett.*, **1987**:459, (1987).

[18] A. M. Kini, U. Geiser, H. H. Wang, K. D. Carlson, J. M. Williams, W. K. Kwor, K. D. Vandervoort, J. E. Thompson, D. L. Supka, D. Jung, and M. H. Whangbo. *Inorg. Chem.*, **29**:2555, (1990).

[19] J. M. Williams, A. M. Kini, H. H. Wang, K. D. Carlson, U. Geiser, L. K. Montgomery, G. J. Pyrka, D. M. Watkins, J. M. Kommers, S. J. Boryschuk, A. V. S. Crouch, W. K. Kwor, J. E. Schirber, D. L. Overmyer, D. Jung, and M. H. Whangbo. *Inorg. Chem.*, **29**:3272, (1990).

[20] H. H. Wang, K. D. Carlson, U. Geiser, A. M. Kini, A. J. Schultz, J. M. Williams, L. K. Montgomery, W. K. Kwok, U. Welp, K. G. Vandervoort, S. J. Boryshuk, A. V. S. Crouch, J. M. Kommers, D. M. Watkins, J. E. Schirber, D. L. Overmyer, D. Jung, J. J. Novoa, and M. H. Whangbo. *Synth, Met,*, **41-43**:1983, (1991).

[21] M. Dressel and N. Dirchko. *Chem. Rev.*, **104**:5689, (2004).

[22] H. Kobayashi, A. Kobayashi, and P. Cassoux. *Chem. Soc. Rev.*, **29**:325, (2000).

[23] K. Kikuchi, M. Kikuchi, T. Namiki, G. Saito, K. Ikemoto, K. Murata, T. Ishiguro, and K.Kobayashi. *Chem. Lett.*, **1987**:931, (1987).

[24] R. Kato, S. Aonuma, Y. Oshima, H. Sawa, M. Tamura, M. Kinoshita, K. Oshima, A. Kobayashi, K. Bun, and H. Kobayashi. *Synth. Met.*, **61**:199, (1993).

[25] K. Kikuchi, T. Namii, I. Ikemoto, and K. Kobayashi. *J. Chem. Soc., Chem. Comm.*, **1986**:1472, (1986).

[26] K. Enomoto, J. Yamaura, A. Miyazaki, and T. Enoki. *Bull. Chem. Soc. Jpn.*, **76**:945, (2003).

[27] M. Y. Ogawa, J. Martinsen, S. M. Palmer, J. L. Stanton, J. Tanaka, R. L. Greene, B. M. Hoffman, and J. A. Ibers. *J. Am. Chem. Soc.*, **109**:1115, (1987).

[28] N. Hanasaki, M. Matsuda, H. Tajima, E. Ohmichi, T. Osada, T. Naito, and T. Inabe. *J. Phys. Soc. Jpn.*, **75**:033703, (2006).

[29] T. Inabe and H. Tajima. *Chem. Rev.*, **104**:5503, (2004).

[30] M. Matsuda, T. Naito, T. Inabe, N. Hanasaki, H. Tajima, T. Otsuka, K. Awaga, B. Narymbetov, and H. Kobayashi. *J. Mater. Chem.*, **10**:631, (2000).

[31] H. Kobayashi, H. Tomita, T. Naito, A. Kobayashi, F. Sakai, T. Watanabe, and P. Cassoux. *J. Am. Chem. Soc.*, **118**:368, (1996).

[32] Y. Oshima, H. B. Cui, and R. Kato. *Magnetochemistry*, **3**:10, (2017).

[33] S. Uji and J. S. Brooks. *J. Phys. Soc. Jpn.*, **75**:051014, (2001).

[34] S. Uji, H. Shinagawa, T. Yakabe, Y. Terai, M. Tokumoto, A. Kobayashi, H. Tanaka, and H. Kobayashi. *Nature*, **410**:908, (2006).

[35] V. Jaccarino and M. Peter. *Phys. Rev. Lett.*, **9**:290, (1962).

[36] S. Fujiyama, M. Takigawa, J. Kikuchi, H. B. Cui, H. Fujiwara, and H. Kobayashi. *Phys. Rev. Lett.*, **96**:217001, (2006).

[37] K. Hiraki, H. Mayaffre, M. Horvatic, C. Berthier, S. Uji, T. Yamaguchi, H. Tanaka, A. Kobayashi, H. Kobayashi, and T. Takahashi. *J. Phys. Soc. Jpn.*, **76**:124708, (2007).

[38] T. Mori and M. Katsuhara. *J. Phys. Soc. Jpn.*, **71**:826, (2002).

[39] H. Kobayashi, H. Tomita, T. Naito, A. Kobayashi, F. Sakai, T. Watanabe, and P. Cassoux. *J. Am. Chem. Soc.*, **118**:368, (1996).

[40] M. Tokumoto, T. Naito, H. Kobayashi, A. Kobayashi, V. N. Laukhin, L. Brossard, and P. Cassoux. *Synth. Met.*, **86**:2161, (1997).

[41] L. Brossard, R. Clerac, C. Coulon, M. Tokumoto, T. Ziman, D. K. Petrov, V. N. Laukhin, M. J. Naughton, A. Audouard, F. Goze, A. Kobayashi, H. Kobayashi, and P. Cassoux. *Eur. Phys. J. B*, **1**:439, (1998).

[42] H. Akutsu, E. Arai, H. Kobayashi, H. Tanaka, A. Kobayashi, and P. Cassoux. *J. Am. Chem. Soc.*, **119**:12681, (1997).

[43] T. Sasaki, H. Uozaki, S. Endo, and N. Toyota. *Synth. Met.*, **120**:759, (2001).

[44] E. Negishi, H. Uozaki, Y. Ishizaki, H. Tsuchiya, S. Endo, Y. Abe, H. Matsui, and N. Toyota. *Synth. Met.*, **133-134**:555, (2003).

[45] H. Akiba, S. Nakano, Y. Nishio, K. Kajita, B. Zhou, A. Kobayashi, and H. Kobayashi. *J. Phys. Soc. Jpn.*, **78**:033601, (2009).

[46] S. Sugiura, K. Shimada, N. Tajima, Y. Nishio, T. Terashima, T. Isono, R. Kato, and S. Uji. *J. Phys. Soc. Jpn.*, **86**:014702, (2017).

[47] S. Sugiura, K. Shimada, N. Tajima, Y. Nishio, T. Terashima, T. Isono, R. Kato, B. Zhou, and S. Uji. *J. Phys. Soc. Jpn.*, **87**:044601, (2018).

[48] J. C. Waerenborgh, S. Rabaca, M. Almeida, E. B. Lopes, A. Kobayashi, B. Zhou, and J. S. Brooks. *Phys. Rev. B*, **81**:060413(R), (2010).

[49] S. Endo, T. Goto, T. Fukase, H. Matsui, H. Uozaki, H. Tsuchiya, E. Negishi, Y. Ishizaki, Y. Abe, and N. Toyota. *J. Phys. Soc. Jpn.*, **71**:732, (2002).

[50] G. Wu, P. Ranin, G. Gaidos, W. G. Clark, S. E. Brown, L. Balicas, and L. K. Mongomery. *Phys. Rev. B*, **75**:174416, (2007).

[51] K. Hiraki, H. Mayaffre, M. Horvatic, C. Berthier, S. Uji, T. Yamaguchi, H. Tanaka, A. Kobayashi, H. Kobayashi, and T. Takahashi. *J. Phys. Soc. Jpn.*, **76**:124708, (2007).

[52] K. Hiraki, M. Kitahara, T. Takahashi, H. Mayaffre, M. Horvatić, C. Berthier, S. Uji, H. Tanaka, B. Zhou, A. Kobayashi, and H. Kobayashi. *J. Phys. Soc. Jpn.*, **79**:074711, (2010).

[53] S. Kawamata, T. Kizawa, T. Suzuki, E. Negishi, H. Matsui, N. Toyota, and T. Ishida. *J. Phys. Soc. Jpn.*, **75**:104715, (2006).

[54] T. Suzuki, H. Matsui, H. Tsuchiya, E. Negishi, K. Kajita, B. Zhou, A. Kobayashi, and H. Kobayashi. *Phys. Rev. B*, **67**:020408(B), (2003).

[55] I. Rutel, S. Okubo, J. S. Brooks, H. Kobayashi, A. Kobayashi, and T. Tanaka. *Phys. Rev. B*, **68**:144435, (2003).

[56] H. Matsui, H. Tsuchiya, E. Negishi, H. Uozaki, Y. Ishizaki, Y. Abe, S. Endo, and N. Toyota. *J. Phys. Soc. Jpn.*, **70**:2501, (2001).

[57] H. Matsui, H. Tsuchiya, T. Suzuki, E. Nefishi, and N. Toyota. *Phys. Rev. B*, **68**:155105, (2003).

[58] M. Watanabe, S. Komiyama, R. Kiyanagi, Y. Noda, E. Negishi, and N. Toyota. *J. Phys. Soc. Jpn.*, **72**:452, (2003).

[59] S. Komiyama, M. Watanabe, Y. Noda, E. Negishi, and N. Toyota. *J. Phys. Soc. Jpn.*, **73**:2385, (2004).

[60] N. Toyota, Y. Abe, H. Matsui, E. Negishi, Y. Ishizaki, H. Tsuchiya, and H. Uozaki. *Phys. Rev. B*, **66**:033201, (2002).

[61] E. Negishi, T. Kuwabara, S. Komiyama, M. Watanabe, Y. Noda, T. Mori, H. Matsui, and N. Toyota. *Rhys. Rev. B*, **71**:012416, (2005).

[62] C. Hotta and H. Fukuyama. *J. Phys. Soc. Jpn.*, **69**:2577, (2000).

[63] Cépas, R. H. Mckenzie, and J. Merino. *Phys. Rev. B*, **65**:100502R, (2002).

[64] L. Balicas, J. S. Brooks, K. Storr, S. Uji, H. Tanaka, H. Kobayashi, A. Kobayashi, V. Barzykin, and L. P. Gor'kov. *Phys. Rev. Lett*, **87**:067002, (2001).

[65] S. Sugiura, K. Shimada, N. Tajima, Y. Nishio, T. Terashima, T. Isono, A. Kobayashi, B. Zhou, R. Kato, and S. Uji. *J. Phys. Soc. Jpn.*, **85**:064703, (2016).

[66] T. Mori and M. Katsuhara. *J. Phys. Soc. Jpn.*, **71**:826, (2002).

[67] T. Nagamiya, K. Yosida, and R. Kubo. *Adv. Phys.*, **4**:1, (1955).

[68] C. P. Poole and Jr. *Electron Spin Resonance; A comprehensive Treatise on Experimental Techniques, 2nd edn.* (Dover publications, INC., Mineola, New York), (1983).

[69] T. H. Lee, Y. Oshima, H. B. Cui, and R. Kato. *J. Phys. Soc. Jpn*, **87**:114702, (2018).

[70] A. Abragam and B. Bleaney. *Electron Paramagnetic Resonance of Transition Ions.* (Dover, New York), (1986).

[71] A. Bencini and D. Gatteschi. *Electron Paramagnetic Resonance of Exchange Coupled System.* (Spinger, Berlin/Heidelberg), (1990).

[72] J. Owen and J. H. M. Thornley. *Rep. Prog. Phys.*, **29**:675, (1966).

[73] B. C. Tofield. *J. Phys. Colloq*, **37**:6568, (1976).

[74] J. C. Deaton, M. S. Gebhard, and E. I. Solomon. *Ingrg. Chem.*, **28**:877, (1989).

[75] F. Neese and E. I. Solomon. *Inorg. Chem.*, **37**:6568, (1998).

[76] H. Kobayashi, H. B. Cui, and A. Kobayashi. *Chem. Rev.*, **104**:5265, (2004).

[77] N. Takubo, N. Tajima, H. M. Yamamoto, H.-B. Cui, and R. Kato. *Phys. Rev. Lett*, **110**:227401, (2013).